

## Approaching Microsized Alloy Anodes *via* Solid Electrolyte Interphase Design for Advanced Rechargeable Batteries

Yuan Tian,<sup>1</sup> Yongling An,<sup>2</sup> Biao Zhang<sup>1,\*</sup>

Dr. Y. Tian, Prof. B. Zhang

<sup>1</sup>Department of Applied Physics & Research Institute for Smart Energy, The Hong Kong Polytechnic University, Hung Hom, Kowloon 999077, Hong Kong, China.

E-mail: biao.ap.zhang@polyu.edu.hk

Dr. Y.L. An

<sup>2</sup>Key Laboratory for Liquid-Solid Structural Evolution & Processing of Materials (Ministry of Education), School of Materials Science and Engineering, Shandong University, Jinan 250061, China.

**Keywords:** solid electrolyte interphase, microsize, alloy anode, rechargeable batteries.

### Abstract:

Microsized alloy anodes (Si, P, Sb, Sn, Bi, *etc.*) with high capacity, proper working potential, high tap density and low cost are promising for breaking the energy limits of current rechargeable batteries. Nevertheless, they suffer from large volume changes during cycling processes, posing a great challenge in maintaining a thin, dense and intact solid electrolyte interphase (SEI) layer. Recent progress suggests that the problematic SEI layer could be a treasure in maintaining the integrity of the microparticle anodes if well designed, which would significantly boost the cyclic stability without resorting to complex electrode architectures. We review the advances in this attractive direction to shed light on future development. Firstly, the key scientific issues of high-capacity microsized alloy anodes and the fundamentals of SEI layer are discussed. Thereafter, progress on the regulation strategies of SEI layer in high-capacity microsized alloy anodes for advanced rechargeable batteries, including electrolyte engineering, electrode surface modification, cycle protocols, and electrode architecture design, are outlined. Finally, potential challenges and perspectives on developing high-quality SEI layer for microsized alloy anodes are proposed.

## 1. Introduction

High-energy-density, high-safety and low-cost rechargeable batteries have attracted tremendous interest with the increasing demands of portable electronic devices, electric vehicles, and smart grids.<sup>[1-3]</sup> Alloy anode materials from group IV (like Si, Ge, Sn) and group V (like P, Sb, Bi) are highly desirable for high-energy batteries owing to their appealing theoretical specific capacity and proper working potential.<sup>[4, 5, 6-8]</sup> Unfortunately, alloy anodes suffer from large volume changes during the cycling process, which causes mechanical failure of active materials and the associated solid electrolyte interphase (SEI) layer.<sup>[9-11]</sup> Both lead to the exposure of the fresh surface to the electrolytes for copious SEI formation, resulting in low Coulombic efficiency, large internal resistance and poor cycle performance.<sup>[12-15]</sup> Extensive efforts have been devoted to the design of nanostructured alloy electrodes to address the challenges, with the preparation of carbon/alloy composite as the most typical representative. These strategies essentially improve the cyclic stability but bring about other issues, such as reduced volumetric energy density and high fabrication cost. It is tempting to directly employ the commercially available microparticles in view of practical application.<sup>[11, 14-18]</sup> Nevertheless, the fracture of microparticles becomes more severe in such cases, which also makes the building of a stable SEI layer more arduous.

SEI layer is deemed the most significant interface on the anode side for various rechargeable batteries.<sup>[19, 20]</sup> It is spontaneously generated on the anode surface by the electrolyte decomposition and the reaction between electrolyte and anode in the initial charge process when the redox potential of the anode is below the reduction potential of electrolyte.<sup>[9, 10, 21-25]</sup> An ideal SEI layer should allow fast cation transfer to boost the reaction kinetics but block the electron transfer from the anode to electrolytes to prevent continuous electrolyte consumption and side reactions at the anode.<sup>[21, 25]</sup> Therefore, the features of SEI layer, including microstructure, chemical composition, mechanical properties, ionic conductivity, solubility, *etc.*, play essential roles in determining the Coulombic efficiencies, cycling stability and even safety.<sup>[9, 23, 26-28]</sup>

The SEI layer becomes vulnerable in the alloy anodes because of the large stress during electrode swelling and contraction.<sup>[29, 30]</sup> The anodes with low-quality SEI layer during cycling will face the following issues.<sup>[31, 32]</sup> (1) Large volume change of anode makes the fragile SEI layer break or even peel off from the surface of active materials.<sup>[4, 14]</sup> (2) Electrolyte penetrates the broken interface and further reacts with the exposed anode surface, consuming the electrolyte and generating a fresh SEI layer. As a result, the SEI layer becomes thick and uneven, leading to increased internal resistance.<sup>[9, 15, 33, 34]</sup> (3) It has been demonstrated that SEI

components (like NaF, Na<sub>2</sub>CO<sub>3</sub>) could be dissolved in some electrolytes (*e.g.*, propylene carbonate (PC)-based electrolyte<sup>[35]</sup>), hindering the formation of stable SEI layer and thereby deteriorating the electrochemical performance.<sup>[35, 36]</sup> On the contrary, a delicate SEI having superior mechanical stability would maintain its integrity despite the large volume change. Moreover, recent studies show that the well-designed SEI layer could also help stabilize the microsized anodes, thus avoiding the complicate electrode architecture for facilitating the practical application. However, a comprehensive understanding of SEI on the microsized alloy anode is lacking.

This review provides clear design perspectives of high-quality SEI for microsized alloy anodes in rechargeable batteries. We first summarize the merits and critical scientific challenges of microsized alloy anodes. Then, the fundamental background, advanced characterization techniques to unravel mechanical properties, composition and structure of SEI layer, and factors influencing SEI layer are reviewed. Subsequently, we systematically discuss the major design strategies of the omnipotent SEI layer for microsized alloy anodes from the following aspects: (1) regulating electrolytes formulation, (2) building artificial protective layers, (3) optimizing cycling protocols, and (4) tailoring electrode materials. Finally, we discuss the remaining scientific challenges for further boosting SEI layer.

## 2. Understanding of microsized alloy anode and SEI

### 2.1. Microsized alloy anodes

#### 2.1.1. Advantages of alloy anodes

Carbonaceous materials (*e.g.*, hard carbon, graphite) are very advantageous in terms of stable cycling performance, but their moderate capacities restrict the energy density of a battery.<sup>[37-39]</sup> In comparison, several group IV (like Si, Ge, Sn) and group V (like P, Sb, Bi) possess higher theoretical specific capacities based on the alloying mechanism and proper working potential in rechargeable alkali-metal ion batteries.<sup>[7, 12, 16, 37, 40-42]</sup> Their specific features are summarized as follows:

(1) Silicon (Si) is one of the most promising anodes for lithium-ion batteries (LIBs) due to the high theoretical specific capacity (4200 mAh g<sup>-1</sup> according to the formation of Li<sub>4.4</sub>Si, 3579 mAh g<sup>-1</sup> for Li<sub>3.75</sub>Si alloy at mild temperature), low working potential (0.2~0.3 V *vs.* Li/Li<sup>+</sup>), low cost, nontoxicity, high abundance, *etc.*<sup>[41, 43, 44-47]</sup>

(2) Phosphorus (P) is deemed one of the highest-capacity alloy anodes for sodium-ion batteries (NIBs) and potassium-ion batteries (KIBs).<sup>[29, 48-50]</sup> In nature, there are three types of P allotropes, including white phosphorus (P<sub>white</sub>), red phosphorus (P<sub>red</sub>), and black phosphorus (P<sub>black</sub>). Among these allotropes, P<sub>white</sub> has a low melting point and presents a safety issue

associated with the self-ignition at room temperature, thereby being excluded as a potential alloy anode.  $P_{red}$  possesses high theoretical specific capacity, moderate working voltage (like  $\sim 0.4$  V vs. Na/Na<sup>+</sup>), low cost, nontoxic and safe nature.<sup>[51]</sup> Nevertheless, it suffers from large volume change ( $>400\%$ ), low electronic conductivity ( $\sim 10^{-14}$  S cm<sup>-1</sup>), unstable SEI layer, and poor cycling performance.  $P_{black}$  is a two-dimensional (2D) anisotropic layered material, which has a 5.2 Å interlayer distance.  $P_{black}$  possesses superior thermal stability, relatively high electronic conductivity ( $0.2-3.3 \times 10^2$  S cm<sup>-1</sup>), and high charge-carrier mobility.<sup>[52, 53]</sup> Notably,  $P_{black}$  can be fabricated from  $P_{red}$  under high-pressure and high-temperature conditions<sup>[54]</sup> or through high-energy ball milling.<sup>[52, 54]</sup>

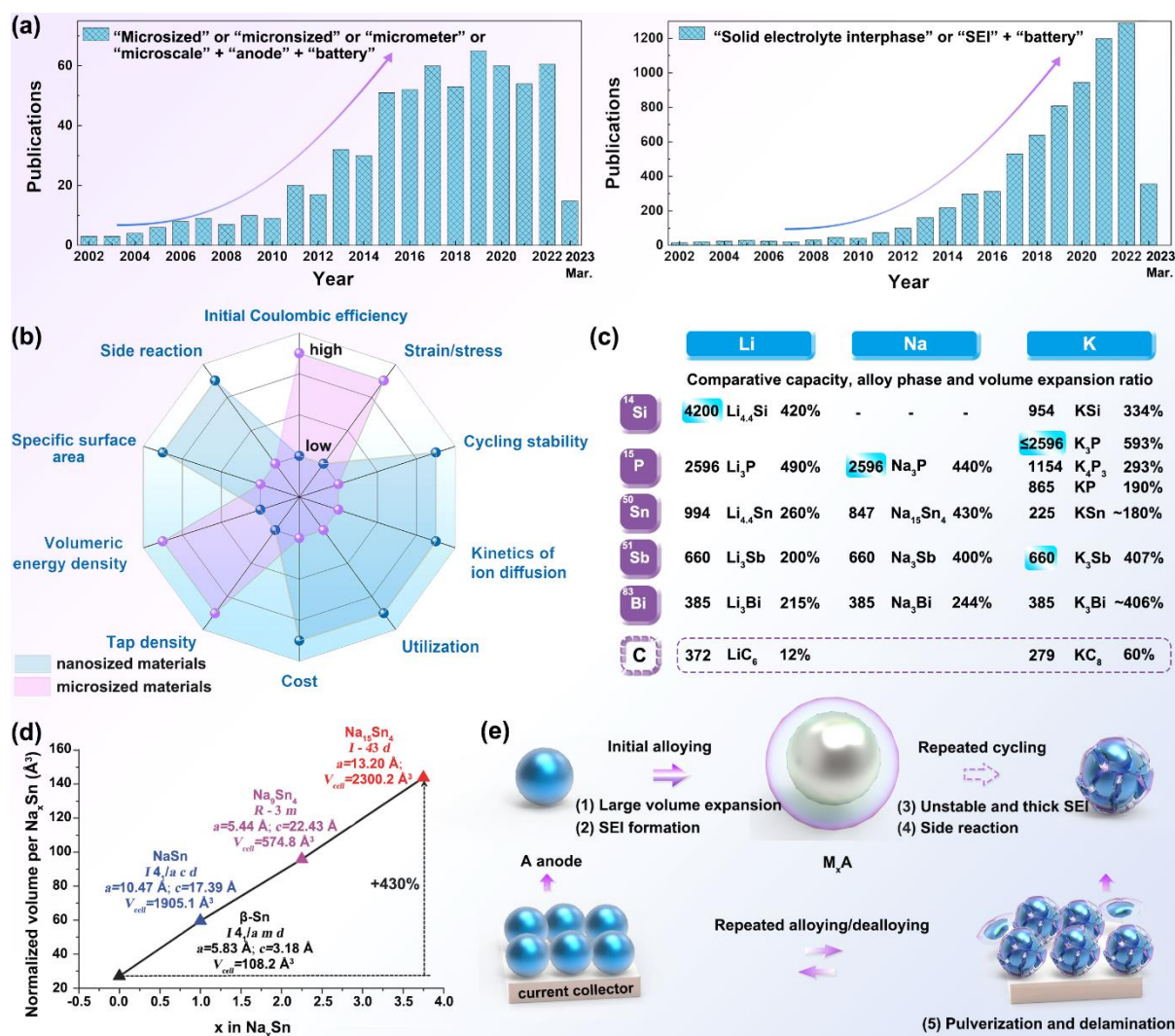


**Figure 1. Importance of SEI layer with regard to micro-sized alloy anode.** (a) The number of publications and cited frequency on the topic of SEI and micro-sized alloy anodes (updated on March 2023). The keywords used for the search in "Web of Science" were "micro-sized or micron-sized or microscale or micrometer + anode + battery" and "battery + solid electrolyte interphase or SEI". (b) The comparison of micro-sized and nanosized anode materials in cost, specific surface area, tap density, initial Coulombic efficiency, cycling stability, the kinetics of

ion diffusion, and volumetric energy density. (c) Theoretical gravimetric specific capacities, corresponding alloy phase and volume expansion ratio of high-capacity alloy anodes and graphite (or carbon) anode for LIBs, NIBs and KIBs. (d) Volume change during Na-Sn alloy. Adopted from Ref.<sup>[15]</sup> with permission. Copyright 2016 Wiley. (e) The challenges of alloy anodes during cycling processes (A is the alloy anode, and  $M_xA$  is the alloy phase).

(3) Metallic tin (Sn) is a low-cost, environmentally friendly material that is abundant in nature.<sup>[55-58]</sup> It shows a high theoretical capacity and proper average reaction potential, *i.e.*, 994 mAh g<sup>-1</sup>, below 0.6 V vs. Li/Li<sup>+</sup>; 847 mAh g<sup>-1</sup>, ~0.2-0.4 V vs. Na/Na.<sup>[59, 60]</sup>

(4) Metallic antimony (Sb) for NIBs and KIBs is also a promising anode candidate owing to decent theoretical specific capacity (660 mAh g<sup>-1</sup>), proper reaction potential (~0.4-0.8 for Na and ~0.4-0.5 V for K), and relatively high electronic conductivity ( $2.5 \times 10^4$  S cm<sup>-1</sup>).<sup>[16, 61]</sup>

(5) Metallic bismuth (Bi) possesses nontoxic nature and large interlayer spacing (~0.395 nm) along the c-axis.<sup>[7, 62, 63]</sup> Compared with the above other alloy anode materials, Bi anode is less popular for LIBs and NIBs due to its limited capacity. In contrast, it has attracted attention in KIBs owing to low reaction potential and high capacity among the reported anodes.<sup>[7]</sup>

### 2.1.2. Benefits of microsized alloy anodes

Since the use of Si nanowires to buffer the volume expansion during Li-Si alloying in 2008,<sup>[64]</sup> various low-dimensional nanostructured materials, like nanodots,<sup>[57]</sup> nanowires,<sup>[65]</sup> nanotubes,<sup>[56, 59]</sup> nanopores,<sup>[16, 49]</sup> and 2D nanosheets, have experienced prosperity rapidly. The nanomaterials can enable less or even zero strain for SEI formation during cycling processes, thereby mitigating the destruction of SEI and consumption of electrolytes and improving cyclic stability.<sup>[41, 49, 66]</sup> Moreover, high surface-to-volume ratios of nanomaterials ensure sufficient contact between active materials and electrolytes, provide large amounts of electrons/ions transfer pathways, promote diffusion kinetics, and enhance rate performance.<sup>[41, 44, 67, 68]</sup> However, the large contact area of nanomaterials with electrolytes also results in large irreversible capacity loss due to the copious SEI formation in the initial cycle, leading to low initial Coulombic efficiency.<sup>[10, 15, 33, 52, 69]</sup> Moreover, low tap-density of nanomaterials can lead to the low volumetric energy density of a battery.<sup>[15]</sup> Furthermore, well-designed nanomaterials generally require complicated manufacture processes and, thus, a high fabrication cost.<sup>[16, 33, 70, 71]</sup>

In contrast, microsized materials demonstrate greater potential for practical applications than those nanomaterials in the aspects of areal mass loading, volumetric energy density, Coulombic efficiency, fabrication process and cost (**Figure 1b**).<sup>[10, 14, 15, 17, 33, 52, 69, 72]</sup> The booming publications on microsized anodes for rechargeable batteries in recent years reflect the keen

interest of the scientific community (Figure 1a). Briefly, (1) owing to the large size, microsized materials have high tap density. It means that electrode composed of microsized materials has higher mass loadings at a certain thickness than nano-counterparts, leading to higher volumetric capacity and energy density, which is promising to satisfy the demand for portable energy storage devices.<sup>[73]</sup> (2) Low specific surface of microsized materials significantly decreases contact area with electrolytes, which mitigates capacity loss in the initial cycle and enhances the first Coulombic efficiency.<sup>[10, 15, 33, 52, 69, 74]</sup> (3) Microsized materials are easily fabricated, simplifying the fabrication process and presenting remarkably cost advantages.<sup>[75]</sup> Therefore, from the perspective of practical application, microsized alloy anodes with a high specific capacity, low reaction potential, and high tap density are promising candidates for the commercial implementation of high-energy batteries.

### 2.1.3. Challenges of SEI layer for microsized alloy anodes

Figure 1c summarizes the volume expansion ratios of the commonly used alloy anodes for LIBs, NIBs and KIBs.<sup>[7, 12, 42]</sup> For example, high-capacity  $P_{red}$  anode experiences a volume change of 499% upon sodiation processes.<sup>[51]</sup> Sn anode suffers from 260% and ~430% (Figure 1d) volume expansion, corresponding to the phase transformation from Sn to  $Li_{4.4}Sn$  and  $Na_{15}Sn_4$ , respectively. Such a huge volume change may lead to severe pulverization of the active materials.<sup>[76]</sup> The massive volume expansion of alloy anodes poses a great challenge in maintaining an intact SEI layer.<sup>[4, 33, 69, 77]</sup> As illustrated in Figure 1e, large volume expansion occurs due to the formation of  $M_xA_y$  alloy phase. Meanwhile, a SEI protective layer is spontaneously generated on the alloy anode surface along with the electrolyte consumption. Once the SEI layer is broken because of the large strain, the electrolyte will further react with the freshly exposed anode surface, leading to further consumption of electrolytes.<sup>[4]</sup> This newly formed SEI layer could isolate the fragmented active materials, resulting in the loss of compact electrical contact.<sup>[33, 77]</sup> Notably, these issues occur in every cycle, which can lead to repeated failure and continuous formation of SEI layer as well as severe electrode pulverization. As a result, the SEI layer becomes thick and uneven, and the electrolyte is severely consumed. Moreover, it will decrease the reversible capacity due to excessive consumption of the charges from the cathodes. Significant stress would be exerted on the SEI layer grown on the microsized alloy particles, making it more challenging to keep SEI stable. Therefore, a high-quality SEI layer is essential to achieve superior electrochemical performance.

## 2.2. Fundamental background of SEI layer



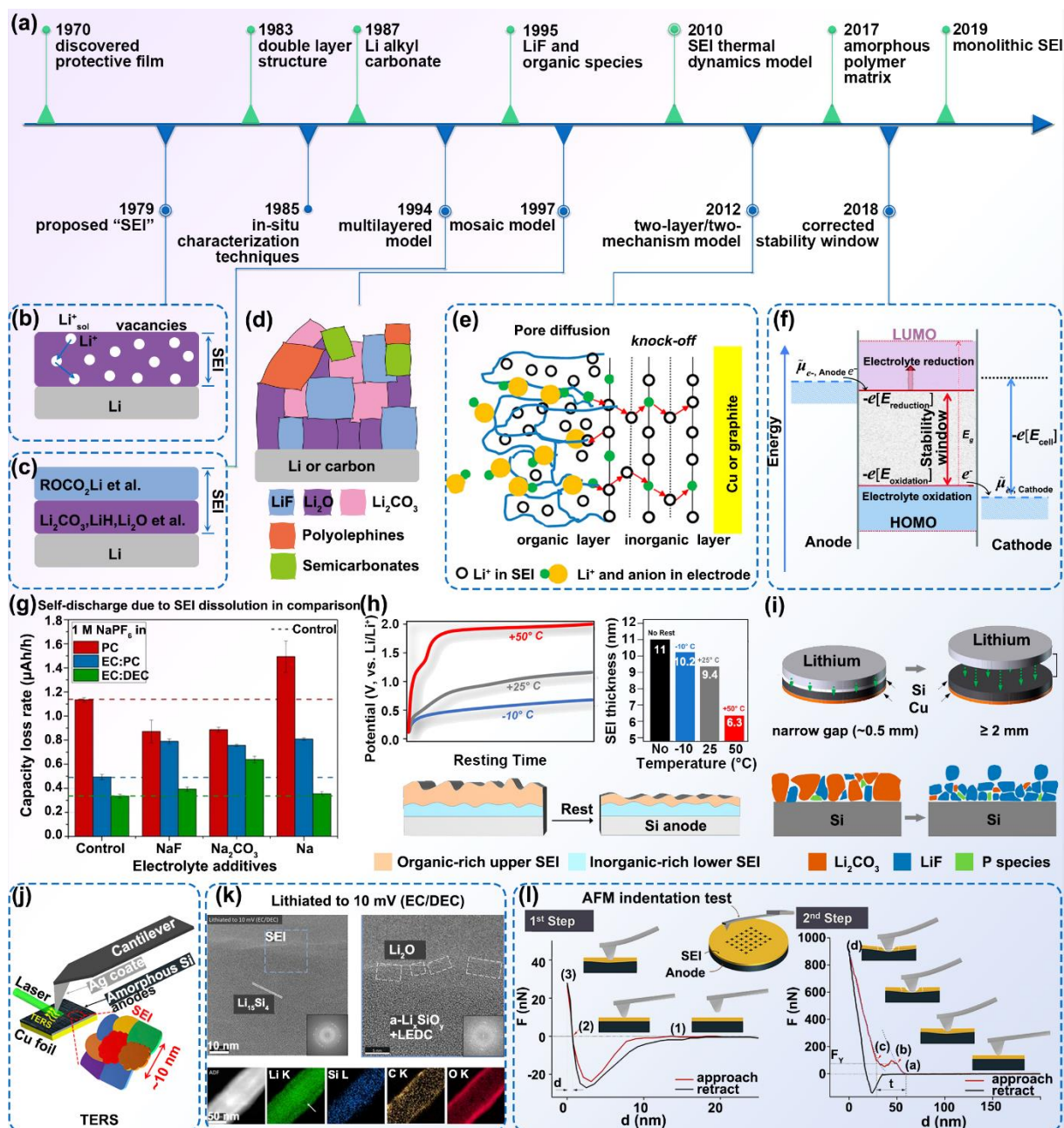


**Figure 2. Development history and advanced characterization of SEI layer.** (a) Timelines of SEI layer. (b) The SEI model proposed in 1979.<sup>[78]</sup> (c) Multilayered SEI model proposed in 1994.<sup>[79]</sup> (d) Classical Mosaic model on Li-metal or carbon anode. Adopted from Ref.<sup>[80]</sup> with permission. Copyright 1997 The Electrochemical Society. (e) Schematic illustration of ionic diffusion through inner inorganic and outer organic layers of SEI. Reproduced with permission from Ref.<sup>[81]</sup> Copyright 2012 American Chemical Society. (f) Corrected electrolyte stability window. Reproduced from Ref.<sup>[82]</sup> with permission. Copyright 2018 Royal Society of Chemistry. (g) The comparison of capacity loss rates when adding NaF, Na<sub>2</sub>CO<sub>3</sub> and Na to the electrolytes. Reproduced from Ref.<sup>[35]</sup> with permission. Copyright 2020 The Authors. (h) The influence of temperature on SEI layer. Reproduced from Ref.<sup>[83]</sup> with permission. Copyright

2019 American Chemical Society. (i) Schematics of SEI layer after electrochemical pretreatment with standard and enlarged distance between electrodes. Reproduced from Ref.<sup>[84]</sup> with permission. Copyright 2022 American Chemical Society. (j) TERS. Reproduced from Ref.<sup>[85]</sup> with permission. Copyright 2019 Elsevier. (k) Cryo-(S)TEM images of lithiated Si nanowires in EC/DEC electrolyte. Reproduced from Ref.<sup>[115]</sup> with permission. Copyright 2019 Elsevier. (l) Mechanical properties of SEI layer *via* a two-step AFM-based nanoindentation test. Reproduced from Ref.<sup>[9]</sup> with permission. Copyright 2021 Elsevier.

For boosting the construction of a high-quality native SEI layer for high-capacity alloy anodes, understanding the formation mechanisms, structures, compositions, and properties of SEI layer is urgent and essential.<sup>[26, 87]</sup> Hence, in this section, we summarize some fundamentals of SEI layer, including the historical advances, advanced characterization techniques, functionality and required merits, primary factors influencing SEI formation, and regulation strategies of SEI layer.

### 2.2.1. History, formation mechanism and significance of SEI layer

**Figure 2a** outlines the vital advances in the formation mechanism, roles, the models for components and structures of SEI layer. In 1970, Dey *et al.*<sup>[88]</sup> firstly discovered the existence of a protective film consisting of electrolyte decomposition products in liquid electrolyte Li-metal batteries.<sup>[78, 88]</sup> Subsequently, Peled *et al.*<sup>[78]</sup> proposed the term "SEI" in 1979 (Figure 2b). They revealed that SEI layer was instantly formed between the anode and electrolyte due to the reaction of the anode with the electrolyte. SEI layer possessed the properties of a solid-state electrolyte that was electronically insulating but ionically conductive. The feature of SEI layer can affect the corrosion rate of metal anode, the reaction mechanism during deposition/dissolution process, and deposition morphology. In 1983, Peled *et al.*<sup>[89]</sup> pointed out that SEI had a double-layer structure. The inner layer near the electrode was thin and compact. The outer thick layer close to the electrolyte presented porous features.

In 1985, Nazri *et al.*<sup>[90]</sup> firstly investigated the composition of SEI on Li electrode by adopting a series of characterization techniques, including *in-situ* X-ray diffraction (XRD), secondary ion mass spectroscopy (SIMS), low angle X-ray photoelectron spectroscopy and infrared spectroscopy (IR). The study identified the existence of  $\text{Li}_2\text{CO}_3$  and polymeric species in SEI layer. In 1987, Aurbach *et al.*<sup>[91]</sup> investigated SEI layer in PC and diethyl carbonate (DEC) of  $\text{LiC}_1\text{O}_4$ ,  $\text{LiAsF}_6$ , and  $\text{LiSO}_3\text{CF}_3$  *via* X-ray photoelectron spectroscopy (XPS) and Fourier transform infrared spectroscopy (FTIR), disclosing solvent and salt reduction reactions. In PC-based electrolytes, the primary components of SEI were lithium alkyl carbonates ( $\text{RCO}_3\text{Li}$ , R=alkyl), while lithium ethyl carbonate ( $\text{CH}_3\text{CH}_2\text{CO}_3\text{Li}$ ) was dominant in DEC-derived SEI.



In 1995, Kanamura *et al.*<sup>[92]</sup> observed the existence of many organic components and LiF in the SEI generated in a LiBF<sub>4</sub>-based electrolyte *via* spectroscopic studies and the potential sweep approaches.

In 1997, Peled *et al.*<sup>[80]</sup> proposed the classical mosaic model of SEI. It demonstrated that SEI was generated instantaneously upon exceeding the cathodic thermodynamic stability of the electrolyte. This surface film consisted of multifarious organic and inorganic species, which were formed owing to electrolyte decomposition on the surface of active material. Figure 2d illustrates the distribution of inorganic and organic species, where inorganic-rich species were located closer to the lithiated carbons or Li metal.

Besides, in 2012, Shi *et al.*<sup>[81]</sup> elucidated a two-layer/two-mechanism of Li<sup>+</sup> transport through SEI (Figure 2e). In a porous organic layer of SEI, Li<sup>+</sup> can rapidly transport, while Li<sup>+</sup> in a dense organic layer diffuses *via* a repetitive knock-off mechanism. Development of advanced technology, like cryogenic transmission electron microscopy (cryo-TEM)) has significantly deepened our understanding of SEI's microstructures.<sup>[93]</sup> Several unique SEIs are observed, such as monolithic and organic-inorganic composite types, which facilitate establishing the structure-property correlations.

The thermodynamic models for SEI formation have also been extensively explored. Goodenough *et al.*<sup>[94]</sup> proposed the classical thermodynamic description of SEI formation by molecular orbital theory. The energy gap between the highest occupied molecular orbital (HOMO) and the lowest unoccupied molecular orbital (LUMO) of the electrolyte was considered the thermodynamic stability window of electrolyte. An anode with chemical potentials higher than LUMO will automatically transfer accessible electrons to the electrolyte, reducing the electrolyte and leading to the formation of SEI on the anode surface in the initial charge process.<sup>[21, 94]</sup> Peljo *et al.*<sup>[82]</sup> revealed later that it was not appropriate to consider the LUMO-HOMO of the solvents only because of complicated reactions participated inside the cells. Figure 2f presents the corrected model. The electrolyte reduction potential at the anode would be more accurate in determining the SEI formation process.

### 2.2.2. Required merits of SEI layer

The ideal SEI layer allows fast cations transport but blocks other solvent molecular and electrons, suppresses electrolyte decomposition, and accommodates the volume variation of the active materials (**Figure 3a**).<sup>[21, 25]</sup> To achieve high Coulombic efficiencies and stable cycling performance, the desired merits for an ideal SEI of high-capacity alloy anodes are discussed and summarized as follows:

(1) **Superior ionic conductivity and electrical insulation.** The SEI layer requires high

cation ( $\text{Li}^+$ ,  $\text{Na}^+$ ,  $\text{K}^+$ , *etc.*) diffusivity for achieving a high-power density.<sup>[28, 33, 36, 86, 95, 96]</sup> Therefore, uniform and thin SEI close to a few nanometers is necessary to boost fast ions transport. Besides, SEI layer should also be electronically insulating to prevent continuous electrolyte decomposition.<sup>[36]</sup>

(2) **Outstanding mechanical properties.** Due to the large volume change of high-capacity alloy anodes during cycling, the SEI needs to have sufficient tolerance to ensure its integrity.<sup>[9, 10, 28, 97]</sup> Therefore, outstanding SEI requires high mechanical toughness, that is, a combination of strength and ductility (or elasticity).<sup>[9, 10]</sup> The ductility can ensure reversible deformation of SEI without irreversible plastic deformation and fracture when experiencing large volume expansion.<sup>[9, 10]</sup> In 2018, Huang *et al.*<sup>[10]</sup> discovered that outstanding elastomers were preferred components of SEI layer. In 2021, Gao *et al.*<sup>[9]</sup> proposed that the “maximum elastic deformation energy” of SEI, which coupled the effect of Young’s modulus with the largest elastic strain, can predict cycling stability.

(3) **Chemical and thermal stability.** To avoid undesirable side reactions with electrolytes, the SEI needs to be chemically stable and insoluble in the electrolyte.<sup>[9, 10, 87, 98-101]</sup> Previous studies demonstrated that some SEI components (like inorganic NaF,  $\text{Na}_2\text{CO}_3$ ) had high solubility in organic solvents,<sup>[35, 36, 87, 102]</sup> which could lead to severe self-discharge and fast capacity loss.<sup>[35, 36]</sup> As early as 2001, Moshkovich *et al.*<sup>[102]</sup> indicated that  $\text{NaClO}_4$ -PC derived-SEI components were more soluble than SEI components generated from  $\text{LiClO}_4$  and  $\text{KClO}_4$  salts. In 2016, Younesi’s group<sup>[36]</sup> unveiled that most sodium inorganic species of SEI presented higher solubilities than these of Li analogs. In 2021, Younesi’s group<sup>[35]</sup> further analyzed the influence of SEI formation and dissolution in  $\text{NaPF}_6$ -PC,  $\text{NaPF}_6$ -EC/PC and  $\text{NaPF}_6$ -EC/DEC on electrochemical performance. As shown in Figure 2g, the  $\text{Na}_2\text{CO}_3$  and NaF inorganic species have the highest solubility in PC-based electrolytes, leading to the fastest self-discharge rate. The issues could be alleviated by saturating the electrolytes by adding these species as electrolyte additives. Until now, the dissolution of SEI in electrolytes is still a big challenge. Hence, developing effective strategies to avoid the dissolution of SEI components are essential for boosting the electrochemical performance.

Moreover, the practical rechargeable batteries powering mass-market electric vehicles must be able to operate over a wide temperature range.<sup>[83, 98-101, 103]</sup> However, the formation kinetics and stability of SEI are temperature sensitive.<sup>[26]</sup> High operation temperature will aggravate the dissolution of some SEI components, reactions between SEI and active materials, and electrolyte decomposition.<sup>[26, 98, 99]</sup> These detrimental reactions could lead to the thermal runaway of a battery.<sup>[26, 98, 99]</sup> As shown in Figure 2h, the comparison of electrochemical profiles

and SEI thickness indicated that SEI dissolves or detaches at faster rates when operating at higher temperatures.<sup>[83]</sup> Therefore, for stable operation in extreme conditions, the SEI layer must have excellent stability over a wide temperature and voltage range.

### 2.2.3. Advanced SEI characterization techniques

The SEI layer generally has complicated chemical components and nano-microstructure. Moreover, it is very sensitive to both air and electron beams. These characteristics make it difficult to accurately probe the composition, structure, and other physical/chemical properties.<sup>[9, 10, 104, 105]</sup> Therefore, developing advanced characterization techniques and analytical methods is essential.<sup>[20, 106-108]</sup> We briefly summarize the commonly used characterization techniques in this section. As early as 1985, some techniques such as *in-situ* XRD, secondary ion mass spectroscopy (SIMS), low angle XPS and IR have been utilized to analyze the components of SEI.<sup>[90]</sup> Subsequently, FTIR, IR and XPS are employed to reveal the solvent and salt reduction reactions in liquid electrolytes.<sup>[91]</sup> We summarize the commonly used techniques in characterizing different properties of SEI as follows.

#### (a) Composition characterization

The surface-sensitive nature of XPS makes it an ideal tool for analyzing the organic and inorganic components in the SEI with a nanoscale thickness. XPS normally has a probing depth of 5-10 nm, revealing the elements presented and their relative amounts. The chemical states of the elements could help infer the possible products regardless of their crystallinity. To examine the homogeneous along the thickness direction, an ion beam is adopted to etch the surface for proving a depth profiling. Furthermore, time-of-flight SIMS (TOF-SIMS) has attracted wide attention in probing the SEI composition recently. Compared to XPS, a 3D image of the species could be obtained to show the distributions. For instance, Xu's group<sup>[106]</sup> established a dynamic picture of the SEI by employing an *in-situ* liquid SIMS in combination with molecular dynamics simulations. Dahbi *et al.*<sup>[54]</sup> adopted TOF-SIMS and hard XPS to analyze chemical components of SEI layer on P<sub>black</sub> anode for NIBs.

Electrochemical quartz crystal microbalance (EQCM), an inverse-piezoelectric-phenomenon-based gravimetric analytical tool, presents promising potential in quantitatively analyzing SEI compositions and the variations, owing to its high sensitivity to mass changes.<sup>[108-110]</sup> EQCM could probe the species accumulated on or lost from the electrode as a function of the applied potential during electrochemical processes.<sup>[109]</sup> For example, Zhang *et al.*<sup>[111]</sup> discovered that SEI layer formation process on Al varies with the potential change via the EQCM technique. Liu *et al.*<sup>[109]</sup> precisely identified LiF and lithium alkylcarbonates as the main chemical components of SEI at different potentials by measuring the mass change of

graphitic anode during the first lithiation process *via* EQCM.

Optical methods, such as Raman and FITR, have also been used to complement the above tools. Because of the relatively poor resolution, these techniques normally only provide the overall information of the components, provided reference spectra of the species are available. Nevertheless, the rapid development of the techniques offers new opportunities. Tip-enhanced Raman spectroscopy (TERS) has enabled a sampling depth of <5 nm and lateral resolution of <10 nm.<sup>[85, 112]</sup> Nanda *et al.*<sup>[85]</sup> adopted the TERS technique to acquire nanoscale topography and chemical mapping of SEI layer generated on an amorphous Si anode (Figure 2j). Recently, Gajan *et al.*<sup>[86]</sup> investigated the dynamic composition variation in the electrode/electrolyte interphase using shell-isolated nanoparticle-enhanced Raman spectroscopy conditions, revealing the origin of the irreversible capacity of Sn electrodes in LIBs.

#### (b) Structure characterization

Because of SEI's nanoscale thickness, TEM is generally adopted to examine the nanostructure, such as thickness, the particle size of the inorganic species, and distribution. This information is essential to build the SEI structure models in simulating stability. Furthermore, electron energy loss spectroscopy (EELS) coupled with energy-dispersive X-ray spectroscopy (EDS) can precisely acquire atomic-resolution structural and chemical information of SEI layer.<sup>[113, 114]</sup> In particular, the EELS could complement the XPS in identifying the possible organics species.<sup>[10]</sup> Note that the SEI is sensitive to electron beams, which may damage the SEI under a long irradiation time. The issue could be largely resolved by examining at cryogenic temperatures. The prefix "cryo-" is used to indicate the test at cryogenic conditions. For example, Huang *et al.*<sup>[115]</sup> adopted cryo-(S)TEM and cryo-EELS techniques to show the evolution of the SEI layer on the Si anode surface in the first cycle. As shown in Figure 2k, the analysis revealed a bilayer SEI (the exterior was crystalline Li<sub>2</sub>O and amorphous Li ethylene decarbonate (LEDC), and the inner was amorphous Li<sub>x</sub>SiO<sub>y</sub>) on lithiated Si in 1 M LiPF<sub>6</sub>-EC/DEC. Moreover, it was discovered that FEC additive in 1 M LiPF<sub>6</sub>-EC/DEC can contribute to a more stable SEI layer with an inner organic poly(VC) and external inorganic Li<sub>x</sub>SiO<sub>y</sub>.

Scanning probe microscopy relies on a physical tip to collect high spatial-resolution images of surfaces.<sup>[113]</sup> It includes a series of microscopic techniques, such as scanning electrochemical microscopy (SECM) and AFM, which have also been used to monitor the topography of the SEI layer. In particular, SECM, an electroanalytical scanning probe technique, can scan diversified interfaces (like liquid/liquid, liquid/gas and liquid/solid) and is capable of imaging substrate topography and local reactivity with nanoscale resolution.<sup>[113, 116]</sup> SECM has been utilized for *in situ* visualization analysis of SEI evolution on various electrodes. It can determine

the interplay and interfacial kinetics between local structures/compositions and reactivity by recording current responses during electrochemical processes.<sup>[108]</sup> Wittstock *et al.*<sup>[117]</sup> visually analyzed the spatiotemporal changes of SEI on graphite anode by utilizing SECM feedback mode with a 2,5-di-tert-butyl-1,4-dimethoxy benzene mediator. SECM combined with other advanced techniques, such as enhanced Raman spectroscopy, further effectively promoted the analysis of SEI formation and properties on Si anodes under different conditions, facilitating the design of SEI layer.<sup>[118]</sup> In addition, AFM is also a powerful morphological analysis tool to reveal the 2D/3D structural features and roughness of the surface, although this could be interfered by the anode substrate in SEI characterization.<sup>[9, 119, 120, 121]</sup> Generally, these scanning probe microscopies are powerful in showing the overall morphology of SEI, such as homogeneity and coverage. Yet, they are insufficient to provide detailed nanostructures at the current stage.

#### (c) Mechanical properties and ionic conductivity

The mechanical test of SEI has been thoroughly reviewed in previous work.<sup>[112]</sup> As it is challenging to prepare a freestanding SEI layer, AFM-based nanoindentation is the most test to examine the mechanical properties of SEI layer.<sup>[9, 119, 120]</sup> As illustrated in Figure 21, Gao *et al.*<sup>[9]</sup> optimized and designed a two-step AFM-based nanoindentation test to separately analyze elastic and plastic features of SEI layer. Yielding strain and Young's Modulus of SEI layer generated on the metal anodes or alloy anodes were measured from the AFM test. A maximum elastic deformation energy was proposed to predict the stability of SEI layer on various electrodes. Moreover, the AFM test can be conducted in liquid environments, which is promising for analyzing real-time electrode/electrolyte interfacial changes in liquid electrolytes *via* an *in-situ* AFM test.<sup>[105]</sup> Turning to ionic conductivity, electrochemical impedance spectroscopy (EIS) is a simple and effective tool for analyzing kinetics. The ionic conductivity across the SEI could be obtained by simulating the results with equivalent circuits. It is worth mentioning that EIS provides the kinetics at the electrode level without reflecting the effect of localized structural fluctuation. Scanning Probe microscopy may provide new opportunities to reveal the kinetics at specific sites by applying a localized potential via the nanoscale tip, which requires further investigation.

The complementary techniques discussed above could disclose insightful features of SEIs. As the SEI layer is sensitive to humidity and oxygen, it is essential to preserve the SEI integrity by either testing in protecting atmosphere, such as in glovebox, or transferring into the equipment chamber under vacuum/inert gas *via* a special holder. The chemical/electrochemical stability of the SEI layer could be probed through *in-/ex-situ* tests at different cycling or storing

states. The studies of the SEI's thermal stability are relatively less compared to the structure/morphological characterization. Recently, optical fiber sensors have been employed to detect the formation mechanism of SEI layer and thermal events associated with the SEI.<sup>[122, 123]</sup> For example, Huang *et al.*<sup>[123]</sup> showed tilted fiber Bragg grating optical fiber sensors can operando monitor the chemistry and states of electrolytes, which helped the understanding SEI formation mechanisms. Desai *et al.*<sup>[122]</sup> further utilized optical sensors to operando track the thermal events of interfacial reactions and explored the role of electrolyte additives upon the SEI/cathode electrolyte interphase formation in NIBs.

#### 2.2.4 Factors influencing SEI and regulation strategies

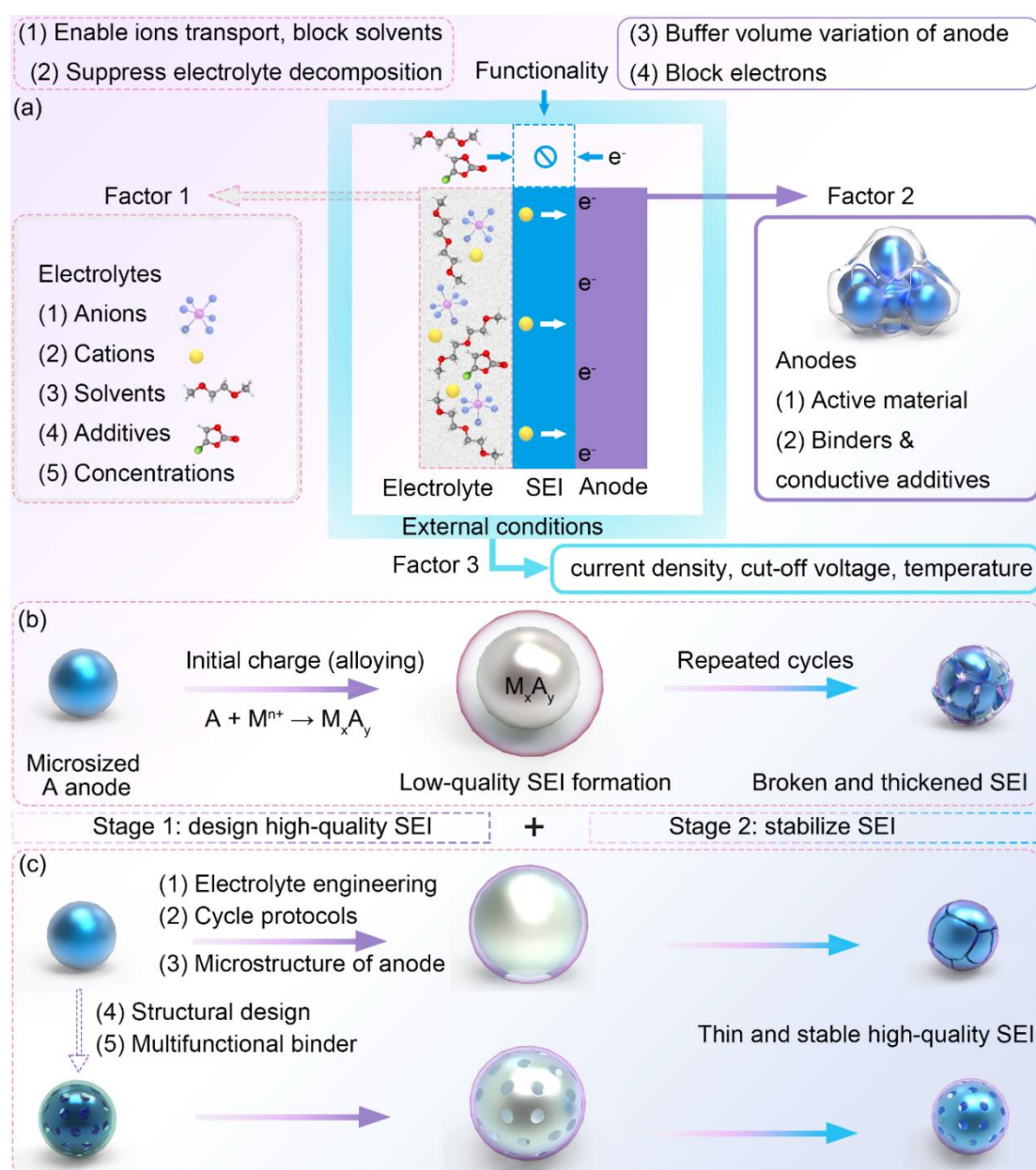


**Figure 3. Factors affecting SEI layer and regulation strategies.** (a) The roles and factors influencing SEI layer. The formation and growth of SEI layer for microsized alloy anodes (b)

without and (c) with rational design and stabilization strategies.

As illustrated in **Figure 3**, taking full advantage of SEI requires two stages: (1) designing a high-quality SEI layer in initial alloying and (2) stabilizing SEI in subsequent repeated cycling processes. In the initial reduction, the native SEI layer is spontaneously generated on the anode surface by the electrolyte decomposition when the anode's redox potential is below the electrolyte's reduction potential.<sup>[9, 10, 21-25]</sup> According to the interfacial chemistry and reduction kinetics, the quality of native SEI generated on the anode surface strongly depends on electrolytes, anodes, and external conditions such as current density and cut-off voltage. During the repeated cycling process, the SEI layer undergoes a series of dynamic structural evolution. The formation and stability of SEI are affected by complex factors, which can be briefly summarized as follows:

(1) **Electrolytes.** The electrolyte is undoubtedly the most critical factor. The anions, cations, solvents, additives, and concentration have complicated and extremely significant influences on the microstructures, components, stability, and mechanical and ionic transport properties of SEI layer.<sup>[124, 125, 126]</sup> Until now, numerous electrolyte-engineering strategies have been proposed to design thin and stable high-quality SEI, such as altering solvents from carbonates to ethers,<sup>[11, 15, 69, 127]</sup> selecting suitable salts,<sup>[10, 125]</sup> regulating concentration from normal (1 M) to high ( $\geq 3$  M) or localized high concentration,<sup>[8, 52, 128]</sup> introducing SEI film forming additives, utilizing novel ionic liquid electrolytes<sup>[100]</sup> and solid-state electrolytes.<sup>[129, 130]</sup>

(2) **Anodes.** As illustrated in Figure 3a, SEI layer as the significant interface between anode and electrolyte, the physical/chemistry property of the anode is also inevitably an important factor affecting SEI formation. For different active materials, their components, storage mechanism, redox potential, electronic properties, polymorphs, and microstructure could affect the reduction kinetics, leading to different electrolyte decomposition and SEI formation processes.<sup>[131-133]</sup> For example, Song *et al.*<sup>[132]</sup> revealed that monolayer, bilayer, and multilayer graphene with distinct electronic structures exhibited different reduction capabilities, which greatly affected the morphology, component and mechanical properties of SEI. Owing to the decreased reduction kinetics, SEI on the surface of lithiated multilayer graphene was dense and organic-rich species. Li *et al.*<sup>[131]</sup> clarified that regulating anodes can affect the catalytic effect of electrolyte reduction, thus tuning SEI.

Binders and conductive additives as significant anode components are also important factors. Multifunctional binders with unique functional groups could interact with active materials and form an extended coating. It could constrain electrode deformation and promote the formation of thin and stable SEI. Besides, multifunctional binders and well-designed electrode structures



can effectively accommodate large mechanical deformation and maintain intact electrode structure during the repeated cycling process. It abates the freshly exposed interface between electrolyte and anode, and suppresses undesired side reactions, thus slowing down the damage and regeneration of SEI.

(3) **External operation conditions.** Some external conditions, such as current density, cut-off voltage, cell configuration, and operation temperature, have also been evidenced to be critical to the quality of the formed SEI arising from the influence on reaction kinetics.<sup>[84, 98]</sup> Different current density brings about distinct diffusion rate of the charges.<sup>[77]</sup> Smaller current density is prone to inducing thin SEI.<sup>[77]</sup> As aforementioned, operation temperature can affect the initial formation and subsequent stability of SEI during cycling processes (Figure 2h). Recently, Brett's group revealed that the distance between electrodes could affect the components and microstructure of SEI.<sup>[84]</sup> As illustrated in Figure 2i, when increasing the distance between the cathode and anodes to  $\geq 2$  mm, rich-LiF SEI with uniform LiF nanoparticles ( $< 500$  nm) was generated. The coin cell also achieved improved electrochemical performance. However, in a conventional coin cell with a narrow gap  $\sim 0.5$  mm, SEI on the Si anode surface was mainly composed of a mixture of  $\text{Li}_2\text{CO}_3$  and LiF. The comparison highlighted the influence of cell configuration on the SEI layer.

As for the stabilization of SEI layer for microsized alloy anodes, high-quality SEI is the premise, and rationally designed anode structure and proper external operating conditions are the basic guarantees. Designing electrode structures (like artificial SEI layer, 2D layered, 3D porous, defective, or hierarchical structure), utilizing multifunctional binders (like self-healing, highly elastic adhesive), and selecting proper cycle protocols are effective strategies.<sup>[69]</sup> Therefore, in the next section, we summarize current strategies for SEI of microsized alloy anodes from electrolytes, cycle protocols, multifunctional binders, and electrode structural design (**Figure 4, Table 3**).

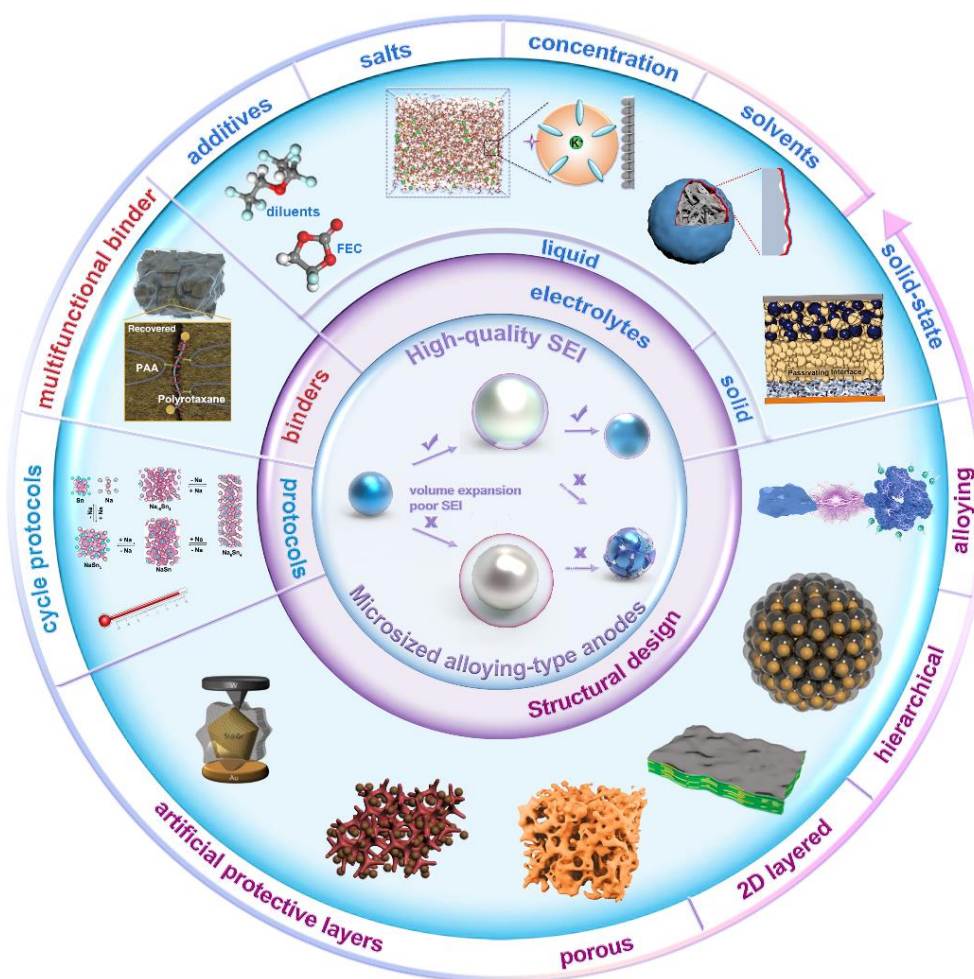


**Figure 4.** Schematic illustration of strategies for stabilizing the SEI layer generated on the surface of alloy anodes in various rechargeable batteries (The insets are reproduced from Ref.<sup>[2, 6, 11, 13, 18, 125, 130, 134-138]</sup> with permission).

### 3. Regulation strategies of SEI layer for microsized alloy anodes

#### 3.1 Electrolytes engineering

The mechanistic understanding regarding the effect of electrolytes on the structure, composition, and properties of SEI layer is critical to developing ideal SEI for microsized alloy anodes. **Table 3** summarizes the electrochemical performance of microsized alloy anode *via* electrolyte regulation strategies, including liquid organic, ionic liquid and solid-state electrolytes.

##### 3.1.1 Liquid organic electrolytes

###### 3.1.1.1 Solvents and salts

Salts and solvents are indispensable and interacting components of liquid organic electrolytes. The reduction of both salts and solvents contributes to the SEI layer for anodes. Hence, the influences of salts and solvents on the SEI layer for microsized alloy anodes are discussed together.

Electrolyte salts consist of anions and cations. The types of rechargeable batteries determine the cation, such as  $\text{Li}^+$ ,  $\text{Na}^+$ ,  $\text{K}^+$ ,  $\text{Zn}^{2+}$ ,  $\text{Ca}^{2+}$ ,  $\text{Mg}^{2+}$  and  $\text{Al}^{3+}$  (**Table 1**). Typical anions include hexafluorophosphate ( $\text{PF}_6^-$ ), sulfonylimide (bis(fluorosulfonyl)imide ( $\text{FSI}^-$ ), bis(trifluoromethanesulfonyl)imide ( $\text{TFSI}^-$ )), borate (like tetrafluoroborate ( $\text{BF}_4^-$ ), bis(oxalato)borate ( $\text{BOB}^-$ ), and oxalato difluoro borate ( $\text{DFOB}^-$ )), *etc.*<sup>[105, 139-142]</sup> For the SEI layer generated on anodes, inorganic components (like fluorides, oxides) are primarily derived from anions decomposition with partial contributions from organic molecules such as FEC.<sup>[29, 139]</sup> Therefore, the anions could remarkably affect the reductive kinetics and features of the SEI layer.<sup>[139, 143]</sup> As illustrated in **Figure 5a**, the  $\text{FSI}^-$  anion in the electrolyte has shown an enhanced re-oxidation reconstruction process of the SEI layer and improved cycling stability than  $\text{PF}_6^-$  in KIBs.<sup>[143]</sup> Molecular orbital energy calculations were performed to predict the reductive stability and the role of anions ( $\text{PF}_6^-$ ,  $\text{FSI}^-$ ,  $\text{TFSI}^-$ ,  $\text{BOB}^-$ ,  $\text{DFP}^-$ ) in building the SEI layer.<sup>[144]</sup> It was discovered that  $\text{PF}_6^-$  had a relatively high reductive stability but was thermodynamically unstable for Li metal anodes. Fortunately, a stable SEI layer generated by pre-reduced salts can effectively suppress salt decomposition. Among these anions, the lowest LUMO energy and chemical hardness of  $\text{BOB}^-$  make it an excellent film-forming salt additive. Compared with  $\text{TFSI}^-$ ,  $\text{FSI}^-$  has similar chemical hardness but lower LUMO energy, further benefiting the formation of SEI layer. The difference highlights the significance of salts in optimizing SEI layer and overall battery performance.

Esters and ethers are the commonly used organic solvents. Until now, carbonate esters, ethers, and phosphates have been widely developed for SEI design of micro-sized alloy anode. For the convenience of comparison, **Table 2** summarizes the abbreviations, 3D conformer, linear formula, molecular weight and melting points of some esters and ethers solvents. According to the chemical structure, carbonate esters can be classified into cyclic carbonate ester (ethylene carbonate (EC) and PC) and linear carbonate ester (ethylmethylcarbonate (EMC), DEC), dimethyl carbonate (DMC)).<sup>[27, 38]</sup> Ethers are organic compounds consisting of ether groups, *i.e.*, R-O-R', where R/R' represents the alkyl or aryl groups.<sup>[141]</sup> The family of ether solvents includes cyclic ethers (*e.g.*, 1,3-dioxolane (DOL), tetrahydrofuran (THF), 4-methyl-1,3-dioxolane (4-MeDOL), 2-methyltetrahydrofuran (2-MeTHF)), linear ethers (*e.g.*, dimethoxyethane (DME or G1), diglyme (G2), tetraglyme (G4), ethylene glycol diethyl ether (EGDEE)),<sup>[126, 145]</sup> crown ethers<sup>[146]</sup> and their derivatives.

#### (1) SEI layer in carbonate-based electrolytes

Carbonate-based electrolytes have been applied in commercial Li-ion batteries, because they generally possess better oxidative stability and higher flash points than ether counterpart.<sup>[141,</sup>

<sup>147]</sup> However, traditional carbonate-based electrolytes for micro-sized alloy anodes encounter numerous obstacles due to the formation of a continuous-thickening, low-quality SEI layer and inferior stability with electrodes. For example, Gao *et al.*<sup>[9]</sup> revealed that SEI formed in carbonate-based electrolytes presented low “maximum elastic deformation energy”. Such SEI layer could be caused by the mechanically fragile interfaces between polymer matrix and inorganic particles (**Figure 2i**). Zhang *et al.*<sup>[15]</sup> demonstrated that SEI layer formed in NaPF<sub>6</sub>-PC with 5wt% FEC was loose due to the high solubility of some SEI components (sodium oxides and carbonates) in PC-based electrolytes.

Stable cycling of micro-sized alloy anode in carbonate-based electrolytes has been reported in KIBs when using bis(fluorosulfonyl)imide(FSI<sup>-</sup>)-based salt.<sup>[62]</sup> Zhang *et al.*<sup>[62]</sup> discovered that KFSI salt in EC/DEC solvent helped form a more stable, uniform, thin, and mechanically robust SEI layer on Bi/rGO anode than KPF<sub>6</sub>. Compared to KPF<sub>6</sub>, KFSI-EC/DEC electrolytes can avoid hydrolysis, preventing the formation of strong Lewis acids (like HF, POF<sub>3</sub>, PF<sub>5</sub>), and suppressing electrolyte decomposition. SEI layer generated in KFSI-based electrolyte was dominated by salt reduction while KPF<sub>6</sub> derived SEI origin from solvent-induced reduction, presenting different SEI formation mechanisms. The nanoindentation test suggested the higher viscoelasticity of Bi/rGO electrodes in KFSI-based electrolytes. Moreover, other alloy anodes (like micro-sized Sn (μSn)) in the KFSI-EC/DEC electrolyte also achieved significantly improved electrochemical performance than that in KPF<sub>6</sub>-EC/DEC electrolyte, highlighting the role of salts in regulating interfacial behaviors and electrochemical performance. The unique function of FSI<sup>-</sup> salt in forming a stable SEI layer was also substantiated by Xie’s research work.<sup>[148]</sup> Compared with 1 M KPF<sub>6</sub>-EC/PC, 1 M KFSI-EC/PC electrolyte for NiCo<sub>2.5</sub>S<sub>4</sub>@rGO anode effectively suppressed side reaction and formed a robust SEI layer.<sup>[148]</sup> Besides, in carbonate electrolytes, LiBF<sub>4</sub>, LiBOB, and LiDFOB salts have also shown higher ion mobility and better rate performance in LIBs at low temperatures than LiPF<sub>6</sub> salt.<sup>[149]</sup>

(2) *SEI layer in ether-based electrolytes*

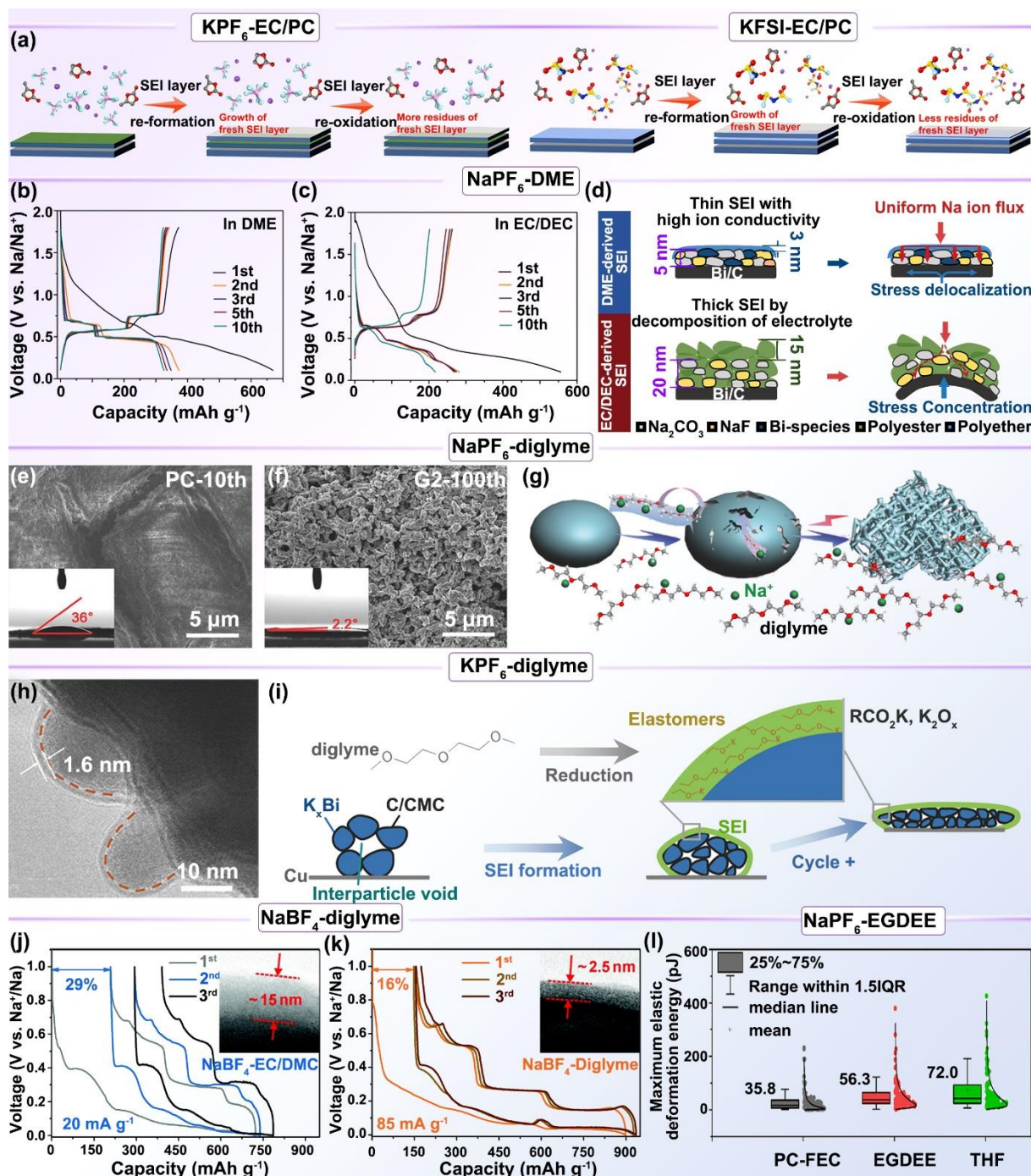


**Figure 5. Electrolyte optimizations.** (a) Illustration on reconstruction process of SEI layer in 1 M KPF<sub>6</sub>-EC/PC and KFSI-EC/PC. Reproduced from Ref.<sup>[143]</sup> with permission. Copyright 2021 Elsevier. Charge/discharge curves of μBi in (b) DME-based and (c) EC/DEC-based electrolytes. (d) Schematic illustration of structure and role of DME- and EC/DEC-derived SEI layer. Reproduced from Ref.<sup>[68]</sup> with permission. Copyright 2020 Wiley. SEM images of bulk Bi anode in (e) NaPF<sub>6</sub>-PC and (f) NaPF<sub>6</sub>-diglyme electrolytes after cycling. (g) Illustration of structural evolution of bulk Bi during the cycling process. Reproduced from Ref.<sup>[150]</sup> with permission. Copyright 2017 Wiley. (h) TEM of μBi anode upon the potassiation in 1 M KPF<sub>6</sub>/diglyme. (i) Illustration of the morphology changes and SEI formation of μBi anode in 1



M KPF<sub>6</sub>-diglyme. Reproduced from Ref.<sup>[69]</sup> with permission. Copyright 2018 Wiley. The first three discharge/charge curves of  $\mu$ Sn anode in 1 M (j) NaBF<sub>4</sub>-diglyme and (k) NaBF<sub>4</sub>-EC/DMC, insets are the corresponding cryo-TEM images of SEI layer. Reproduced from Ref.<sup>[10]</sup> with permission. Copyright 2019 Royal Society of Chemistry. (l) Maximum elastic deformation energy of SEI layer in 1 M NaPF<sub>6</sub> with solvents of PC-FEC, EGDEE, and THF, respectively. Reproduced from Ref.<sup>[151]</sup> with permission. Copyright 2022 American Chemical Society.

Ether-based electrolytes have better reduction stability on the anode side and benefit the formation thinner SEI layer, which is compatible with various anodes.<sup>[15, 152]</sup> As shown in **Table 2**, among ethers, glyme (Gn, CH<sub>3</sub>O(CH<sub>2</sub>CH<sub>2</sub>O)<sub>n</sub>CH<sub>3</sub>) solvent is a big family. With the increase of chain length, the viscosity of glyme solvent increases accompanied by the decrease in ionic conductivity.<sup>[153]</sup> Zhang *et al.*<sup>[15]</sup> pioneered the studies of glyme-based electrolytes for the stabilizing of micro-sized alloy anodes without resorting to electrode microstructural design. They demonstrated the stable cycling of micro-sized Sn in NIBs under 1 M NaPF<sub>6</sub> in G1-G4 electrolytes. The research on glyme-based electrolytes flourished in recent years and has been extended to various anodes.

DME (also named G1), with relatively low viscosity, is among the most popular ether solvents. In 2019, Yang *et al.*<sup>[154]</sup> proved that DME-based electrolytes with NaPF<sub>6</sub> or KPF<sub>6</sub> had better wettability with Bi@N-C electrodes than EC/DEC-based electrolytes, which decreased Na<sup>+</sup>/K<sup>+</sup> diffusion energy barriers. Moreover, the decomposition potential of EC/DEC-based electrolyte (>1 V) was higher than Na-Bi or K-Bi alloying reaction, resulting in the formation of detrimental SEI before the insertion of Na<sup>+</sup>/K<sup>+</sup>, thereby decreasing the initial specific charge capacity.<sup>[68]</sup> In 2020, Yuan *et al.*<sup>[68]</sup> proved that the hierarchical Bi/C anode in 1 M NaPF<sub>6</sub>-DME achieved higher reversibility (Figure 5b), smaller volume variation during the sodiation/desodiation process, lower resistance after cycling than that in 1 M NaPF<sub>6</sub>-EC/DEC-5% FEC (Figure 5c). The results indicated that the 1 M NaPF<sub>6</sub>-DME derived SEI layer for hierarchical Bi/C anode was composed of an interior dense Bi-containing inorganic and external highly ionic conductive polyether layer. Moreover, compared to the loosely distributed SEI in 1 M NaPF<sub>6</sub>-EC/DEC-5% FEC, the DME-derived SEI layer was thinner and denser. A strong binding between the electrode and SEI layer was achieved, giving rise to superior ionic conductivity and robust mechanical properties (Figure 5d).

The longer chain length of diglyme than DME balances the oxidation stability and viscosity, making it a top choice for alloy anodes for compatibility in full cells. In 2016, Zhang *et al.*<sup>[15]</sup> revealed the influences of 1 M NaPF<sub>6</sub> in diglyme and PC+5%FEC on the SEI layer and cycling

stability for  $\mu\text{Sn}$  anode in NIBs. The  $\mu\text{Sn}$  anode in 1 M  $\text{NaPF}_6$ -diglyme electrolyte presented a smoother surface and maintained better structural integrity after 100 cycles and achieved remarkably improved performance. It was mainly attributed to the formation of a dense protective film on  $\mu\text{Sn}$  anode in 1 M  $\text{NaPF}_6$ -diglyme electrolyte. In 2017, Wang *et al.*<sup>[150]</sup> also demonstrated that 1 M  $\text{NaPF}_6$ -diglyme for micro-sized Bi ( $\mu\text{Bi}$ , 200 mesh) induced the formation of sodium alkoxides and polyethers dominated SEI layer, showing better wettability with Bi anode than that of  $\text{NaPF}_6$ -PC electrolyte (Figure 5e-g). Meanwhile, the bulk Bi developed into a porous integrated Bi anode during cycling. As a result,  $\mu\text{Bi}$  in 1 M  $\text{NaPF}_6$ -diglyme achieved high initial Coulombic efficiency (94.8%),  $\sim 400 \text{ mAh g}^{-1}$  capacity, and remarkably enhanced cycling stability. Besides, Huang *et al.*<sup>[69]</sup> demonstrated the stable cycling of  $\mu\text{Bi}$  anode in 1 M  $\text{KPF}_6$ -diglyme electrolyte in KIBs. The  $\mu\text{Bi}$  anode delivered an enhanced initial Coulombic efficiency (83%) and appealing capacity retention of 97% after 100 cycles. The analysis indicated that more potassium oligomers  $[(\text{CH}_2\text{CH}_2\text{-O})_n\text{K}, (\text{CH}_2\text{CH}_2\text{-OCH}_2\text{-O})_n\text{K}]$  with better mechanical flexibility were formed when using  $\text{KPF}_6$ -diglyme, endowing SEI layer with better elasticity (Figure 5h, i). The continuous and elastic SEI well confined the broken Bi microparticles in SEI, mitigating the loss of active materials and preventing the generation of fresh electrode-electrolyte interface.

Except in the  $\text{PF}_6^-$ -diglyme system, Huang *et al.*<sup>[10]</sup> investigated the difference in microstructure, chemical composition and mechanical properties of SEI layer in 1 M  $\text{NaBF}_4$ -diglyme and  $\text{NaBF}_4$ -EC/DMC electrolytes on the  $\mu\text{Sn}$  anodes *via* cryo-TEM, AFM, XPS and DFT calculations. The cryo-TEM of  $\mu\text{Sn}$  anodes after 3 cycles (inset of Figure 5j) demonstrated that  $\text{NaBF}_4$ -EC/DMC induced the formation of thick SEI with polycrystalline domains of  $\text{Na}_2\text{CO}_3$  (and possible NaF). By contrast,  $\text{NaBF}_4$ -diglyme derived SEI (inset of Figure 5k) was ultrathin, consisting of poorly crystallized  $\text{Na}_2\text{CO}_3/\text{NaF}$  dispersed in a polymer-like matrix. Such a feature promotes sodium diffusion, endows SEI with better mechanical properties, and improves ionic conductivity. AFM tests demonstrated that  $\text{NaBF}_4$ -diglyme-derived SEI possessed better stiffness ( $\sim 355 \text{ MPa}$ ) and elasticity ( $\sim 79\%$ ), explaining the improved electrochemical performance in diglyme electrolytes. This work unravels the structural and mechanical origin of stable SEI layers in glyme-based electrolytes.

In addition to chain length, the end-group of linear ether also plays an essential role. By modifying the end-group from methy- of DME to ethyl-, the new ether solvent, ethylene glycol diethyl ether (EGDEE), offers particular benefits in KIBs. Du *et al.*<sup>[33]</sup> discovered the superiority of 1 M KFSI/EGDEE in stabilizing  $\mu\text{Sb}$  anodes. Such an electrolyte promotes the formation of oligomer-like species in SEI layer and endows SEI layer with sufficient elasticity



to accommodate the repeated swelling-contracting. Compared with in 1 M KFSI-EC/PC,  $\mu\text{Sb}$  anode for KIBs in 1 M KFSI-EGDDE presented a higher initial Coulombic efficiency (69.4% > 56.5%), higher reversible capacity (573 mAh g<sup>-1</sup>), and stable long-term cycling performance. The merits of EGDEE in constructing SEI layer could also be extended to  $\mu\text{Sn}$ <sup>[151]</sup> for NIBs and graphite<sup>[155]</sup> for KIBs. As illustrated in Figure 5l, the maximum elastic deformation energy value of SEI layer on  $\mu\text{Sn}$  surface in 1 M NaPF<sub>6</sub>-EGDDE outperformed the one in PC-FEC-based electrolytes,<sup>[151]</sup> further highlighting the advantages of ether-based electrolytes in improving mechanical properties of SEI layer.

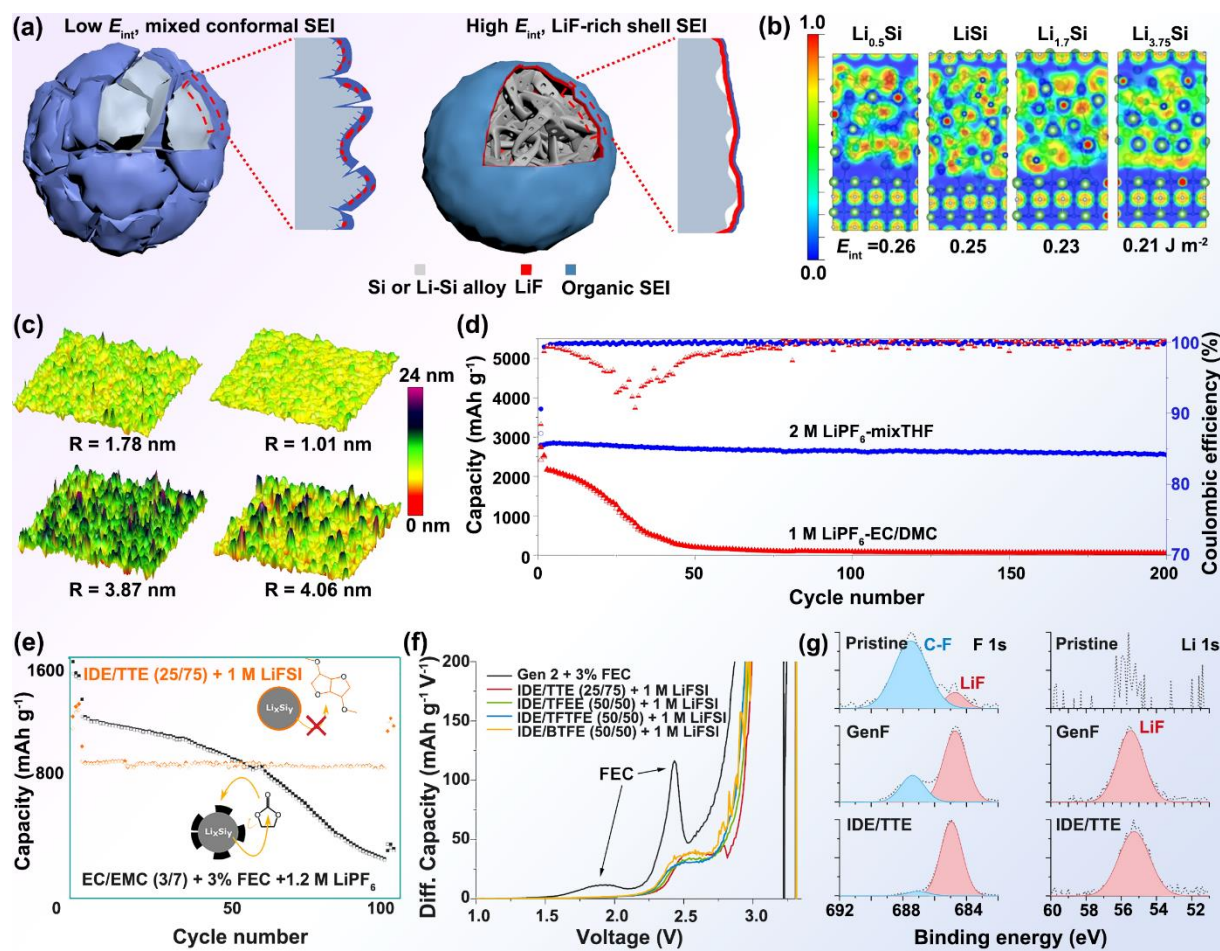


**Figure 6. Cyclic ethers.** (a) The relationship between cycled  $\mu\text{Si}$  electrode and Li alloy-SEI interface. (b) Electron localized function and high interfacial energy ( $E_{int}$ ) for the Li alloy-LiF interface. (c) AFM images of  $\mu\text{Si}$  electrode after 100 cycles and (d) cyclic performance in 2 M LiPF<sub>6</sub>-mixTHF and 1 M LiPF<sub>6</sub>-EC-DMC. Reproduced from Ref.<sup>[11]</sup> with permission. Copyright Springer Nature. (e) Cycling stability and (f) differential capacity plots of LiFePO<sub>4</sub>||Si batteries for isosorbide dimethyl ether/hydrofluoroether (IDE/HFE) electrolytes in comparison to 1.2 M LiPF<sub>6</sub>-3% FEC-EC/EMC. (g) XPS spectra of pristine and cycled  $\mu\text{Si}$  anodes after 100 cycles. Reproduced from Ref.<sup>[127]</sup> with permission. Copyright 2022 American Chemical Society.

The benefits of ether electrolytes could also be applied to the alloy anodes in LIBs. The SEI

layer with high interfacial energy ( $E_{int}$ ) to  $\mu\text{Si}$  anode surface shows a low adhesion the anode surface (**Figure 6a, b**), helping the anode relocation at the interface to better accommodate the volume change.<sup>[11]</sup> Therefore, the high  $E_{int}$  of LiF makes it an attractive component in SEI layer. Ethers possess low thermodynamic reduction potentials of  $\sim 0.0\text{--}0.3$  V, which facilitates preferential fluorinated salt decomposition.<sup>[11, 153]</sup> The poor solubility of  $\text{LiPF}_6$  in linear ethers, such as DME and diglyme, restricts the wide utilization of glyme-based electrolytes in LIBs. Compared to linear ethers, cyclic ethers are seldom used except DOL due to their high chemical reactivity.<sup>[153, 156]</sup> DOL also leads to violent reactions related to the ring-opening and subsequent polymerization reactions. Among the cyclic ethers, THF and 2-MeTHF can shield such reactions owing to the reduced number of ether oxygens (**Figure 6**).<sup>[153, 156]</sup>

Chen *et al.*<sup>[11]</sup> screened salts and solvents for microsized alloy anodes in LIBs by determining salt reduction potential and solvation ability of solvent. They designed a 2 M  $\text{LiPF}_6$  in the mixture of THF and 2-MeTHF (mixTHF) for  $\mu\text{Si}$ ,  $\mu\text{Al}$  and  $\mu\text{Bi}$  ( $>10\ \mu\text{m}$ ) anodes. It demonstrated that a thin, homogeneous and LiF-rich SEI layer was formed in the 2 M  $\text{LiPF}_6$ -THF/2-MeTHF electrolyte (**Figure 6c**). The LiF-rich SEI layer possessed high  $E_{int}$  with the alloy anode to buffer the plastic deformation of lithiated alloy ( $\text{Li}_x\text{Si}$ ) during alloying/dealloying processes. As a result,  $\mu\text{Si}$ ,  $\mu\text{Al}$  and  $\mu\text{Bi}$  anodes achieved a stable capacity of 2800, 970 and 380  $\text{mAh g}^{-1}$ , respectively, with initial CEs of higher of over 90% (**Figure 6d**). Besides, Zhang *et al.*<sup>[156]</sup> adopted 2 M  $\text{LiPF}_6$  2-MeTHF or 2 M  $\text{LiPF}_6$  THF/2-MeTHF as electrolytes to successfully stabilize the SEI layer on  $\mu\text{Sn}$  anode for LIBs. 2-MeTHF-based electrolytes derived SEI on  $\mu\text{Sn}$  anode presented a thin and compact structural feature with abundant LiF, greatly enhancing the cyclic lifespan.

Johnson *et al.*<sup>[127]</sup> employed another cyclic ether solvent, isosorbide dimethyl ether (IDE), to stabilize the surface of microsized Si ( $\mu\text{Si}$ ) anode for LIBs. The nonflammable, nontoxic and commercially available IDE solvent presented low reactivity with  $\mu\text{Si}$  anode owing to the presence of a bicyclic ring. Moreover, 1,1,1-trifluoroethyl-1,1,2,2-tetrafluoropropyl ether (TTE) was introduced into IDE-based electrolytes to decrease the viscosity. Compared with 1.2 M  $\text{LiPF}_6$ -EC/EMC-3% FEC (GenF), the 1 M LiFSI-IDE with TTE diluent showed less reactivity with the electrode surface and achieved higher cycling stability of  $\mu\text{Si}$  anode (**Figure 6e,f**). The negligible organic fluorides and strong LiF peak on the cycled Si surface (**Figure 6g**) proved the inhibited decomposition of organic species in IDE solvent.

### (3) SEI layer in phosphate-based electrolytes

Phosphorus-based solvents (like phosphates, phosphonates, and phosphazenes) are popular owing to their promising prospects in avoiding flammability and enhancing anodic stability

against high-voltage cathodes. The pioneering efforts using phosphorus-based solvents have been summarized in some previous reviews.<sup>[141, 157]</sup> Trimethyl phosphate (TMP) is a typical linear phosphate solvent, which possesses wide liquid-phase temperature ranges from -46 to 197 °C, high dielectric constant (21.6), and low viscosity (2.3 mPa s).<sup>[158-160]</sup> Other phosphate solvents, such as triethyl phosphate (TEP) and dimethyl methylphosphonate (DMMP), also show wide operating temperature, low viscosity, good solubility of salts, and wide electrochemical stability window. Despite numerous advantages, phosphates have poor compatibility with most electrode materials.<sup>[141, 157, 161]</sup> The reason may lie in the poor reductive stability of phosphates, making it difficult to form a stable SEI on the anode surface.<sup>[158, 161-163]</sup> However, when phosphates are used as co-solvents or additives, reductive decomposition can be effectively suppressed, and the nonflammability of electrolytes can be enhanced. Therefore, organic phosphorus-based solvents are inclined to be utilized as non-flammable co-solvents or flame-retardant additives in various rechargeable batteries.<sup>[158]</sup> Furthermore, resorting to the high concentration and localized high concentration concepts, phosphates-based electrolytes with proper concentration realized stable and compact SEI layer on microsized alloy anodes.<sup>[52, 128, 141]</sup> The advances in concentrated phosphate-based electrolytes will be discussed in the following section. Besides, some fluorinated phosphates (*e.g.*, tri(2,2,2-trifluoroethyl) phosphite (FTEP)) also exhibited enhanced oxidative stability and SEI formation capability.<sup>[141, 162]</sup>

### 3.1.1.2 Concentrations

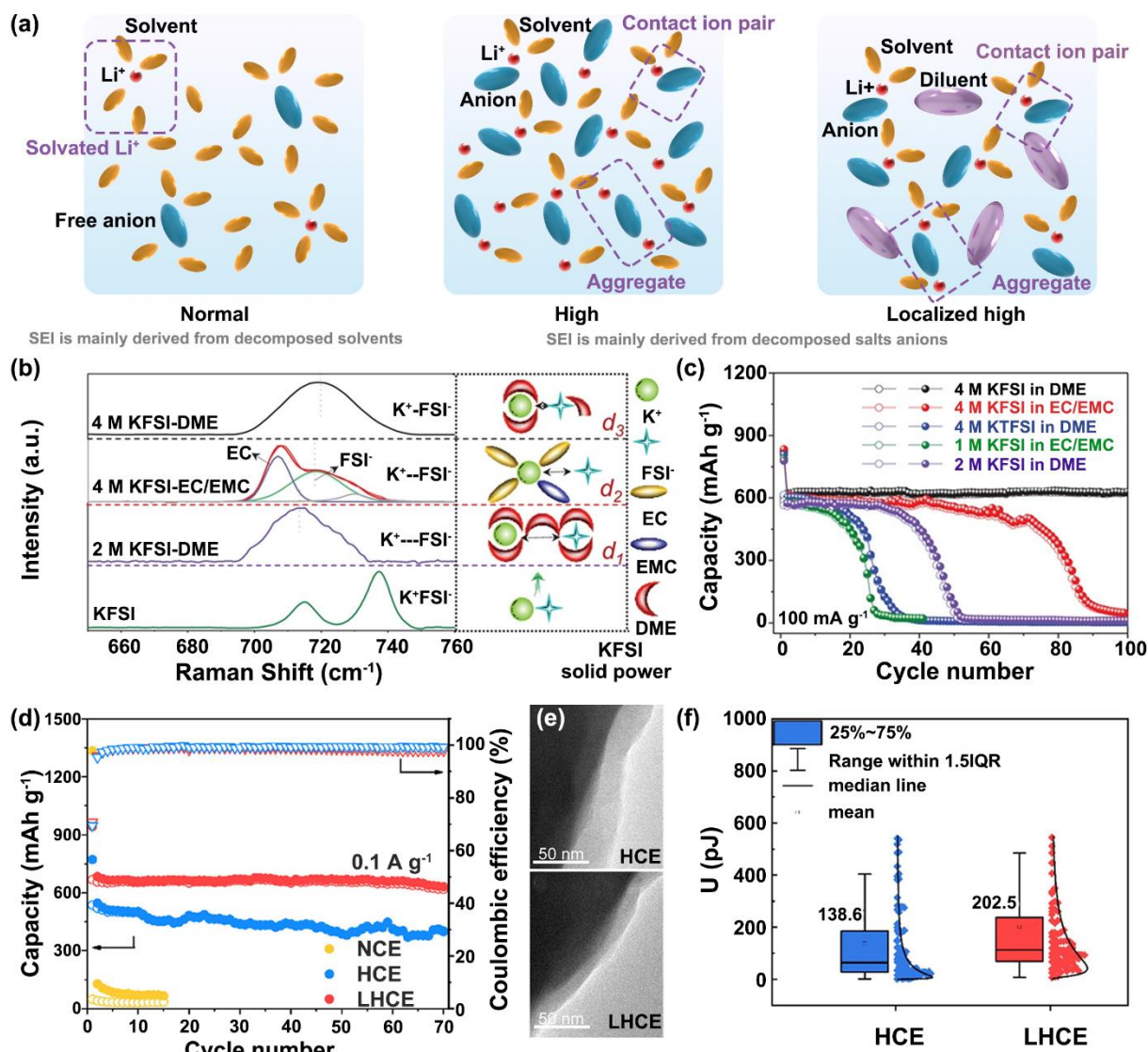


**Figure 7. Electrolyte Concentrations.** (a) The illustration of normal, high and localized concentration electrolytes. (b) Raman spectra of FSI<sup>-</sup> anions and interaction illustration between ions (K<sup>+</sup>, FSI<sup>-</sup>) and solvent in different electrolyte formulations. (c) Cycling performance of micro-sized Sb anode. Reproduced from Ref.<sup>[125]</sup> with permission. Copyright 2020 Wiley. (d) The comparison of cycling performances of P<sub>black</sub>/G anode, (e) TEM of SEI layer after 300 cycles, (f) the maximum elastic deformation energy of SEI in normal, high, and localized high concentration electrolytes. Reproduced from Ref.<sup>[52]</sup> with permission. Copyright 2021 American Chemical Society.

The concentrated electrolyte concept can retrospect to as early as 1985. Dahn *et al.*<sup>[164]</sup> discovered that concentrated LiAsF<sub>6</sub> can suppress the co-intercalation of PC into layered ZrS<sub>2</sub> material. In the past decades, high concentration electrolyte has rapidly flourished. Compared with conventional electrolytes (*e.g.*, 1 M), free solvent molecules in highly concentrated electrolytes are greatly decreased, forming a peculiar 3D solution structure (**Figure 7a**).<sup>[141]</sup> It reduces the chance of interaction between free solvent molecules and anode materials,

indicating improved stability.<sup>[8, 125, 128, 165]</sup> When increasing salt concentration, the anodic stability of ether-based electrolytes will be greatly enhanced, which will promote the implementation in high-voltage battery systems. Moreover, the high salt concentration promotes the formation of a salt-derived SEI layer, which could positively affect the interfacial chemistry on anode surfaces.<sup>[141]</sup> For example, electrolyte stability, interaction strength of FSI<sup>-</sup> and K<sup>+</sup> (Figure 7b), and compatibility with  $\mu$ Sb anode in 4 M KFSI-DME were higher than these in 4 M KFSI-EC/EMC, 2 M KFSI-DME, and 1 M KFSI-EC/EMC.<sup>[125]</sup> Owing to the better stability of K<sup>+</sup>-DME-FSI<sup>-</sup> in 4 M KFSI-DME, electrolyte decomposition was well suppressed, and improved cycling stability was achieved (Figure 7c).<sup>[125]</sup> Besides, in 2021, Wang *et al.*<sup>[165]</sup> developed a 5 M concentrated KFSI-diglyme electrolyte for a hierarchical (BiO)<sub>2</sub>CO<sub>3</sub> anode for KIBs. The increasing concentration from 1 M, 3 M to 5 M decreased the amounts of free diglyme, and promoted the participation of FSI<sup>-</sup>@anion, leading to thin and KF-rich SEI for improved electrochemical performance.

Despite the remarkable advantages, high viscosity, poor wettability and high cost of highly concentrated electrolytes make them arduous for practical applications.<sup>[22]</sup> Fortunately, localized high-concentration electrolyte provides an alternative that can bolster the advantages and mitigate the drawbacks of high-concentration electrolytes. Generally, some diluents with proper amounts will be introduced into the high-concentration electrolytes, which can not only decrease viscosity and improve ionic conductivity but also maintain the advantages of concentrated electrolytes like high oxidative stability and the solvation structure.<sup>[22]</sup> For example, in 2019, Jia *et al.*<sup>[128]</sup> introduced fluorinated bis(2,2,2-trifluoroethyl) ether (BTFE) as a diluent into 1.2 M LiFSI-TEP/FEC (TEP/FEC/BTFE: 1.2/0.13/4), forming a localized high concentration electrolyte for porous  $\mu$ Si. This electrolyte promoted the formation of locally highly coordinated Li<sup>+</sup>-TEP solvates and FSI<sup>-</sup> derived LiF-rich SEI layer. As a result, Si/graphite||NMC333 full cell in 1.2 M LiFSI-TEP/FEC/BTFE presented remarkably improved electrochemical performance than 1 M LiPF<sub>6</sub>-EC/EMC-FEC. In 2021, Du *et al.*<sup>[52]</sup> utilized 1,1,2,2-tetrafluoroethyl-2,2,2-trifluoroethyl ether (HFE) as the diluent in 5 M KFSI-TMP, forming a localized high-concentration electrolyte (KFSI/TMP/HFE: 1/1.7/2, Figure 7d). Compared with 1 M and 5 M KFSI-TMP, SEI layer on P<sub>black</sub>/graphite anode after 300 cycles was still thin and stable in the 5 M KFSI-TMP/HFE (Figure 7e). HFE diluent in 5 M KFSI-TMP enhanced the interaction between cations and anions and promoted the participation of FSI<sup>-</sup> in the K<sup>+</sup> solvation sheath, resulting in the KF-rich SEI layer. Moreover, the SEI formed in localized high-concentration electrolytes presented larger elastic deformation energy (Figure 7f) to tolerate the volume change during potassiation/depotassiation processes.

### 3.1.1.3 Additives

To avoid stress-induced fracture and continuous growth of SEI layer on micro-sized alloy anode, the rational selection and usage of electrolyte additives have been deemed as one of the most cost-effective ways to optimize SEI layer and boost performance.<sup>[35, 127, 166-168]</sup> Therefore, we briefly summarize the progress of additives for micro-sized alloy anodes and analyze the mechanism of different additives in stabilizing SEI layer. The commonly used additives include fluorine (F)-containing species, unsaturated carbonate derivatives, salt type additives,<sup>[167, 169]</sup> *etc.*

F-containing species are popular because they are conducive to the formation of fluorinated species/polymers (*e.g.*, LiF, NaF, KF and analogues).<sup>[127, 170-172]</sup> These components are important for constructing a robust SEI layer to suppress possible side reactions.<sup>[127, 170, 171]</sup> Besides, F-containing species could intrinsically impede oxidation owing to the high electron-withdrawing tendency of the F groups, potentially benefiting the oxidation stability of the electrolytes at high voltages.<sup>[141, 167]</sup> Among these F-rich additives, the best-known are the fluorinated solvents, such as FEC (a fluorinated form of EC),<sup>[166, 173, 174]</sup> 3,3,3-fluoroethylmethyl carbonate,<sup>[175]</sup> and difluoroethylene carbonate.<sup>[36, 176]</sup> In particular, FEC has been utilized as a commercial electrolyte additive. It presents a positive role for micro-sized alloy anode in mitigating the side reaction of electrolyte with electrode and inducing the formation of a stable F-rich SEI layer.<sup>[166, 173, 174, 177]</sup> For example, in 2012, Darwiche *et al.*<sup>[173]</sup> optimized the electrochemical performance of  $\mu\text{Sb}$  anode for NIBs by using FEC additive in 1 M NaClO<sub>4</sub>-PC. Moreover, compared with FEC-free electrolytes,  $\mu\text{Sb}$  anode in FEC-containing electrolyte achieved higher initial Coulombic efficiency and reversible capacity because of the formation of a stable SEI layer. In 2019, Bian *et al.*<sup>[171]</sup> further revealed that the optimum amount of FEC can generate a stable LiF/NaF-rich SEI layer on  $\mu\text{Sb}$  anode for LIBs and NIBs, inhibiting the continuous electrolyte decomposition. Nevertheless, excessive inorganic LiF, NaF, and KF components also made the SEI layer mechanically brittle; thus, the performance improvement for some micro-sized alloy anodes was still limited, as demonstrated by Eom *et al.*<sup>[178]</sup>

Unsaturated carbonate derivatives with unsaturated C-C bonds are also attractive additives.<sup>[141]</sup> Among these candidates, vinyl ethylene carbonate (VC) has been utilized as an indispensable additive in the battery electrolyte industry over the past two decades. VC additive performs the polymerization reaction on the electrode surface, promoting the formation of protective poly(VC) layers.<sup>[141]</sup> In 2016, Dahbi *et al.*<sup>[54]</sup> indicated that both VC and FEC additives in 1 M NaPF<sub>6</sub>-EC/DEC can form stable SEI and protect electrolytes against decomposition but through a distinct passivation process. The comparison demonstrated that



VC-derived SEI was formed based on a polymerization reaction and mainly consisted of inorganic and organic compounds. In contrast, SEI generated in 1 M NaPF<sub>6</sub>-EC/DEC with FEC additive was based on a decomposition reaction, which was mainly composed of inorganic compounds (NaF, Na<sub>2</sub>CO<sub>3</sub>, polyenes, *etc.*).<sup>[54]</sup> This striking contrast demonstrated the influence of different additives on the SEI formation mechanism, components, structure and properties.

Besides, some salts have also been developed as electrolyte additives.<sup>[157, 167, 169]</sup> A commonly used LiNO<sub>3</sub> salt was frequently utilized as an electrolyte additive to protect the Li metal anode by generating a dense inorganic Li<sub>x</sub>NO<sub>y</sub> passivation layer,<sup>[140, 157]</sup> and may be extended to alloy anodes. In 2020, Younesi's group<sup>[35]</sup> employed readily soluble SEI species, Na<sub>2</sub>CO<sub>3</sub> and NaF salts, as additives to saturate the electrolytes. The introduction of NaF salt additive in 1 M NaPF<sub>6</sub>-PC effectively suppressed SEI dissolution and increased NaF content in the SEI layer, promoting the formation of a more inorganic and stable SEI layer. Recently, lithium difluoro(oxalato)borate (LiDFOB) salt as an additive was introduced into 1.5 M LiFSI-DME/HFE (v/v: 4/6) for bulk Sb anode in LIBs. It was found that the LiDFOB salt additive affected the Li<sup>+</sup>/FSI<sup>-</sup> interactions and changed the Li<sup>+</sup> solvation structure.<sup>[179]</sup> The LiDFOB salt additive and HFE diluent synergistically stabilized bulk Sb anode and electrolyte, promoting the formation of a robust SEI and ion transfer. Similarly, NaDFOB has also been adopted to promote the NIBs stability, especially at high temperatures.<sup>[180]</sup> The objective of such salt additives is typically to alter the inorganic components in the SEI to boost the kinetics and chemical/thermal stabilities.

### 3.1.2 Ionic liquid electrolytes

Ionic liquids can be deemed as special salts that are molten below 100 °C or even at room temperature. Ionic liquids present outstanding merits, such as inherent nonvolatility, high oxidative stability, high temperature and chemical stability.<sup>[181]</sup> Replacing the flammable organic electrolytes with one based on ionic liquids could potentially improve safety, widen the voltage window, enhance thermal stability, *etc.*<sup>[100, 181, 182]</sup> Recently, a non-flammable ionic liquid-based electrolyte, lithium bis(fluorosulfonyl)amide (LiFSI) in N-butyl-N-methyl pyrrolidinium bis(fluorosulfonyl)imide (2 M LiFSI/Pyr14FSI), was utilized to improve the performance of μSi anode.<sup>[100]</sup> As illustrated in **Figure 8a**, compared with conventional 1 M LiPF<sub>6</sub>-EC/DMC/DEC, the SEI generated in 2 M LiFSI/Pyr14FSI was dominated by high-temperature-resistant inorganic components (*e.g.*, LiF, LiN<sub>x</sub>, and Li<sub>2</sub>CO<sub>3</sub>). As a result, LiFSI/Pyr14FSI derived SEI layer presented sufficient mechanical strength to tolerate the volume expansion of μSi particles even at high temperatures, leading to the high cycle reversibility and thermal stability of μSi anode. The relatively high and stable initial Coulombic efficiencies at elevated



temperatures in 2 M LiFSI ionic liquid electrolyte provided sufficient proof (Figure 8b).

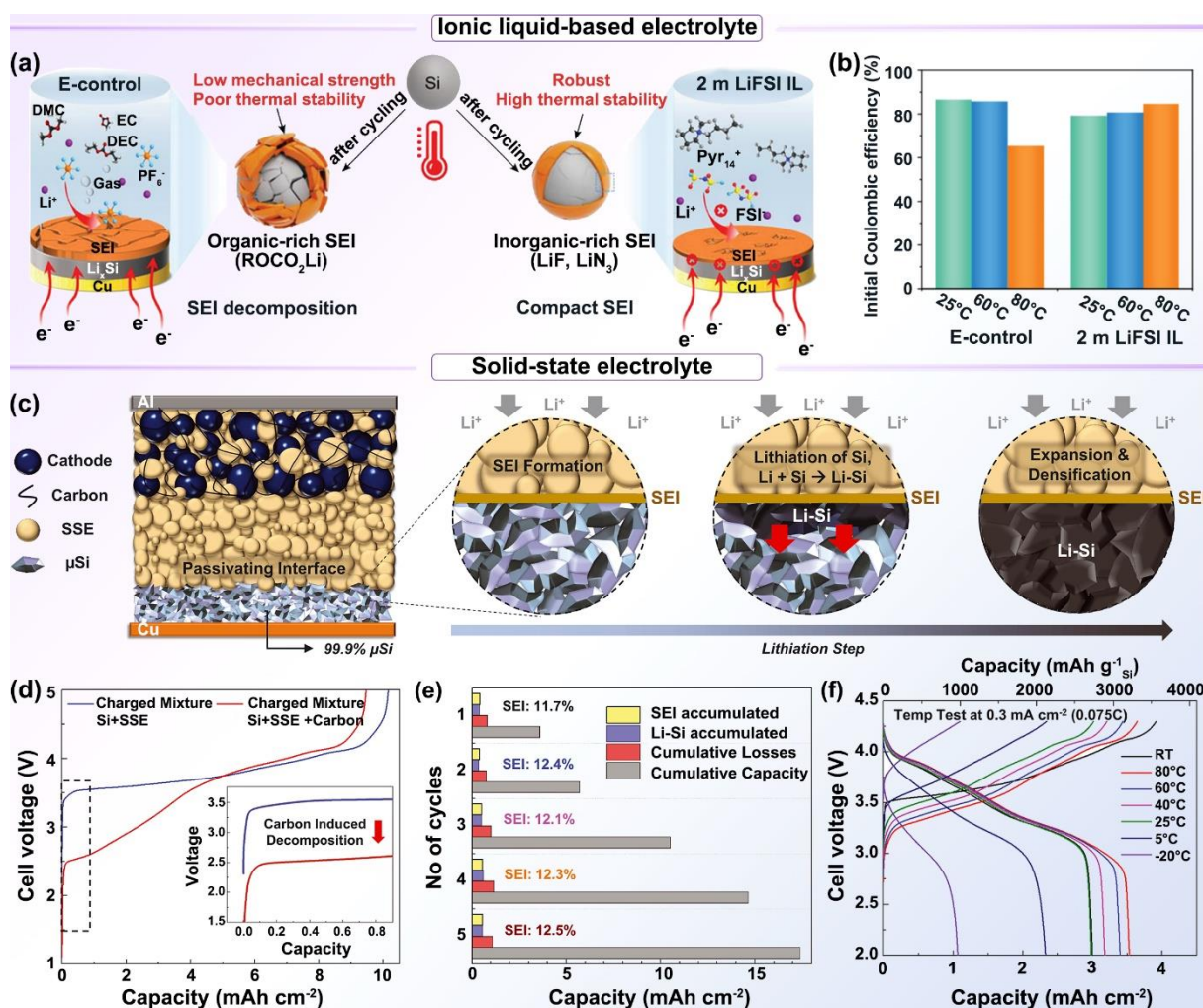


**Figure 8. Ionic liquid and solid state electrolyte.** (a) Illustration of influencing SEI layer and (b) initial Coulombic efficiency of  $\mu\text{Si}$  in ionic liquid-based and carbonate-based electrolytes at different temperatures. Reproduced from Ref.<sup>[100]</sup> with permission. Copyright 2022 Wiley. (c) Illustration for the lithiation process of full cell with carbon-free  $\mu\text{Si}$  anode in solid-state electrolyte. (d) The comparative voltage-capacity profiles, (e) Li-Si and SEI amounts relative to cell capacity. (f) The 1<sup>st</sup> cycle voltage profile of  $\mu\text{Si}||\text{SSE}||\text{NCM811}$  at different operation temperatures. Reproduced from Ref.<sup>[130]</sup> with permission. Copyright the authors and American Association for the Advancement of Science.

### 3.1.3 Solid state electrolytes

Solid-state electrolytes are arising increasing attention owing to their high safety and the capability to induce a stable and passivating SEI layer.<sup>[96, 129, 130, 183]</sup> In 2021, Meng's group utilized the interface passivating properties of sulfide solid-state electrolyte to stabilize carbon-free high-loading (99.9 wt%)  $\mu\text{Si}$  anode.<sup>[130]</sup> As illustrated in Figure 8c, compared with liquid electrolytes, the interfacial contact area between sulfide solid-state electrolytes and porous  $\mu\text{Si}$

anode can be decreased to a 2D plane. The 2D plane can be well preserved and avoid the generation of new interfaces even after  $\mu\text{Si}$  undergoes large volume expansion. Meanwhile, unlike the carbon-containing Si anode, eliminating carbon in the  $\mu\text{Si}$  anode further suppresses the massive decomposition of solid-state electrolyte, achieving remarkably enhanced Coulombic efficiency (Figure 8d). Moreover, Li-Si alloy phase formed upon the lithiation process can propagate throughout the  $\mu\text{Si}$  anode owing to the direct ionic and electronic contact between Li-Si and  $\mu\text{Si}$ . As presented in Figure 8e, the quantitative analysis of the SEI layer, active  $\text{Li}^+$  and capacity loss from 1<sup>st</sup> cycle to 5<sup>th</sup> cycle exhibited minor changes. It demonstrated that sulfide solid-state electrolytes eliminated continuous interfacial growth and irreversible lithium loss, suggesting that the SEI layer was stable upon cycling. Consequently, the carbon-free  $\mu\text{Si}||\text{SSE}||\text{NCM811}$  full cell presented high reversibility even at extreme operation temperatures of  $-20^\circ\text{C}$  and  $80^\circ\text{C}$  (Figure 8f).

### 3.2 Artificial protective layers

The artificial protective layer works as an electrolyte barrier, mechanical buffer layer, and ions transport promoter, which allows targeted tailoring SEI feature on the micro-sized alloy anode surface.<sup>[24, 184]</sup> Designing a proper artificial protective layer has been deemed an effective approach to regulating and stabilizing the SEI layer through tuning electrolyte reduction kinetics.<sup>[58]</sup> For example, mechanical buffer layers have been employed to solve the structural stability challenges of micro-sized alloy anodes.<sup>[185, 186]</sup> The satisfying mechanical properties of the protective layer are conducive to accommodating the volume change of high-capacity alloy anodes and stabilizing native SEI.<sup>[18, 187-190]</sup> Similar to the requirements of native SEI, the design of an artificial protective layer needs to guarantee fast ions transport capability, superior mechanical stability, and chemical/electrochemical and thermal stability. Albeit artificial protective layers have countless advantages, improper design may bring negative effects. For example, introducing an excessive and electrochemically active artificial protective layer could trigger aggravated electrolyte reduction, resulting in a thicker SEI layer and low initial Coulombic efficiency. Therefore, the following aspects mainly discuss design principles and influences of type, distribution, thickness, defects, combination modes (direct mixing or chemical bonding), pore features of the protective layer on electrolyte reduction kinetics and SEI layer.

#### 3.2.1 Inorganic coatings

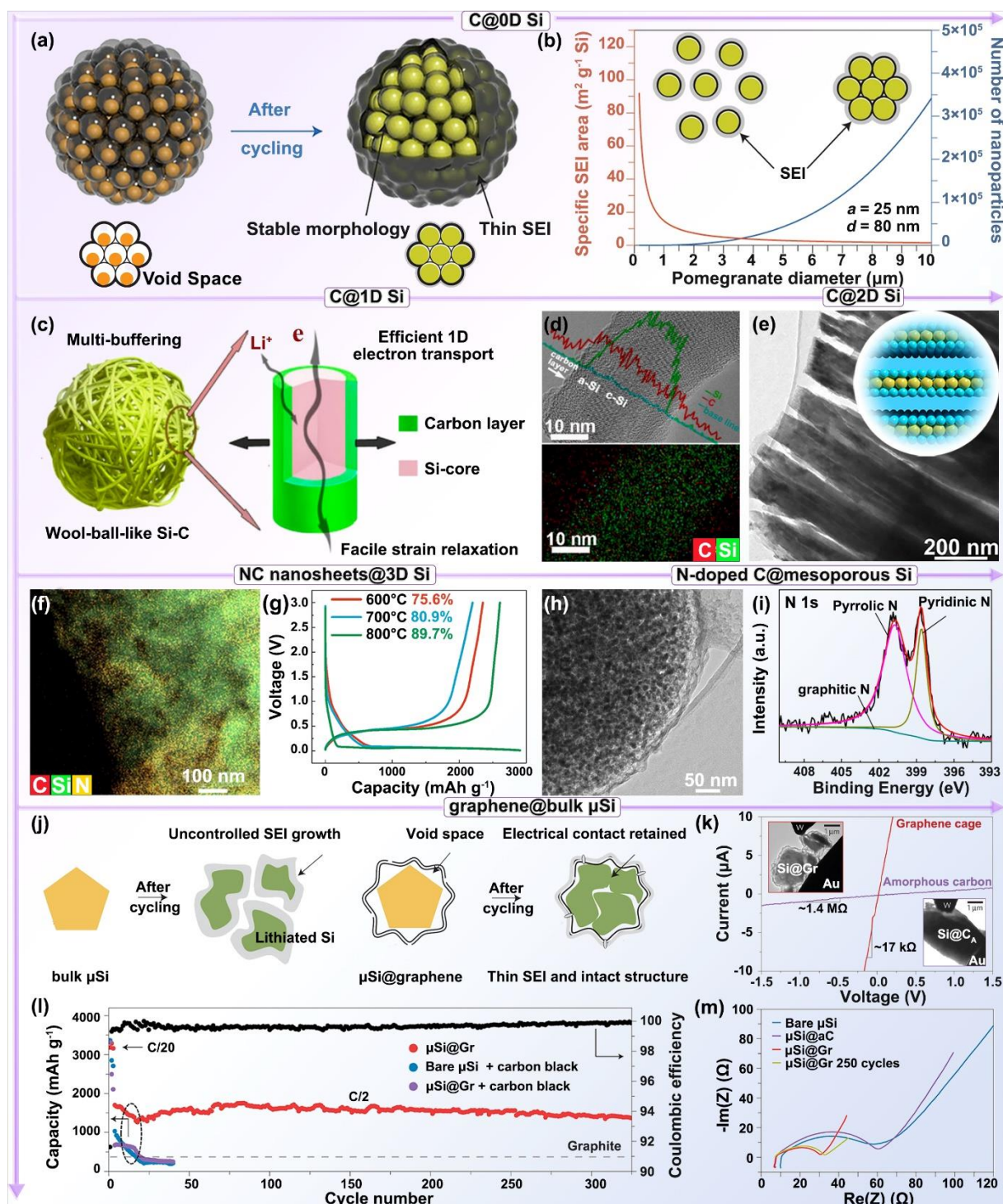


**Figure 9. Carbon-based materials as artificial protective layers.** (a) Illustration for the changes of Si@C pomegranate during the cycling process. (b) The relationship of particle sizes and SEI. Reproduced from Ref.<sup>[6]</sup> with permission. Copyright 2014 Macmillan Publishers. (c) Multiscale buffering mechanism and (d) TEM of micro-sized wool-ball-like  $C@1D$  Si. Reproduced from Ref.<sup>[191]</sup> with permission. Copyright 2019 American Chemical Society. (e) TEM and illustration of layered 2D  $\mu Si@C$ . Reproduced from<sup>[192]</sup> with permission. Copyright 2020 American Chemical Society. (f) The merged TEM mapping. (g) The initial

charge/discharge curves of N-doped carbon nanosheets (NCNFs)@3D $\mu$ Si with different pores and coating thickness. Reproduced from Ref.<sup>[47]</sup> with permission. Copyright 2022 American Chemical Society. (h) TEM and (i) N 1s spectrum of mesoporous  $\mu$ Si@PBI-carbon anode. Reproduced from Ref.<sup>[185]</sup> with permission. Copyright 2017 American Chemical Society. (j) Illustrations of SEI layer for  $\mu$ Si and  $\mu$ Si@graphene after cycling. (k) Electrical behaviors, the comparison of (l) cycling performance and (m) EIS profiles of bulk  $\mu$ Si with different protective layers. Reproduced from Ref.<sup>[18]</sup> with permission. Copyright 2016 Macmillan.

Inorganic conductive carbon-based materials are popular candidates for protective layers on microsized alloy anodes. As early as 2013, Wang's group<sup>[187]</sup> developed a nanoscale carbon layer as building blocks for interconnected Si and constructed a micro-sized Si-C composite anode for LIBs, where the carbon blocks effectively stabilized the formation of SEI layer. Until now, various conductive carbon allotropes, such as carbon (shell or sheet)<sup>[44, 47, 129, 187, 193, 194]</sup> 1D carbon nanotube,<sup>[50, 188, 189, 195-197]</sup> and 2D graphene,<sup>[18, 71, 190, 198, 199]</sup> have been introduced into volume-sensitive microsized alloy anodes and successfully utilized as the protective layer. To promote the positive regulation effect of a carbon-based protective layer on SEI, the configurations, distribution, graphitization degree, defects, and pore features should be rationally tailored.

Carbon-based materials as an external shell to encapsulate inner active materials is the most common protective approach. For instance, in 2014, Cui's group designed a pomegranate-like hierarchical structured Si anode.<sup>[6]</sup> As illustrated in **Figure 9a**, Si nanoparticle was encapsulated into a self-supporting conductive carbon framework, and numerous carbon encapsulated Si hybrids were assembled into pomegranate-like microsized Si-C particles. The external conductive carbon shell served as an electrolyte barrier, blocking electrolytes and avoiding SEI formation in the inner Si nanoparticles. Moreover, the pomegranate-like structure further greatly decreased the SEI formation area due to efficient packing (Figure 9b). Meanwhile, the proper void space between the conformal carbon shell and inner nano-Si provided adequate space to buffer volume changes without damaging the overall pomegranate Si-C anode. As a result, the SEI layer on the overall pomegranate Si-C surface can maintain a thin and integral structure during repeated cycles. Besides, the conjoint carbon shell formed a 3D conductive framework, facilitating rapid ions transport. Therefore, such hierarchical microsized pomegranate-like Si-C anode achieved up to 99.87% average Coulombic efficiency and 97% capacity retention after 1000 cycles.

Similarly, some microsized hierarchical structures composed of conductive carbon shells encapsulated 1D or 2D or 3D active materials also presented a similarly positive role in forming



thin SEI and stabilizing SEI during repeated cycling. As illustrated in Figure 9c, Hou *et al.*<sup>[191]</sup> utilized a conductive carbon shell to encapsulate 1D Si nanowires and devised a microsized wool-ball-like Si-C framework. Figure 9d exhibited a typical morphology of single Si-C nanowires. The wool-ball-like Si-C anode maintained structural integrity with a  $\sim 19.5\%$  volume variation during the lithiation process and induced the formation of thin SEI layer, finally enabling a stable cycling performance upon 1000 cycles. Recently, An *et al.*<sup>[192]</sup> devised a layer-by-layer-assembled Si/C (L-Si/C) anode for LIBs. The TEM image of L-Si/C fabricated at  $650^\circ\text{C}$  (Figure 9e) demonstrated that 2D layered Si was modified by an external carbon layer with an optimal thickness of  $\sim 15.3$  nm and graphitization degree. The optimal microsized L-Si/C anode achieved capacity retention of 82.85% at  $5\text{ A g}^{-1}$  upon 3200 cycles. For these microsized hierarchical structures, external conductive carbon shell mainly serves as electrolyte barriers, elastic buffer, and electrons/ions transport promoter. On the one hand, the external carbon layer blocks direct contact between active materials and electrolytes, alleviates electrolyte consumption, and induces the formation of thin SEI. On the other hand, a carbon shell with proper space can allow for volume variation of high-capacity alloy anodes without deforming carbon shell or disrupting SEI layer on the outside surface, and thus avoiding continuous SEI growth during repeated cycles. Moreover, the overall hierarchical structure provides sufficient space to further alleviate inherent volume changes and inner stresses, thus maintaining an integrated electrode framework and thin SEI while maintaining a high tap density.

The thickness of the protective layer is also an important parameter. An *et al.*<sup>[47]</sup> devised uniform 2D N-doped carbon nanosheet frameworks (NCNFs) as a protective layer for nanoporous  $\mu\text{Si}$  anode ( $\text{NP}\mu\text{Si}@$ NCNFs, Figure 9f) by the pyrolysis of  $\text{g-C}_3\text{N}_4$ . The thickness of NCNFs fabricated at 600, 700, and  $800^\circ\text{C}$  was 27.7, 30.3 and 21.5 nm, respectively. As shown in Figure 9g,  $\text{NP}\mu\text{Si}@$ NCNFs anodes with thinner NCNFs achieved higher initial Coulombic efficiency, indicating fewer electrolytes and Li ions consumption. The investigation demonstrated that the proper thickness of the artificial layer was essential for the formation of thin SEI.

Tailoring defects and surface functional groups is also an effective approach to control the catalytic degree of active materials on electrolyte reduction, electrochemical active sites, conductivity, and mechanical properties of materials.<sup>[131]</sup> For instance, in 2017, Nie *et al.*<sup>[185]</sup> fabricated a conductive pyrrolic N-enriched carbon from polybenzimidazole (PBI) to encapsulate  $\mu\text{Si}$  spheres (Figure 9h). Unlike ordinary carbon, in addition to working as electrolyte barriers to suppress side reaction, pyrrolic N-enriched carbon (Figure 9i) provided

massive extrinsic defects and active sites for extra Li storage, and endowed  $\mu\text{Si}$  with enhanced electronic conductivity and structural robustness. However, massive defects also could trigger severe electrolyte reduction due to large amounts of active sites, resulting in large irreversible capacity, low initial Coulombic efficiency, the formation of thick SEI, and poor cycling performance.<sup>[131, 200]</sup> Therefore, rational defect design is necessary for tailoring SEI layer.

Besides, the combination mode between the protective layer and active material also has an important impact on the stability of SEI. Yu *et al.*<sup>[193]</sup> demonstrated that  $\text{P}_{\text{red}}$  confined within microporous carbon ( $\text{P}_{\text{red}}@\text{YP}$ ) can better accommodate volume change and stabilize SEI, achieving 99% average Coulombic efficiency upon 1000 cycles. However, unconfined  $\text{P}_{\text{red}}$  on the surface of CNT formed unstable SEI during sodiation/desodiation processes. The distinct comparison demonstrated the roles of combination modes. Moreover, the activity, stability and reversibility of electrode materials could be simultaneously boosted when a chemical interaction (strongly coupled) between active species and the protective layer occurs. Song *et al.*<sup>[201]</sup> devised a carboxyl group-functionalized CNTs chemically coupled  $\text{P}_{\text{red}}$  anode *via* P-O-C bonds (P-CNT/c-NaCMC-CA). Compared with directly mixed P-CNT anode, P-O-C bonds in P-CNT hybrids help intensify the close electrical contact between  $\text{P}_{\text{red}}$  and CNTs, enabling a stronger tolerance for repeated volume changes. As a result, P-CNT/c-NaCMC-CA with robust chemical bonding realized lower interfacial resistance and more stable SEI after long-term cycling.

Compared with ordinary carbon, 2D graphene possesses superior mechanical flexibility, electrical conductivity and thermal properties, presenting the promising potential to address both particle fracture of high-capacity alloy anode and unstable SEI layer.<sup>[37, 202]</sup> As early as 2015, Sun *et al.*<sup>[203]</sup> reported a sandwiched phosphorene-graphene composite anode for NIBs, delivering average Coulombic efficiencies of 97.6% ( $8 \text{ A g}^{-1}$ ) and 99.3% ( $26 \text{ A g}^{-1}$ ) in the initial hundred cycles. High Coulombic efficiency indicates high reversibility and superior stability of the electrode and SEI layer. Except for micro-sized 2D materials, graphene also presents extraordinary improvement for bulk micro-sized alloy anode in stabilizing SEI and optimizing electrochemical performance. For instance, Li *et al.*<sup>[18]</sup> adopted the conformal multilayered graphene cages to encapsulate bulk Si microparticles (Figure 9j-m). Compared with bare or amorphous carbon-modified bulk  $\mu\text{Si}$ , the mechanically robust, flexible and conductive graphene cage provided enough space to buffer the anisotropic expansion of bulk  $\mu\text{Si}$  particles, protected cracked  $\mu\text{Si}$  against electrolyte decomposition, avoided the repeated damage and generation of SEI, and maintained superior electrical contact. As a result, the graphene-encapsulated Si micro-sized anode for LIBs achieved high initial- and later-cycle Coulombic

efficiencies (Figure 9l) as well as fast charge-transfer kinetics (Figure 9m).<sup>[18]</sup>

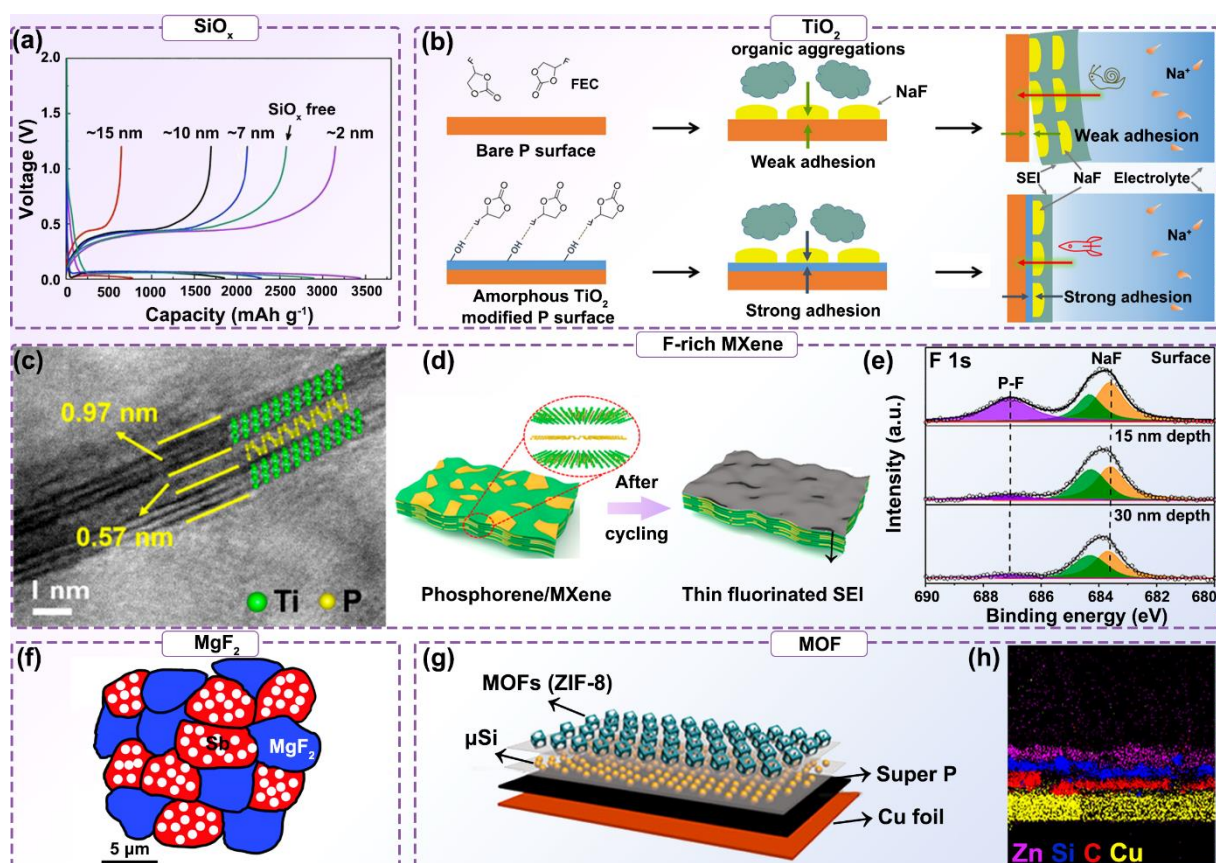


**Figure 10. Inorganic coatings (oxides, MOF, rich-F MXene) as artificial protective layers.** (a) Initial charge/discharge curve of bulk  $\mu\text{Si}$  with  $\text{SiO}_x$  coating of different thicknesses. Reproduced from Ref.<sup>[204]</sup> with permission. Copyright 2013 Wiley. (b) Influence mechanism of amorphous  $\text{TiO}_2$  coating on SEI formation on  $\text{P}_{\text{red}}$  surface. Reproduced from Ref.<sup>[170]</sup> with permission. Copyright 2019 American Chemical Society. (c) HRTEM, (d) illustration of phosphorene/MXene promoting stable SEI and fast reaction kinetics, and (e) F 1s XPS in-depth analysis of SEI layer formed on a phosphorene/MXene. Reproduced from Ref.<sup>[137]</sup> with permission. Copyright 2020 American Chemical Society. (f) Macroporous bulk  $\text{Sb}/\text{MgF}_2$ . Reproduced from Ref.<sup>[205]</sup> with permission. Copyright 2018 Wiley. (g) Schematic illustration and (h) cross-sectional SEM of ZIF-8 modified  $\mu\text{Si}$  anode. Reproduced from Ref.<sup>[206]</sup> with permission. Copyright 2015 American Chemical Society.

In addition to inorganic carbon-based materials, other coatings with unique functions, such as oxides and F-rich species, have also been utilized as efficient protective layers. Oxides (e.g.,  $\text{SiO}_x$ ,<sup>[129, 204]</sup>  $\text{ZrO}_2$ ,  $\text{Al}_2\text{O}_3$ , and  $\text{TiO}_2$ <sup>[207]</sup>) as a protective layer can work as a ceramic stabilizer for micro-sized alloy anodes to constrain large volume variation and stabilize the electrode/electrolyte interfaces. However, similar to carbon-based materials, most oxides can be used as active materials for Li, Na, K, Mg, and Al storage. In the initial alloying process,



some oxide-based protective layers will participate in SEI formation due to the reactions between oxides and cations ( $\text{Li}^+$ ,  $\text{Na}^+$ , *etc.*). Therefore, it is necessary to rationally regulate the features (*e.g.*, thickness, species) of such a protective layer to achieve optimal improvement for SEI in the balance of positive and negative effects. For example, in 2013, Sim *et al.*<sup>[204]</sup> investigated the influence of  $\text{SiO}_2$  coating with different thicknesses (0, 2, 7, 10, and 15 nm) on the initial Coulombic efficiency and electrochemical performance of micro-nano hierarchical Si. As shown in **Figure 10a**, compared with free and thicker  $\text{SiO}_x$  coating,  $\mu\text{Si}$  anode with proper coating thickness (2 nm) exhibited a higher initial Coulombic efficiency. It highlighted the critical role of oxide coating with proper thickness in forming thinner and more stable SEI.

Besides, chemical bonding between the oxides layer and active materials also plays a vital role in regulating SEI. As illustrated in Figure 10b, Zhang *et al.*<sup>[170]</sup> demonstrated that amorphous  $\text{TiO}_2$  coating on the surface of  $\text{P}_{\text{red}}$  anode can interact with the reduction product (*e.g.*, NaF, organic components) of FEC additive, suppress further electrolyte decomposition, and form strong adhesion between  $\text{P}_{\text{red}}$  with SEI. Hence, for  $\text{P}_{\text{red}}$  anode with amorphous  $\text{TiO}_2$  coating, the mechanical damage of SEI during repeated sodiation/desodiation processes was effectively suppressed to achieve enhanced electrochemical performance.

Oxides can also serve as a sacrifice layer to regulate SEI. Luo *et al.*<sup>[207]</sup> developed an ultrathin  $\text{TiO}_2$  nanocoating for microsized  $\text{P}_{\text{black}}$  anode. The  $\text{TiO}_2$  nanocoating induced the formation of a stable  $\text{Li}_x\text{Ti}_y\text{O}_z$  passivation layer and regulated SEI microstructure. The  $\text{Li}_x\text{Ti}_y\text{O}_z$  passivation layer facilitated fast ions/electrons transfer and promoted the formation of a thin SEI layer.

F-rich species are also promising candidates for constructing a protective layer of alloy anodes. Guo *et al.*<sup>[137]</sup> introduced fluorine terminated 2D  $\text{Ti}_3\text{C}_2\text{T}_x$  MXene into  $\text{P}_{\text{black}}$  anode (Figure 10c,d). As shown in Figure 10e, the in-depth XPS analysis proved that  $\text{Ti}_3\text{C}_2\text{T}_x$  with abundant F groups could benefit the formation of stable NaF-rich SEI even in a F-free carbonate electrolyte. DFT calculations clarified the improved diffusion kinetics and sodium affinities in the phosphorene/ $\text{Ti}_3\text{C}_2\text{F}_2$ . As a result,  $\text{P}_{\text{black}}/\text{MXene}$  hybrid anode achieved 535  $\text{mAh g}^{-1}$  reversible capacity at 100  $\text{mA g}^{-1}$  and stable cycling performance (343  $\text{mAh g}^{-1}$  after 1000 cycles at 1000  $\text{mA g}^{-1}$ ) in 1 M  $\text{NaClO}_4\text{-EC/PC}$ . The investigation provided a novel and effective way to regulate SEI composition and stabilize the structure. Ruiz *et al.*<sup>[205]</sup> adopted the electrochemically inactive dense  $\text{MgF}_2$  phase to modify macroporous Sb anode for NIBs. The  $\text{MgF}_2$  phase serves as a mechanical buffer to alleviate part of phase transformation-induced stresses (Figure 10f). Besides, metal-organic framework (MOF)<sup>[206]</sup> with large pore volume and high surface area has also been utilized to modify  $\mu\text{Si}$  anode (Figure 10g,h), where MOF can effectively decrease the direct exposure of  $\mu\text{Si}$  with electrolyte and promote the formation of

stable SEI layer.

### 3.2.2 Organic coatings

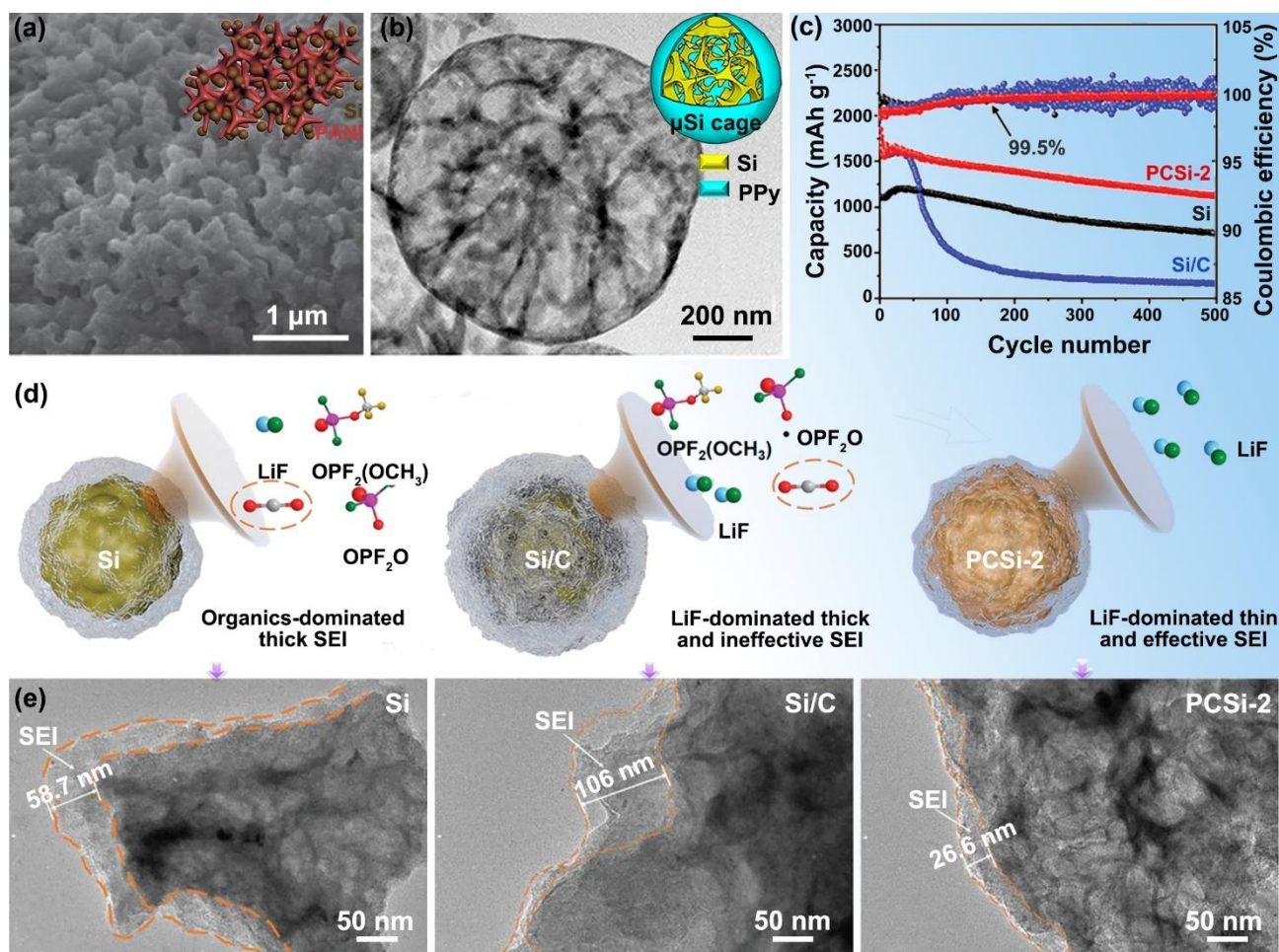


**Figure 11. Organic coating.** (a) Schematic illustration and SEM image after 2000 cycles of 3D porous Si/PANI polymer hydrogel anode. Reproduced from Ref.<sup>[13]</sup> with permission. Copyright 2013 Macmillan Publishers Limited. (b) Schematic illustration and TEM image of  $\mu$ Si cage. Reproduced from Ref.<sup>[208]</sup> with permission. Copyright 2019 American Chemical Society. (c) Cycling performance, (d) schematic illustration for structural and SEI characteristics, and (e) TEM images of Si, Si/C, and PCSi-2 anodes after 50 cycles. Reproduced from Ref.<sup>[134]</sup> with permission. Copyright 2022 Wiley.

Polymer materials with superior processability, high flexibility and good ionic conductivity are deemed ideal artificial protective layer materials.<sup>[209]</sup> Organic polymers, such as polyacrylonitrile,<sup>[210]</sup> polyaniline (PANI),<sup>[13]</sup> polypyrrole (PPy)<sup>[208]</sup> are also promising for solving the large volume change and inducing the formation of high-quality SEI. As shown in **Figure 11a**, Wu *et al.*<sup>[13]</sup> adopted an *in-situ* polymerization approach to incorporate a conductive bi-functional conformal PANI polymer coating onto the  $\mu$ Si anode surface. The 3D polymer created a continuous electronic transport pathway and provided a free space for the volume

expansion of Si particles. Moreover, the positively charged PANI hydrogel layer and  $\mu\text{Si}$  were tightly bonded together by hydrogen bonding or electrostatic adsorption. These features promoted close electrical contact, avoided pulverization of Si particles, and protected thin SEI layers from damage. In 2019, Lv *et al.*<sup>[208]</sup> introduced an ultrathin ( $<5$  nm) mesoporous PPy layer for  $\mu\text{Si}$  anode *via in-situ* polymerization. As shown in Figure 11b, the mesoporous conductive PPy layer encapsulated the entire hollow  $\mu\text{Si}$  skeleton. The external PPy layer promoted fast ions/electrons transport, served as a protective layer to stabilize  $\mu\text{Si}$  anode and suppressed undesired side reactions. Moreover, the hollow  $\mu\text{Si}$  skeleton provided abundant space to buffer drastic volume variation during cycling processes. Inheriting from the structural advantages of hollow Si skeleton and the conductive polymer layer,  $\mu\text{Si}$  anode realized  $\sim 1660$  mAh  $\text{g}^{-1}$  and Coulombic efficiency of  $\sim 99.8\%$  and  $99.4\%$  after 500 cycles with a mass loading of 3 and  $4.4$  mg  $\text{cm}^{-2}$ , respectively.

The electrochemically active polymer layer could regulate and stabilize SEI by affecting the formation pathway of SEI. For example, Wang *et al.*<sup>[134]</sup> introduced poly(hexaazatriphthalene) (PHATN) polymer layer onto  $\mu\text{Si}/\text{C}$  anode surface (denoted as PCSi). Compared with bare Si and Si/C anodes, the PCSi anode for LIBs achieved remarkably improved cycling stability (Figure 11c). The detailed analysis demonstrated that the introduction of the PHATN layer changed the formation path of SEI owing to the fact that PHATN with  $-\text{C}=\text{N}-$  groups possessed a strong lithium affinity than solvent. As illustrated in Figure 11d, during the lithiation of the PCSi anode, Li ions were easily intercalated into PHATN owing to the  $-\text{C}=\text{N}-$  groups, forming a stable Li-rich PHATN layer. Li-rich PHATN interface can promote rapid ions transport, optimize the growth path of SEI, and induce the LiF-rich SEI. Besides, PHATN created a self-healing hydrogen bond framework, which offered controllable space to accommodate the volume change of  $\mu\text{Si}$  particles. By contrast, the formation of SEI on the  $\mu\text{Si}$  with ordinary carbon was induced by successive decomposition of  $\text{LiPF}_6$  salt and carbonate solvent, which was totally different from PCSi. The comparison of TEM images (Figure 11e) of Si, Si/C, and PCSi-2 anodes after 50 cycles obviously demonstrated that PCSi could form thin and stable SEI. The remarkably improved cycling stability of the PCSi anode for LIBs confirmed the effectiveness of the PHATN polymer protective layer in stabilizing  $\mu\text{Si}$  and SEI.

### 3.3 Cycle protocols

The formation processes and resultant properties of SEI are sensitive to external conditions, such as temperature,<sup>[83]</sup> current parameters,<sup>[77, 211, 212]</sup> cut-off voltage,<sup>[138]</sup> distance between electrodes,<sup>[84]</sup> and pressure. For example, Stetson *et al.*<sup>[83]</sup> unveiled that SEI dissolution was more severe at higher operation temperatures (Figure 2h), demonstrating the temperature-

dependent solubility of SEI. Zhu *et al.*<sup>[138]</sup> investigated the influence of desodiation cut-off voltage on the stress level and electrochemical performance of  $\mu\text{Sn}$  anode for NIBs. They revealed that the crucial  $\text{Sn}/\text{NaSn}_3$  phase transition was highly responsible for causing mechanical damage, as revealed by the DFT and finite element analysis. As a result, they precisely regulated the cutoff voltages to tune the phase transition and avoid the formation of  $\text{NaSn}_3$  phase during electrochemical cycling processes. This investigation provided a novel way to suppress particle pulverization of micro-sized alloy anode and avoid the repeated generation of SEI layer. Liu *et al.*<sup>[77]</sup> adopted a small pre-cycling current in the first several cycles to induce the formation of stable SEI at the initial stage, which was deemed a direct and effective strategy. These cases highlight the effectiveness of setting appropriate cycle protocols in regulating and stabilizing the SEI layer on the surface of micro-sized alloy anodes.

### 3.4 Electrode design

#### 3.4.1 Active materials design

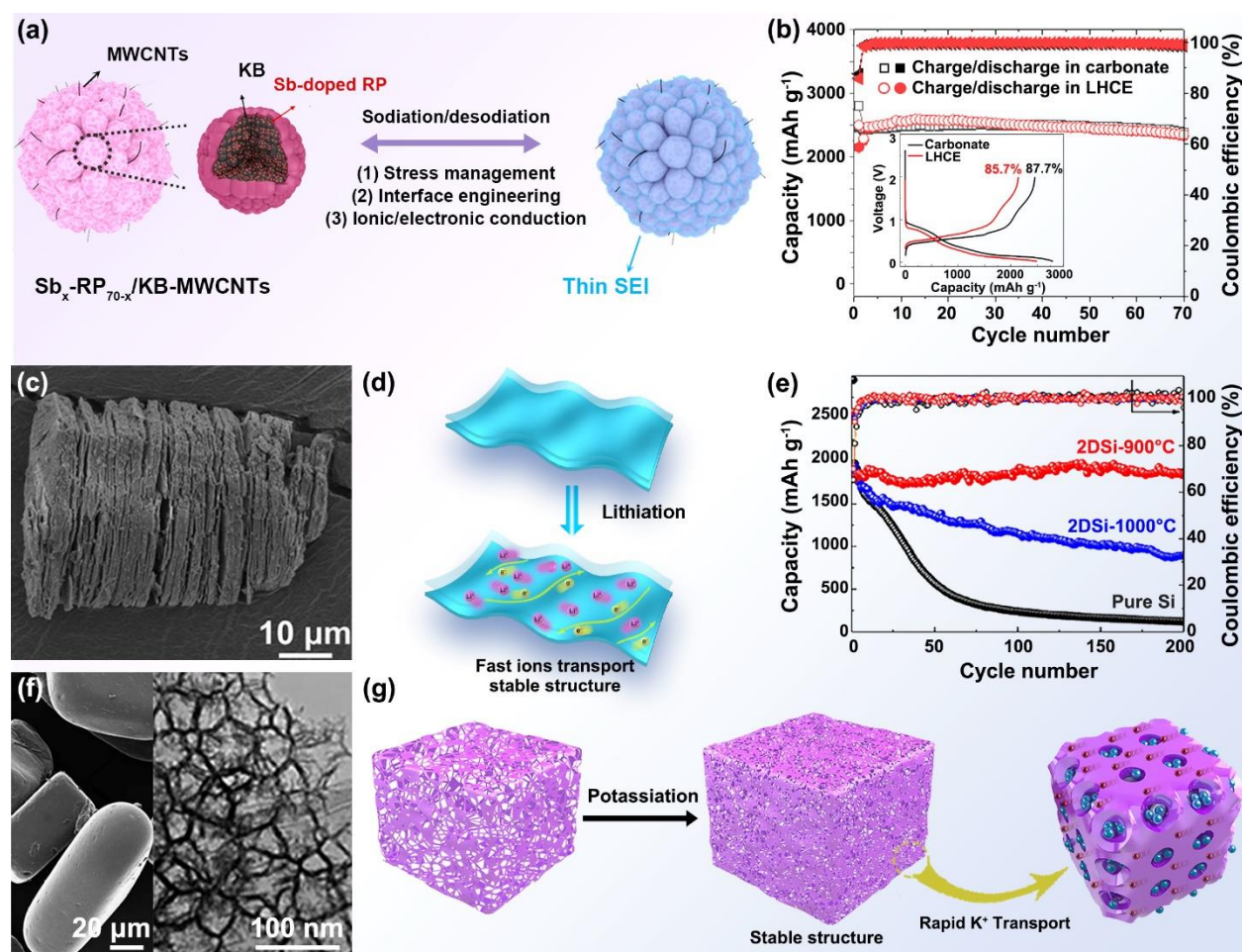


**Figure 12. Multiscale structural design.** (a) Schematic illustration and (b) cycling performance in carbonate and ether-based electrolytes of hierarchical micro/nanostructured  $\text{Sb}_x\text{-RP}_{70-x}/\text{KB-MWCNTs}$ . Reproduced from Ref.<sup>[50]</sup> with permission. Copyright 2021

American Chemical Society. (c) SEM and (d) schematic illustration of 2D layered  $\mu\text{Si}$ . (e) The comparison of cycling performance. Reproduced from Ref.<sup>[46]</sup> with permission. Copyright 2020 American Chemical Society. (f) SEM and TEM of mesoporous Si sponge. Reproduced from Ref.<sup>[213]</sup> with permission. Copyright 2014 Macmillan. (g) Schematic of potassiation process for nanoporous  $\mu\text{Sb}$  anodes. Reproduced from Ref.<sup>[16]</sup> with permission. Copyright 2018 American Chemical Society.

Rational structural design can induce a preferred salt-driven decomposition while selectively suppressing the electrolytes solvents decomposition, thereby inducing thin and robust SEI in ordinary electrolytes.<sup>[50, 131]</sup> Multiscale electrode structure is a good choice. As aforementioned in the inorganic coating, a multiscale structure composed of primary and secondary particles has remarkable advantages to accommodate mechanical stress caused by large volume variation of high-capacity alloy anodes during repeated cycles. For example, in 2021, Liu *et al.*<sup>[50]</sup> constructed a hierarchical micro/nanostructured Sb-doped  $\text{P}_{\text{red}}/\text{KB-MWCNTs}$  anode for NIBs (**Figure 12a**). Both experimental and theoretical results consistently demonstrated that the hierarchical Sb-doped  $\text{P}_{\text{red}}/\text{KB-MWCNTs}$  could greatly accommodate mechanical stress and suppress undesirable electrolyte decomposition regardless of electrolytes. As shown in Figure 12b, Sb-doped  $\text{P}_{\text{red}}/\text{KB-MWCNTs}$  anodes in conventional carbonate (1 M  $\text{NaPF}_6\text{-PC}$  with 2% FEC) and localized high concentration (1.2 M  $\text{NaFSI-DME/BTFE}$ ) electrolytes delivered similar initial Coulombic efficiency and cycling stability, highlighting the vital role of structural design. Compared with  $\text{P}_{\text{red}}/\text{C}_{30}$ , the XPS results demonstrated that Sb-doped  $\text{P}_{\text{red}}/\text{KB-MWCNTs}$  in two electrolytes could induce F-rich, thin and robust SEI layer through regulating the electrolyte decomposition.

Furthermore, microsized 2D layered and 3D porous structural electrodes, such as 3D macroporous Si,<sup>[214]</sup> mesoporous Si,<sup>[213]</sup> nanoporous Si,<sup>[45]</sup> Sb<sup>[16, 215]</sup> and SiGe,<sup>[216]</sup> and layered porous Si@CNT,<sup>[197]</sup> have also been extensively reported. Such structures with adequate void/pore space are more capable of accommodating volume variation, restricting damage/growth of the SEI layer, and enhancing electrochemical reaction kinetics during alloying/dealloying processes while maintaining high tap density and decreasing contact area with electrolytes.<sup>[137, 203, 217]</sup> Figure 12c and f showed typical microsized 2D layered<sup>[46]</sup> and 3D mesoporous<sup>[213]</sup> structural Si anodes, respectively. As illustrated in Figure 12d,g, these structures presented smaller structure changes during lithiation/delithiation processes. As revealed by Li *et al.*,<sup>[213]</sup> large mesoporous Si (>20  $\mu\text{m}$ ) sponge (Figure 12f) can restrict the volume expansion to  $\sim 30\%$  at full lithiation and suppress particle pulverization in bulk Si particles by *in-situ* TEM analysis and continuum media mechanical calculations. The



irreversible capacity loss in the initial cycle of pre-lithiated Si was less than 5%, indicating the thin SEI formation. Notably, albeit the positive improvement effects of these micro-sized multiscale structures, appropriate structural parameters are still necessary. As shown in Figure 12e, the micro-sized 2D Si fabricated at 1000°C (2DSi-1000°C) achieved worse cycling stability than that of 2DSi-900°C,<sup>[46]</sup> owing to the intact 2D layered structure and sufficient layer space.<sup>[46]</sup> Note that the high surface area electrode promotes copious SEI formation, which will decrease the initial Coulombic efficiency. The collapse of the electrode structure during cycling also leads to the over-growth of SEI, deteriorating the charge transfer. Therefore, it is essential to maintain a low surface area when designing the active material and the structural integrity to prevent new surface exposure during cycling.

Besides the hierarchical structural design, electrode surface chemistry also plays a key role in electrolyte reduction. A Al/Na-doped and defect-abundant micro-sized nanostructured Si anode for LIBs achieved positive SEI regulation and improved electrochemical performance.<sup>[200]</sup> The surface Al and Si can be oxidized into Al<sub>2</sub>O<sub>3</sub> and SiO<sub>x</sub>, which serve as the artificial protective layer for  $\mu$ Si anode.<sup>[200]</sup> The *in-situ* formed artificial SEI layer effectively alleviated the mechanical stress/strain of the  $\mu$ Si anode and prevented continuous broken/growth of SEI layer.<sup>[200]</sup>

### 3.4.2 Binders optimization

Binder is a significant electrode component that combines active materials with conductive materials and current collectors. It plays a critical role in ensuring close electrical contact, accommodating volume expansion, maintaining the integrity of alloy anode materials, and stabilizing SEI during cycling processes.<sup>[218]</sup> Han et al. categorized the binders into three types based on the interaction between them and the active anode materials, including inert adhesion, hydrogen binding and covalent crosslinking.<sup>[219]</sup> There is an absence of any chemical reactions between the inert binder and anode; they hold the particles together through van der Waals force. The widely used poly(tetrafluoroethylene) (PTFE) and poly(vinylidene difluoride) (PVDF) belong to this type. Several studies have proved microparticles are more susceptible to pulverization during volume change than their nanoparticle counterparts. Thus, these binders may not be desired for micro-sized alloy anodes due to poor affinity to the particles.<sup>[220]</sup> In comparison, hydrogen bonding improves the connection between the binder and alloy anode. Carboxymethyl cellulose (CMC), poly(acrylic acid) (PAA), and sodium alginate (SA), which have abundant carboxylic acid groups, fall into this category. These binders can naturally induce hydrogen bonding on the surface of alloy anodes, effectively keeping the connection between binder and active materials. The strongest adhesion occurs in the third type, i.e.,

covalent crosslinking, resulting from the interaction between the functional groups of the binder and the surface of alloy anodes. The sturdy binding can effectively maintain the electrode integrity and alleviate the electrical network destruction during cycling, achieving high Coulombic efficiencies and stable cycling performance. Typical candidates include poly(vinyl alcohol) (PVA)- and PAA-derivatives through functionalization and grafting of a second phase.<sup>[2, 221-223]</sup> The latter two types of binders do not only affect the integrity of the electrode but also the SEI components. This is exemplified by Nguyen et al., who adopted citric acid as the binder and surface-modifying agent in the Si anode.<sup>[224]</sup> The reduction of citric acid led to the formation of lithium citrate coated on the Si surface, benefiting the SEI stability. Therefore, based on the roles of the binders, it would be more appropriate to divide them into two types, i.e., structural and functional binders. Both significantly affect the SEI, which is why we discuss the binder in the current review. The functional binder, such as citric acid, has a direct impact on the SEI by either contributing to the SEI species or altering the electrolyte decomposition pathway.<sup>[224]</sup> The role of the structural binder is to keep the electrode integrity by preventing pulverization. Although it does not directly affect the SEI, the pulverization of particles will expose new surfaces and triggers continuous SEI growth. Rapid progress has been made in this direction by improving the mechanical properties of the binder.

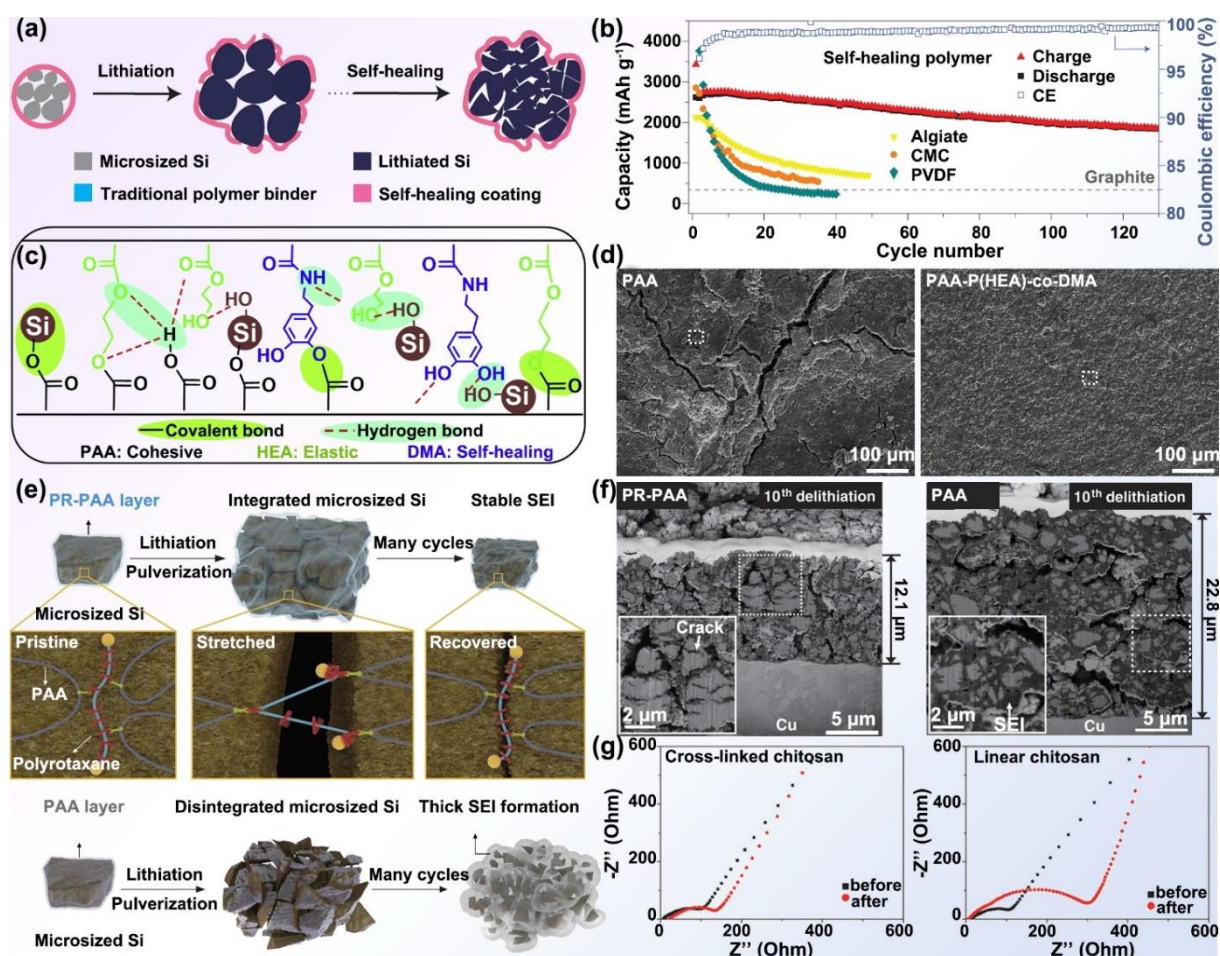




**Figure 13. Binder optimization.** (a) Schematic illustration for the structural change of  $\mu\text{Si}$  anode with self-healing binders. (b) The comparison of cycling performance of  $\mu\text{Si}$  anode with proposed self-sealing binder and traditional PVDF, CMC and alginate polymer binders. Reproduced from Ref.<sup>[34]</sup> with permission. Copyright Nature group. (c) Schematic illustration of structural formulae of PAA-P(HEA-co-DMA) binder and their interaction with Si. (d) SEM images of Si anode after 100 cycles using traditional PAA and designed PAA-P(HEA-co-DMA) binder. Reproduced from Ref.<sup>[223]</sup> with permission. Copyright 2018 Elsevier. (e) Schematic illustration of the stress dissipation mechanism of highly elastic PR-PAA and traditional PAA binder for  $\mu\text{Si}$  anode. (f) cross-sectional SEM of  $\mu\text{Si}$  anode after 10<sup>th</sup> delithiation. Reproduced from Ref.<sup>[2]</sup> with permission. Copyright 2017. (g) EIS curves of  $\mu\text{Sb}$  electrodes with cross-linked chitosan or chitosan before and after the cycling test, respectively. Reproduced from Ref.<sup>[225]</sup> with permission. Copyright 2016 Wiley.

Multifunctional binders with features of self-healing, high elasticity, superior ionic/electronic conductivity, and strong adhesive are popular with alloy anodes. For example, Wang *et al.*<sup>[34]</sup> employed the hydrogen-bond-directed self-healing polymer as the binder to stabilize the  $\mu\text{Si}$  ( $\sim 3\text{-}8\ \mu\text{m}$ ) anode in 2013. Benefiting from the self-healing property, mechanical damage and cracks during charge/discharge processes could be spontaneously recovered after the  $\mu\text{Si}$  anode was encapsulated by such a binder (**Figure 13a**). The 99.2% average Coulombic efficiencies at  $2000\ \text{mA g}^{-1}$  of self-healing polymer modified Si anode suggested minimal side reaction and superior stability of SEI layer (Figure 13b). Besides, in 2018, Xu *et al.*<sup>[223]</sup> designed a self-healing multiple network binder, poly(acrylic acid)-poly(2-hydroxyethyl acrylate-co-dopamine methacrylate) (PAA-P(HEA-co-DMA)), for  $\mu\text{Si}$  anode. As shown in Figure 13c, the covalently cross-linking structure created the network architecture, where abundant hydrogen bonds existed in every local area. Compared with traditional PAA binder, the  $\mu\text{Si}$  anode with self-healing PAA-P(HEA-co-DMA) binder maintained a smooth and intact structure after 100 cycles (Figure 13d). The significant performance enhancement could be attributed to the self-healing binder providing enough mechanical support, effectively accommodating the strain of  $\mu\text{Si}$  particles, and avoiding repeated SEI formation and electrolyte consumption during cycling processes.

In 2017, Choi *et al.*<sup>[2]</sup> designed a highly elastic binder by adding 5 wt% polyrotaxane to conventional PAA binder (PR-PAA) and employed it for  $\mu\text{Si}$  anode in LIBs. The designed elastic PR-PAA binder prevented pulverized Si particles from disintegration (Figure 13e), which stabilized SEI layer and suppressed repeated SEI growth, thereby enhancing the Coulombic efficiency and realizing stable cycling performance at commercial-level areal

capacities. Compared with conventional PAA binder, the  $\mu\text{Si}$  anode with a thickness of  $9.8\ \mu\text{m}$  using the highly elastic PR-PAA binder presented a thickness change of only  $12.1\ \mu\text{m}$  after 10 cycles compared to  $22.8\ \mu\text{m}$  for the one using unmodified PAA binder (Figure 13f), highlighting the positive role of high elastic binder in stabilizing electrode and SEI layer.

The binder-derived stabilizing approach has also been adopted in other microsized alloy anodes. In 2020, Wang *et al.*<sup>[226]</sup> optimized SEI and electrochemical performance of microsized SnSb anode for KIBs by combining the mechanically robust cross-linked CMC and PAA binder and 3 M KFSI-DME electrolyte. Benefiting from the synergistic effect of high-strength binder and electrolyte, the microsized SnSb anode achieved a  $\sim 419\ \text{mAh g}^{-1}$  capacity at  $50\ \text{mA g}^{-1}$  upon 600 cycles, suggesting stable electrode structure and SEI layer during cycling processes.

Besides, Goodenough's group<sup>[225]</sup> developed a polymer network consisting of cross-linked chitosan as a binder for  $\mu\text{Sb}$  anode in NIBs. As shown in Figure 13g, the electrode using cross-linked chitosan binder showed a smaller change of charge-transfer and interface resistance than that of liner chitosan binder. It demonstrated that SEI could be stabilized and electrode structure could be well maintained using the optimized binder. XPS signal further implied that cross-linked chitosan induced the formation of a thin SEI layer. As a result,  $\mu\text{Sb}$  anode for NIBs achieved enhanced Coulombic efficiency and improved cycling stability.

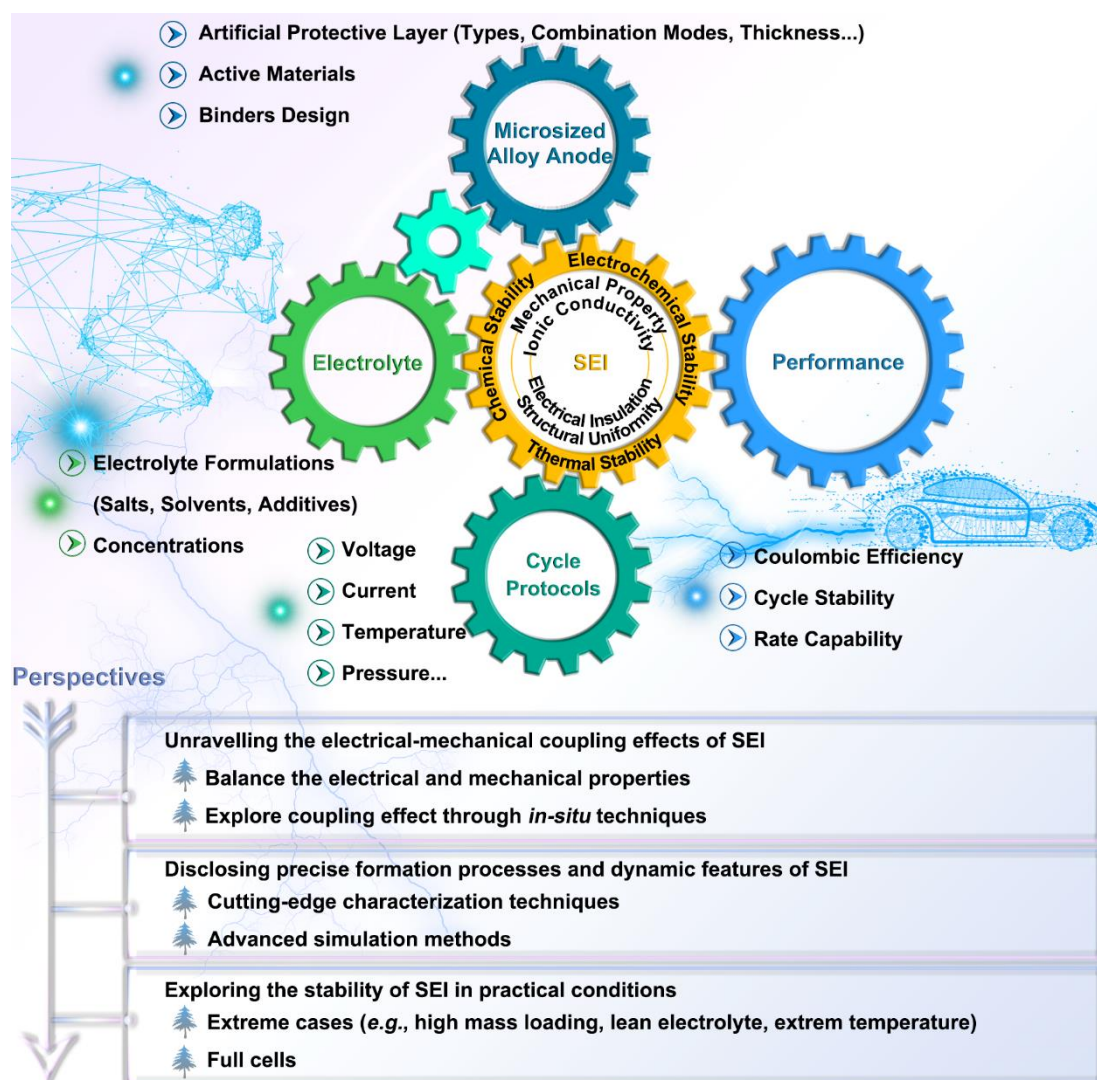


**Figure 14. Perspectives.** Summary of the relationship among electrolyte, micro-sized alloy anode, SEI layer and battery performance, coupled with potential directions of SEI for micro-sized alloy anodes.

#### 4. Summary and perspectives

Micro-sized alloy anodes have been deemed attractive candidates for high-energy-density energy storage systems due to their high tap density, high volumetric energy density and low cost. A high-quality SEI layer is crucial in determining the electrochemical performance and cyclic lifespan of micro-sized alloy anodes with large-volume expansion. In this review, we summarized the regulation and stabilization strategies of SEI for micro-sized alloy anodes in various rechargeable batteries from the perspectives of engineering electrolytes, designing artificial coating, regulation cycle protocols, and optimizing the electrode structures (**Figure 14**). It is worth mentioning that the preferred SEI structure in different electrodes and battery types may differ. Therefore, there is an absence of general SEI design strategies that could be

applied to all the systems. Overall, the SEI should be uniform, dense, thin, mechanically stable and ionic conductive. Although significant progress has been achieved, building such SEIs for general systems and under practical conditions is still a grand challenge. Herein, we propose some perspectives toward future development.

(1) Unravelling the electrical-mechanical coupling effects of the SEI layer. Both the electrical and mechanical properties are closely related to the microstructure of SEI layer. However, the structural requirements for high ionic conductivity and improved mechanical properties may contradict each other. For instance, high content of inorganic components, such as LiF, has been reported to benefit fast charge transfer. Nevertheless, these inorganic components would generally decrease the elasticity of the SEI layer to accommodate the volume change. A compromise may need when designing the SEI layer to balance the electrical and mechanical properties. Furthermore, the mechanical properties determine the SEI's deformation, affecting the diffusion of charges. Such a coupling effect has rarely been explored and could be clarified through *in-situ* techniques in future studies.

(2) Disclosing precise formation processes and dynamic features of the SEI layer through advanced characterization and simulation methods. The recent progress in advanced characterization has offered new opportunities to unveil SEI characteristics. For instance, cryo-TEM allows one to build accurate SEI models in different systems. This will facilitate the understanding of the electrochemical and mechanical properties of SEI through complementary theoretical simulations. The operando techniques make monitoring SEI dynamics on time under commercial cells possible, which is well exemplified in the recent work of sensing the 18650 Li(Na) cells by an optical fiber.<sup>[3]</sup> The enhanced understanding will surely benefit the rational SEI design for stabilizing micro-sized alloy anodes toward practical applications. It is noteworthy that the SEIs formed in different systems, such as Li, Na, and K batteries, could differ a lot even for the same electrode under similar electrolytes, as demonstrated in the metal anodes.<sup>[120]</sup> However, a direct comparison of SEIs in alloy anodes is still lacking. The straightforward extrapolation of successful electrolyte formulations from one system to another does typically not work well. The reason may lie in i) the distinct solvation structure of the cation. The K ions have the weakest desolvation energy among the three alkali-metal ions, which would affect the decomposition pathway of the electrolyte and the resulting SEI; and ii) the solubility discrepancy of the SEI components because of the different Lewis acidity of alkali metal ions. For instance, it is found that the dissolution of SEI has caused a more severe self-discharge issue in NIBs than in LIBs.<sup>[36]</sup> It calls for systematical studies to compare the SEI microstructure and their dynamic features in different batteries, which would benefit the

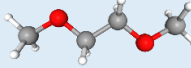
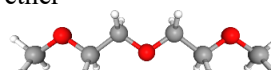
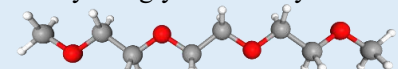
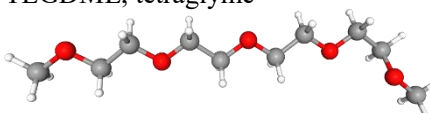
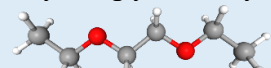
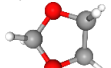
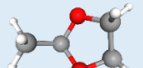
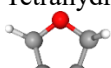
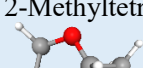
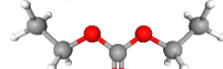
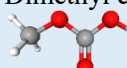
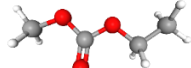
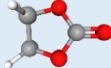
electrolyte and SEI design.

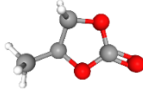
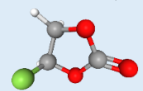
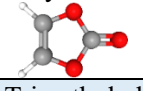
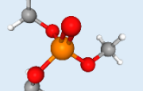
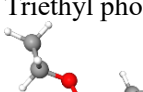
(3) Exploring the stability of the SEI layer in practical conditions. The performance of microsized alloy electrodes operating in extreme cases (e.g., high areal mass loading, lean electrolyte addition, high/low temperature) and full cells should be examined. Currently, most studies are conducted in half-cells with excess electrolytes, which differ from real conditions. For instance, lean electrolytes may limit SEI regeneration on the fracture surface. How it will affect SEI dynamics remains a question. Another critical factor in determining the stability of the SEI layer is the temperature. Generally, the high temperature would trigger the parasite reactions, and the low temperature deteriorates the kinetics, including the charge transfer across the SEI layer. It necessitates deep exploration to unravel the temperature effect and associated mechanisms. Last, the strategies for building stable SEI must be compatible with the cathode, particularly for the electrolytes-derived approaches, which may not match well with the high-voltage cathodes due to the oxidation stability of novel salts/solvents/additives. A holistic evaluation should be adopted in assessing the SEI layer on microsized anodes.

**Table 1.** A summary of fundamental information of metallic Li, Na, K, Zn, Mg, Ca and Al.

Element	Ionic Radius (pm)	Potential versus SHE (V)	Density (g cm <sup>-3</sup> )	Earth Abundance	Theoretical Gravimetric Capacity (mAh g <sup>-1</sup> )	Theoretical Volumetric Capacity (mAh cm <sup>-3</sup> )
Li	76	-3.04	0.53	0.0017 wt%	3860	2061
Na	102	-2.71	0.97	2.3 wt%	1166	1129
K	138	-2.93	0.86	2.09 wt%	687	610
Zn	75	-0.76	7.13	0.0067 wt%	820	5855
Mg	72	-2.36	1.74	2.3 wt%	2206	3831
Ca	100	-2.84	1.55	4.1 wt%	1337	2072
Al	53	-1.68	2.70	8.2 wt%	2980	8046

**Table 2.** The abbreviation (Abbr.), synonyms, linear formula, molecular weight (M), boiling point ( $T_b$ ), viscosity ( $\eta$ ) and dielectric constant ( $\epsilon$ ) of ester and ether solvents. The  $\eta$  and  $\epsilon$  values are obtained from the Ref.<sup>[31, 153, 227]</sup>

Solvent	Abbr.	Full name and 3D conformer	Linear formula	M (g mol <sup>-1</sup> )	$T_b$ (°C)	$\eta$ (mPa s)	$\epsilon$	
Ether	Gn	<i>n</i> Glyme, <i>n</i> (ethylene glycol) dimethyl ether.	CH <sub>3</sub> O(CH <sub>2</sub> CH <sub>2</sub> O) <sub>n</sub> CH <sub>3</sub>	-	-	-	-	
	G1	DME, monoglyme 	CH <sub>3</sub> OCH <sub>2</sub> CH <sub>2</sub> OCH <sub>3</sub>	90.12	85	0.455	7.3	
	G2	Diglyme, diethylene glycol dimethyl ether 	(CH <sub>3</sub> OCH <sub>2</sub> CH <sub>2</sub> ) <sub>2</sub> O	134.17	162	1.06	7.4	
	G3	Triethylene glycol dimethyl ether 	CH <sub>3</sub> O(CH <sub>2</sub> CH <sub>2</sub> O) <sub>3</sub> CH <sub>3</sub>	178.23	216	1.95-2.16	7.53	
	G4	TEGDME, tetraglyme 	CH <sub>3</sub> O(CH <sub>2</sub> CH <sub>2</sub> O) <sub>4</sub> CH <sub>3</sub>	222.28	275	3.3-3.7	7.9	
	EGDE E	Ethylene glycol diethyl ether 	CH <sub>3</sub> CH <sub>2</sub> OCH <sub>2</sub> CH <sub>2</sub> OCH <sub>2</sub> CH <sub>3</sub>	118.17	123.5	0.65	-	
	Cyclic ether	DOL	1,3-Dioxolane 	C <sub>3</sub> H <sub>6</sub> O <sub>2</sub>	74.08	75.6	0.6	7.1
		2-MeDOL	2-Methyl-1,3-dioxolane 	C <sub>4</sub> H <sub>8</sub> O <sub>2</sub>	88.11	82	-	-
		THF	Tetrahydrofuran 	C <sub>4</sub> H <sub>8</sub> O	72.11	66	0.46	7.58
		2-MeTHF	2-Methyltetrahydrofuran 	C <sub>5</sub> H <sub>10</sub> O	86.13	78	0.497	-
Ester	Linear carbonate	DEC	Diethyl carbonate 	(C <sub>2</sub> H <sub>5</sub> O) <sub>2</sub> CO	118.13	126	0.75	2.82
		DMC	Dimethyl carbonates, 	(CH <sub>3</sub> O) <sub>2</sub> CO	90.08	90	0.58	3.1
		EMC	Ethyl methyl carbonate, 	C <sub>4</sub> H <sub>8</sub> O <sub>3</sub>	104.10	101	0.65	2.4
	Cyclic carbonate	EC	Ethylene carbonates 	C <sub>3</sub> H <sub>4</sub> O <sub>3</sub>	88.06	243	1.9	89.6

	PC	Propylene carbonates 	C <sub>4</sub> H <sub>6</sub> O <sub>3</sub>	102.09	240	2.5	66.1	
	FEC	Fluoroethylene carbonate 	C <sub>3</sub> H <sub>3</sub> FO <sub>3</sub>	106.5	212	4.1	96	
	VC	Vinylene carbonate 	C <sub>3</sub> H <sub>2</sub> O <sub>3</sub>	86.05	168	2.2	-	
	Linear phosphate	TMP	Trimethyl phosphate 	(CH <sub>3</sub> ) <sub>3</sub> PO <sub>4</sub>	140.07	197.2	1.98	20.7
		TEP	Triethyl phosphate 	(C <sub>2</sub> H <sub>5</sub> O) <sub>3</sub> PO	182.15	219.	1.54	13

**Table 3.** Summary of SEI features and cycling stability of micro-sized alloy anodes *via* various regulation strategies

Regulation strategies	Electrolyte	Electrode	Cycling performance	SEI		
				Component	Thickness	Properties
Electrolyte Liquid organic	1 M LiDFOB+TMP	Si (~50 μm) <sup>[160]</sup>	950.27 mAh g <sup>-1</sup> (100 cycles, 200 mA g <sup>-1</sup> )	LiF, Li <sub>x</sub> PO <sub>y</sub> F <sub>z</sub> , Li <sub>x</sub> BO <sub>y</sub> F <sub>z</sub>	-	Thin and mechanically stable SEI layer
	1 M LiFSI+IDE/TTE	Si <sup>[127]</sup>	-	Negligible ROLi and abundant LiF species	-	Mechanically stable SEI layer with high Li <sup>+</sup> transport capability
	1.2 M LiFSI+TEP/FEC/BTFE	Si/graphite (1-5 μm) <sup>[128]</sup>	982 mAh g <sup>-1</sup> (300 cycles, 0.75 mA cm <sup>-2</sup> )	LiF	-	LiF-rich SEI layer with improved mechanical stability
	2 M LiPF <sub>6</sub> +mixTHF	Si (>10 μm) <sup>[11]</sup>	2800 mAh g <sup>-1</sup> (200 cycles, 715.8 mA g <sup>-1</sup> )	LiF, Li <sub>2</sub> CO <sub>3</sub> , LiOH, Li <sub>2</sub> O, ROLi/Li <sub>4</sub> SiO <sub>4</sub> , Li <sub>x</sub> PF <sub>y</sub>	2.87 nm	Thin, uniform, and high-modulus LiF-organic bilayer interphase
	2 M LiPF <sub>6</sub> +THF/2-MeTHF	Sn (45 μm) <sup>[156]</sup>	-	LiF, Li <sub>2</sub> CO <sub>3</sub> , ROLi, Li <sub>x</sub> PF <sub>y</sub> , SnF <sub>4</sub>	5.3 nm	Thin, uniform, compact, and mechanically robust SEI layer
	1 M NaPF <sub>6</sub> +EC/PC+5% FEC	Bi <sub>0.25</sub> Sb <sub>1.75</sub> Te <sub>3</sub> (2 μm) <sup>[63]</sup>	406 mA h g <sup>-1</sup> (100 cycles, 200 mA g <sup>-1</sup> )	Na <sub>2</sub> CO <sub>3</sub> , NaOR, NaCO <sub>3</sub> R, NaF, Na <sub>2</sub> O, NaPO <sub>y</sub> F <sub>z</sub>	-	Thin and flexible SEI layer
	1 M NaPF <sub>6</sub> +EC/DEC+5% FEC	Amorphous TiO <sub>2</sub> @P <sub>red</sub> /CNT (~3 μm) <sup>[170]</sup>	972 mAh g <sup>-1</sup> (100 cycles, 100 mA g <sup>-1</sup> )	Na <sub>2</sub> CO <sub>3</sub> , NaF, Na <sub>x</sub> PF <sub>y</sub> O <sub>z</sub>	-	Bilayer with the interior being elastic rich-NaF and exterior being a thin organic shell



1 M NaPF <sub>6</sub> +EC/DEC +5% FEC	P <sub>black</sub> <sup>[54]</sup>	1458 mAh g <sup>-1</sup> (23 cycles, 125 mA g <sup>-1</sup> )	NaF, Na <sub>2</sub> CO <sub>3</sub> , polyenes	-	Thin, homogeneous and durable SEI layer with high ionic conductivity
1 M NaPF <sub>6</sub> +EC/DEC +1% VC		1484 mAh g <sup>-1</sup> (23 cycles, 125 mA g <sup>-1</sup> )	NaF, Na <sub>2</sub> CO <sub>3</sub> , -OCO <sub>2</sub> Na		
1 M NaPF <sub>6</sub> +PC+FEC	Sb <sub>7</sub> P <sub>red63</sub> /C <sub>30</sub> <sup>[50]</sup>	2356.3 mAh g <sup>-1</sup> (70 cycles, C/3)	Na <sub>3</sub> P, Na <sub>x</sub> PF <sub>y</sub> O <sub>z</sub> , NaF	<5 nm	Thin, mechanically robust and high ionic conductive SEI layer
1.2 M NaFSI+DME+B TFE			Na <sub>x</sub> P, NaF		
1 M NaClO <sub>4</sub> +PC+10 % FEC	Sb (0.5~3 μm) <sup>[171]</sup>	605 mAh g <sup>-1</sup> (150 cycles, 200 mA g <sup>-1</sup> )	NaF	~2 nm	Thin and mechanically robust NaF-rich SEI layer with high ionic conductivity
1 M NaClO <sub>4</sub> +PC 5% FEC	Sb (45 μm) <sup>[173]</sup>	576 mAh g <sup>-1</sup> (160 cycles, 330 mA g <sup>-1</sup> )	-	-	Stable SEI layer, verifying by improved efficiency
1 M NaBF <sub>4</sub> +diglyme	Sn (10 μm) <sup>[10]</sup>	-	NaF, Na <sub>2</sub> CO <sub>3</sub> , Na <sub>2</sub> O, Na <sub>x</sub> BO <sub>y</sub> F <sub>z</sub> , and Sn-containing species	~2.5 nm	Ultrathin SEI layer with high elasticity and ionic conductivity
1 M NaPF <sub>4</sub> +diglyme	Sn (45 μm) <sup>[15]</sup>	768 mAh g <sup>-1</sup> (100 cycles, 250 mA g <sup>-1</sup> )	NaF, NaPF <sub>6</sub> , Na <sub>2</sub> O, Na <sub>2</sub> CO <sub>3</sub> , phosphates, RCH <sub>2</sub> ONa	-	Continuous, dense and ionic conductive SEI layer
1 M NaPF <sub>6</sub> +diglyme	Bi (15~18 μm) <sup>[150]</sup>	389 mAh g <sup>-1</sup> (2000 cycles, 400 mA g <sup>-1</sup> )	Na <sub>2</sub> CO <sub>3</sub> , R-COO-Na, RCH <sub>2</sub> ONa, NaF	~3 nm	Mechanically robust and high ionic conductive SEI layer
1 M NaPF <sub>6</sub> +DME	Bi/C <sup>[68]</sup>	310 mAh g <sup>-1</sup> (100 cycles, 200 mA g <sup>-1</sup> )	Inner dense Na <sub>2</sub> CO <sub>3</sub> , NaF and Bi-containing and inorganic layer. Outer ion-conductive polyether layer	~8 nm	High ionic-conducting and robust multi-layered SEI
1 M KPF <sub>6</sub> +diglyme	Bi (74 μm) <sup>[69]</sup>	392 mA h g <sup>-1</sup> (100 cycles, 400 mA g <sup>-1</sup> )	[(CH <sub>2</sub> CH <sub>2</sub> -O-) <sub>n</sub> K, (CH <sub>2</sub> CH <sub>2</sub> -OCH <sub>2</sub> -O-) <sub>n</sub> K], (RCO <sub>2</sub> K), K <sub>2</sub> O <sub>x</sub>	~2.6 nm	Stable SEI layer with excellent mechanical flexibility and elasticity
1 M KFSI+EGDEE	Sb (~5.9 μm) <sup>[33]</sup>	443 mAh g <sup>-1</sup> (150 cycles, 500 mA g <sup>-1</sup> )	[CH <sub>2</sub> CH <sub>2</sub> O] <sub>n</sub> , KF	~20 nm	Thin SEI layer with small Young's modulus and large elastic strain
4 M KFSI+DME	Sb (18 μm) <sup>[125]</sup>	553 mAh g <sup>-1</sup> (200 cycles, 200 mA g <sup>-1</sup> )	High proportion of F-based inorganic species (e.g., KF).	-	Chemically/electrochemically stable SEI layer
4 M KFSI+DME	Submicron-sized BiSb (2 μm) <sup>[136]</sup>	514.1 mAh g <sup>-1</sup> (100 cycles, 250 mA g <sup>-1</sup> )	KF, K <sub>2</sub> S <sub>2</sub> O <sub>3</sub> , K <sub>2</sub> SO <sub>3</sub> , K <sub>2</sub> SO <sub>4</sub> , KHSO <sub>4</sub>	-	Robust, compact and ultrathin SEI layer with fast K <sup>+</sup> transport capability

		5 M KFSI+diglyme	(BiO) <sub>2</sub> CO <sub>3</sub> (~1 μm) <sup>[165]</sup>	450 mAh g <sup>-1</sup> (100 cycles, 25 mA g <sup>-1</sup> )	Organic-rich outer layer and inorganic-rich inner layer	-	Thin and mechanically robust SEI layer
		5 M KFSI+TMP+HF E (molar ratio of 1: 1.7 : 2)	P <sub>black</sub> /graphite <sup>l</sup> <sub>52]</sub>	342 mAh g <sup>-1</sup> (300 cycles, 300 mA g <sup>-1</sup> )	Rich (S=O)-N species but less amounts of inorganic components such as KF, K <sub>2</sub> S, and K <sub>2</sub> SO <sub>3</sub>	12.2 nm	Stable SEI layer with low Young's modulus and high elastic strain limit
	Ionic liquid	2 M LiFSI+Pyr <sub>14</sub> FSI	Si (~4.5 μm) <sup>[100]</sup>	1497 mAh g <sup>-1</sup> , (200 cycles, 2 A g <sup>-1</sup> )	LiF, Li <sub>x</sub> N, Li <sub>x</sub> SO <sub>y</sub> , Li <sub>2</sub> CO <sub>3</sub> , ROCO <sub>2</sub> Li	-	Robust SEI layer with thermally stable, high-modulus, and inorganic-rich features
	Solid state	PEO@LATP	Si@SiO <sub>2</sub> @LP O@C (~1 μm) <sup>[129]</sup>	1440.6 mAh g <sup>-1</sup> (200 cycles, 200 mA g <sup>-1</sup> )	Li <sub>2</sub> CO <sub>3</sub> , LiF, RO-C=O	~15 nm	Stable SEI layer with high mechanical stability and high ionic conductivity
		Li <sub>6</sub> PS <sub>5</sub> Cl	Si (~2 μm) <sup>[130]</sup>	80% capacity retention (500 cycles, 5 mA cm <sup>-2</sup> )	Li <sub>2</sub> S, Li <sub>3</sub> P, LiCl	-	Mechanically robust and stable 2D SEI layer
Artificial protective layers	Carbon layer	1 M LiPF <sub>6</sub> +EC/DEC+ 5% FEC	NPSi@C (~50 μm) <sup>[44]</sup>	1093.1 mAh g <sup>-1</sup> (2000 cycles, 5 A g <sup>-1</sup> )	-	-	Mechanically robust SEI layer with fast Li <sup>+</sup> transport capability
	N-doped carbon nanosheet frameworks	1 M LiPF <sub>6</sub> +EC/DEC+ 5% FEC	NPSi@NCNF <sub>s</sub> <sup>[47]</sup>	822.2 mAh g <sup>-1</sup> (4000 cycles, 5 A g <sup>-1</sup> )	-	-	Mechanically robust SEI layer with fast Li <sup>+</sup> transport capability
	Nanoscale carbon layer	1 M LiPF <sub>6</sub> +EC/DEC/ DMC+10% FEC	Si@C (20 μm) <sup>[187]</sup>	1459 mAh g <sup>-1</sup> (200 cycles, 1 A g <sup>-1</sup> )	-	-	Uniform and crack-free SEI layer
	Soft multiwall carbon nanotube	1 M LiPF <sub>6</sub> +EC/DEC/ FEC (volume ratio of 1: 1: 0.2)	Si-CNT <sup>[195]</sup>	~ 610 mAh g <sup>-1</sup> (1200 cycles, 500 mA g <sup>-1</sup> )	-	-	Stable SEI layer with high ionic conductivity
	Graphene	1 M LiPF <sub>6</sub> +EC/DEC/ VC	P-Si/rGO (~8 μm) <sup>[71]</sup>	1258 mAh g <sup>-1</sup> (300 cycles, 210 mA g <sup>-1</sup> )	-	-	Mechanically stable SEI layer
	Graphene cages	1 M LiPF <sub>6</sub> +EC/DEC+ 10% FEC+1% VC	μSi@graphene (~1-3 μm) <sup>[18]</sup>	~1400 mAh g <sup>-1</sup> (300 cycles, 1000 mA g <sup>-1</sup> )	-	-	Thin and mechanically stable SEI layer
	Graphene	1 M LiPF <sub>6</sub> +EC/DEC+ 5% FEC	μSi@overlapped graphene@rGO (1-5 μm) <sup>[199]</sup>	1697 mAh g <sup>-1</sup> (200 mA g <sup>-1</sup> )	-	-	Deformable and stable SEI layer
	Nano TiO <sub>2</sub>	1 M LiPF <sub>6</sub>	P <sub>black</sub> @TiO <sub>2</sub> (5 μm) <sup>[207]</sup>	1049 mAh g <sup>-1</sup> (100 cycles, 519 mA g <sup>-1</sup> )	Thin SEI layer and a Li <sub>x</sub> Ti <sub>y</sub> O <sub>z</sub> passivation layer	-	Mechanically stable SEI layer with high charge transfer capability
	Single-walled carbon nanotube	1 M NaClO <sub>4</sub> +DMC/F EC (volume ratio of 1: 1)	P <sub>red</sub> -SWCNT (~5 μm) <sup>[188]</sup>	80% capacity retention (2000 cycles, 2000 mA g <sup>-1</sup> )	-	-	Mechanically robust SEI layer with high Na <sup>+</sup> transport capability

	Microporous carbon layer	1 M NaClO <sub>4</sub> +EC/DEC/FEC (volume ratio of 1: 1: 0.2)	P@YP (50 μm) <sup>[193]</sup>	1064 mAh g <sup>-1</sup> (100 cycles, 520 mA g <sup>-1</sup> )	-	-	Mechanically stable SEI layer
	Ti <sub>3</sub> C <sub>2</sub> T <sub>x</sub> MXene	1 M NaClO <sub>4</sub> +EC/PC	Phosphorene/MXene <sup>[137]</sup>	343 mAh g <sup>-1</sup> (1000 cycles, 1000 mA g <sup>-1</sup> )	NaF, phosphorus species	<15 nm	NaF-rich SEI layer with good Na <sup>+</sup> conductivity and robust mechanical property
	Conductive polymer hydrogel	1 M LiPF <sub>6</sub> +EC/DEC/VC (volume ratio of 1: 1: 0.02)	3D microsized Si-PANI <sup>[133]</sup>	1600 mAh g <sup>-1</sup> (1000 cycles, 1000 mA g <sup>-1</sup> )	-	-	Thin, mechanically deformable and stable SEI layer with fast Li <sup>+</sup> transport capability
	PPy	1 M LiPF <sub>6</sub> +EC/DEC/VC	μSi (~1 μm) <sup>[208]</sup>	1660 mAh g <sup>-1</sup> (500 cycles, 0.2 C)	-	-	Thin SEI layer
	PHATN	1 M LiPF <sub>6</sub> +EC/DEC/FEC	PCSi (~4 μm) <sup>[134]</sup>	1129.6 mAh g <sup>-1</sup> (500 cycles, 1000 mA g <sup>-1</sup> )	Rich LiF, Li <sub>2</sub> Si <sub>2</sub> O <sub>5</sub> , Li <sub>2</sub> SiO <sub>3</sub> , Li <sub>x</sub> PO <sub>y</sub> F <sub>z</sub>	26.6 nm	Thin, uniform and mechanically robust SEI layer
	cPAN	1.2 M LiFSI+PYR <sub>13</sub> FSI	PCSi (1-5 μm) <sup>[210]</sup>	2240 mAh g <sup>-1</sup> (250 cycles, 0.286 mA cm <sup>-2</sup> )	LiF, SO <sub>2</sub>	-	Thin and mechanically robust SEI layer accommodating volume change of μSi
Cycle protocols	Electrochemical pre-treatment	1 M LiPF <sub>6</sub> +EC/EMC +5% FEC	Si <sup>[84]</sup>	~1700 mAh g <sup>-1</sup> (150 cycles, 715 mA g <sup>-1</sup> )	Li <sub>2</sub> CO <sub>3</sub> , LiF (cell gap of 0.5 mm)	5-8 nm	Thick SEI layer with some cracks
				~2400 mAh g <sup>-1</sup> (150 cycles, 715 mA g <sup>-1</sup> )	LiF-rich nanoparticles (cell gap of 2 mm)	2-3 nm	Thin, chemically stable, and mechanically rigid SEI layer with uniform distributed Li <sup>+</sup> flux
	Current Parameters	1 M LiPF <sub>6</sub> +EC/DEC+10% FEC	P <sub>red</sub> @CNF <sup>[77]</sup>	~1850 mAh g <sup>-1</sup> (500 cycles, 100 mA g <sup>-1</sup> )	LiF	-	LiF-rich SEI layer with good electrochemical and mechanical stability
	Voltage regulation	1 M NaPF <sub>6</sub> +DME	Sn (~10 μm) <sup>[138]</sup>	455 mAh g <sup>-1</sup> (2500 cycles, 2000 mA g <sup>-1</sup> , 0.01-0.62 V)	-	-	Thin, NaF-rich, and elastic SEI layer
	Presodiation	1 M NaPF <sub>6</sub> +EC/DEC +5% FEC	Sb <sup>[212]</sup>	500 mAh g <sup>-1</sup> (300 cycles, 2000 mA g <sup>-1</sup> )	NaF, Na <sub>2</sub> CO <sub>3</sub> , ROCO <sub>2</sub> Na	~20 nm	Chemically stable, mechanically robust and uniform SEI layer
Structure design	2D layered	1 M LiPF <sub>6</sub> +EC/DEC+5% FEC	Si (~50 μm) <sup>[46]</sup>	835 mAh g <sup>-1</sup> (3000 cycles, 5000 mA g <sup>-1</sup> )	-	-	Mechanically robust and thin SEI layer
	Layered porous	1 M LiPF <sub>6</sub> +EC/DEC/DMC+6% FEC	Si (~1-20 μm) <sup>[197]</sup>	1682 mAh g <sup>-1</sup> (100 cycles, 200 mA g <sup>-1</sup> )	Li <sub>2</sub> CO <sub>3</sub> , LiF, RO <sub>2</sub> Li, ROCO <sub>2</sub> Li	23.1 nm	Thin and mechanically stable SEI layer
	Porous	1 M NaClO <sub>4</sub> +PC+5% FEC	Sb (~5 μm) <sup>[215]</sup>	414 mAh g <sup>-1</sup> (120 cycles, 50 mA g <sup>-1</sup> )	-	-	Mechanically stable SEI layer with high Na <sup>+</sup> transport capability

	Nanoporous	1 M LiPF <sub>6</sub> +EC/DEC	Si (~2 μm) <sup>[45]</sup>	835 mAh g <sup>-1</sup> (3000 cycles, 5 A g <sup>-1</sup> )	-	-	Thin and compact SEI layer
	Nanoporous	1 M KPF <sub>6</sub> +EC/DEC	Sb (~2 μm) <sup>[16]</sup>	318 mAh g <sup>-1</sup> (50 cycles, 100 mA g <sup>-1</sup> )	-	-	Thin and mechanically stable SEI layer
	Mesoporous	1 M LiPF <sub>6</sub> +EC/DEC+ 10% FEC	Si (>20 μm) <sup>[213]</sup>	740 mAh g <sup>-1</sup> (800 cycles, 1 A g <sup>-1</sup> )	-	-	Compact and crack- free SEI layer
Binders	Self-Healing polymers	1 M LiPF <sub>6</sub> +EC/DEC/ FEC (volume ratio of 1: 1: 0.4)	Si (~3-8 μm) <sup>[34]</sup>	2094 mAh g <sup>-1</sup> (90 cycles, 400 mA g <sup>-1</sup> )	-	-	Chemically/electroch emically/mechanicall y stable SEI layer
	PAA- P(HEA- coDMA)	1 M LiPF <sub>6</sub> +EC/DMC +10% FEC	Si (~0.5-3 μm) <sup>[223]</sup>	2394 mAh g <sup>-1</sup> (220 cycles, 1 A g <sup>-1</sup> )	-	-	Mechanically stable SEI layer
	PR-PAA	1 M LiPF <sub>6</sub> +EC/DEC/ FEC/VC	Si (2.1 μm) <sup>[2]</sup>	2971 mAh g <sup>-1</sup> (20 cycles, 100 mA g <sup>-1</sup> )	ROCO <sub>2</sub> Li, Li <sub>2</sub> CO <sub>3</sub> , Li <sub>2</sub> O, LiF	-	Thin and mechanically stable SEI layer
	Cross- Linked Chitosan	1 M NaPF <sub>6</sub> +PC/FEC	Sb <sup>[225]</sup>	555.4 mAh g <sup>-1</sup> (100 cycles, 660 mA g <sup>-1</sup> )	C-O-C, -O- COO-, Na <sub>2</sub> CO <sub>3</sub> or alkyl carbonate -O- COONa	-	Uniform and robust SEI layer that can accommodate volume changes of μSb
	CMC+PAA	3 M KFSI+DME	SnSb/C (1-6 μm) <sup>[226]</sup>	~419 mAh g <sup>-1</sup> (600 cycles, 50 mA g <sup>-1</sup> )	RCH <sub>2</sub> OK, K <sub>2</sub> CO <sub>3</sub> , KF	-	Continuous, homogeneous and stable SEI layer

## Acknowledgments

This work was supported by the General Research Fund scheme of the Hong Kong Research Grants Council (project no. 15305219), and the Hong Kong Polytechnic University (CDBJ).

Received: ((will be filled in by the editorial staff))

Revised: ((will be filled in by the editorial staff))

Published online: ((will be filled in by the editorial staff))

## References

- [1] M. Armand, J. M. Tarascon, *Nature* 2008, 451, 652; J. M. Tarascon, M. Armand, *Nature* 2001, 414, 359; J. W. Choi, D. Aurbach, *Nat. Rev. Mater.* 2016, 1, 16013; S. Luo, F. Wu, G. Yushin, *Mater. Today* 2021, 49, 253; J. Xie, L. Ma, J. Li, X. Yin, Z. Wen, Y. Zhong, C. Li, Y. Liu, Z. Shen, W. Mai, G. Hong, W. Zhang, *Adv. Mater.* 2022, 34, 2205625.
- [2] S. Choi, T. W. Kwon, A. Coskun, J. W. Choi, *Science* 2017, 357, 279.
- [3] J. Huang, L. Albero Blanquer, J. Bonafino, E. R. Logan, D. Alves Dalla Corte, C. Delacourt, B. M. Gallant, S. T. Boles, J. R. Dahn, H.-Y. Tam, J.-M. Tarascon, *Nat. Energy* 2020, 5, 674.

- [4] Y. Gao, R. Yi, Y. C. Li, J. Song, S. Chen, Q. Huang, T. E. Mallouk, D. Wang, *J. Am. Chem. Soc.* 2017, 139, 17359.
- [5] H. Wu, G. Chan, J. W. Choi, I. Ryu, Y. Yao, M. T. McDowell, S. W. Lee, A. Jackson, Y. Yang, L. Hu, Y. Cui, *Nat. Nanotechnol.* 2012, 7, 310; W. Zhang, W. K. Pang, V. Sencadas, Z. Guo, *Joule* 2018, 2, 1534.
- [6] N. Liu, Z. Lu, J. Zhao, M. T. McDowell, H. W. Lee, W. Zhao, Y. Cui, *Nat. Nanotechnol.* 2014, 9, 187.
- [7] S. Imtiaz, I. S. Amiinu, Y. Xu, T. Kennedy, C. Blackman, K. M. Ryan, *Mater. Today* 2021, 48, 241.
- [8] X. Zheng, H. Fu, C. Hu, H. Xu, Y. Huang, J. Wen, H. Sun, W. Luo, Y. Huang, *J. Phys. Chem. Lett.* 2019, 10, 707.
- [9] Y. Gao, X. Du, Z. Hou, X. Shen, Y.-W. Mai, J.-M. Tarascon, B. Zhang, *Joule* 2021, 5, 1860.
- [10] J. Huang, X. Guo, X. Du, X. Lin, J.-Q. Huang, H. Tan, Y. Zhu, B. Zhang, *Energy Environ. Sci.* 2019, 12, 1550.
- [11] J. Chen, X. Fan, Q. Li, H. Yang, M. R. Khoshi, Y. Xu, S. Hwang, L. Chen, X. Ji, C. Yang, H. He, C. Wang, E. Garfunkel, D. Su, O. Borodin, C. Wang, *Nat. Energy* 2020, 5, 386.
- [12] J. Niu, Z. Zhang, D. Aurbach, *Adv. Energy Mater.* 2020, 10, 2000697.
- [13] H. Wu, G. Yu, L. Pan, N. Liu, M. T. McDowell, Z. Bao, Y. Cui, *Nat. Commun.* 2013, 4, 1943.
- [14] J. Wang, Y. Cui, *Nat. Energy* 2020, 5, 361.
- [15] B. Zhang, G. Rousse, D. Foix, R. Dugas, D. A. Corte, J. M. Tarascon, *Adv. Mater.* 2016, 28, 9824.
- [16] Y. An, Y. Tian, L. Ci, S. Xiong, J. Feng, Y. Qian, *ACS Nano* 2018, 12, 12932.
- [17] G. Zhu, D. Chao, W. Xu, M. Wu, H. Zhang, *ACS Nano* 2021, 15, 15567.
- [18] Y. Li, K. Yan, H.-W. Lee, Z. Lu, N. Liu, Y. Cui, *Nat. Energy* 2016, 1, 15029.
- [19] Z. Zhang, Y. Li, R. Xu, W. Zhou, Y. Li, S. T. Oyakhire, Y. Wu, J. Xu, H. Wang, Z. Yu, D. T. Boyle, W. Huang, Y. Ye, H. Chen, J. Wan, Z. Bao, W. Chiu, Y. Cui, *Science* 2022, 375, 66; Y. Sun, C. Zhao, K. R. Adair, Y. Zhao, L. V. Goncharova, J. Liang, C. Wang, J. Li, R. Li, M. Cai, T.-K. Sham, X. Sun, *Energy Environ. Sci.* 2021, 14, 4085; J. Li, N. Zhuang, J. Xie, X. Li, W. Zhuo, H. Wang, J. B. Na, X. Li, Y. Yamauchi, W. Mai, *Adv. Energy Mater.* 2020, 10, 1903455.
- [20] X. Li, J. Li, W. Zhuo, Z. Li, L. Ma, Z. Ji, L. Pan, W. Mai, *Nano-Micro Lett.* 2021, 13, 179.

- [21] B. Lee, E. Paek, D. Mitlin, S. W. Lee, *Chem. Rev.* 2019, 119, 5416.
- [22] Y. Tian, Y. An, C. Wei, H. Jiang, S. Xiong, J. Feng, Y. Qian, *Nano Energy* 2020, 78, 105344.
- [23] Q. Zhao, S. Stalin, L. A. Archer, *Joule* 2021, 5, 1119.
- [24] H. Wang, D. Zhai, F. Kang, *Energy Environ. Sci.* 2020, 13, 4583.
- [25] A. K. Stephan, *Joule* 2019, 3, 1812.
- [26] E. Peled, S. Menkin, *J. Electrochem. Soc.* 2017, 164, A1703.
- [27] G. G. Eshetu, G. A. Elia, M. Armand, M. Forsyth, S. Komaba, T. Rojo, S. Passerini, *Adv. Energy Mater.* 2020, 10, 2000093.
- [28] W. Liu, P. Liu, D. Mitlin, *Adv. Energy Mater.* 2020, 10, 2002297.
- [29] T. Li, X.-Q. Zhang, P. Shi, Q. Zhang, *Joule* 2019, 3, 2647.
- [30] Y. Jin, P. M. L. Le, P. Y. Gao, Y. B. Xu, B. W. Xiao, M. H. Engelhard, X. Cao, T. D. Vo, J. T. Hu, L. R. Zhong, B. E. Matthews, R. Yi, C. M. Wang, X. L. Li, J. Liu, J. G. Zhang, *Nat. Energy* 2022, 7, 718.
- [31] M. Zhou, P. Bai, X. Ji, J. Yang, C. Wang, Y. Xu, *Adv. Mater.* 2021, 33, 2003741.
- [32] X.-Q. Zhang, X.-B. Cheng, X. Chen, C. Yan, Q. Zhang, *Adv. Funct. Mater.* 2017, 27, 1605989.
- [33] X. Du, Y. Gao, B. Zhang, *Adv. Funct. Mater.* 2021, 31, 2102562.
- [34] C. Wang, H. Wu, Z. Chen, M. T. McDowell, Y. Cui, Z. Bao, *Nat. Chem.* 2013, 5, 1042.
- [35] L. A. Ma, A. J. Naylor, L. Nyholm, R. Younesi, *Angew. Chem. Int. Ed.* 2021, 60, 4855.
- [36] R. Mogensen, D. Brandell, R. Younesi, *ACS Energy Lett.* 2016, 1, 1173.
- [37] B. Zhang, F. Kang, J.-M. Tarascon, J.-K. Kim, *Prog. Mater. Sci.* 2016, 76, 319.
- [38] Y. An, H. Fei, G. Zeng, L. Ci, B. Xi, S. Xiong, J. Feng, *J. Power Sources* 2018, 378, 66.
- [39] J. Xie, J. Li, X. Li, H. Lei, W. Zhuo, X. Li, G. Hong, K. N. Hui, L. Pan, W. Mai, *CCS Chemistry* 2021, 3, 791; X. Yuan, S. Chen, J. Li, J. Xie, G. Yan, B. Liu, X. Li, R. Li, L. Pan, W. Mai, *Carbon Energy* 2021, 3, 615.
- [40] M. Lao, Y. Zhang, W. Luo, Q. Yan, W. Sun, S. X. Dou, *Adv. Mater.* 2017, 29, 1700622; Y. Tian, Y. An, C. Liu, S. Xiong, J. Feng, Y. Qian, *Energy Storage Mater.* 2021, 41, 343; M. N. Obrovac, V. L. Chevrier, *Chem. Rev.* 2014, 114, 11444.
- [41] Y. An, Y. Tian, C. Wei, Y. Tao, B. Xi, S. Xiong, J. Feng, Y. Qian, *Nano Today* 2021, 37, 101094.
- [42] D. Liu, Z. J. Liu, X. Li, W. Xie, Q. Wang, Q. Liu, Y. Fu, D. He, *Small* 2017, 13, 1702000.
- [43] H. Yoo, J. I. Lee, H. Kim, J. P. Lee, J. Cho, S. Park, *Nano Lett.* 2011, 11, 4324; Q. Xu, J. Y. Li, Y. X. Yin, Y. M. Kong, Y. G. Guo, L. J. Wan, *Chem. Asian. J.* 2016, 11, 1205; Y. An,

- Y. Tian, C. Wei, Y. Zhang, S. Xiong, J. Feng, Y. Qian, *Energy Storage Mater.* 2020, 32, 115;
- Q. Ma, Z. Zhao, Y. Zhao, H. Xie, P. Xing, D. Wang, H. Yin, *Energy Storage Mater.* 2021, 34, 768.
- [44] Y. An, Y. Tian, H. Wei, B. Xi, S. Xiong, J. Feng, Y. Qian, *Adv. Funct. Mater.* 2019, 30, 1908721.
- [45] Y. An, H. Fei, G. Zeng, L. Ci, S. Xiong, J. Feng, Y. Qian, *ACS Nano* 2018, 12, 4993.
- [46] Y. An, Y. Tian, C. Wei, H. Jiang, B. Xi, S. Xiong, J. Feng, Y. Qian, *ACS Nano* 2019, 13, 13690.
- [47] Y. An, Y. Tian, C. Liu, S. Xiong, J. Feng, Y. Qian, *ACS Nano* 2022, 16, 4560.
- [48] S. Liu, J. Feng, X. Bian, J. Liu, H. Xu, Y. An, *Energy Environ. Sci.* 2017, 10, 1222; W. Li, S. Hu, X. Luo, Z. Li, X. Sun, M. Li, F. Liu, Y. Yu, *Adv. Mater.* 2017, 29, 1605820; J. Ni, L. Li, J. Lu, *ACS Energy Lett.* 2018, 3, 1137; G. Qin, Y. Liu, F. Liu, X. Sun, L. Hou, B. Liu, C. Yuan, *Adv. Energy Mater.* 2020, 11, 2003429; B. Zhang, R. Dugas, G. Rousse, P. Rozier, A. M. Abakumov, J. M. Tarascon, *Nat. Commun.* 2016, 7, 10308.
- [49] S. Liu, H. Xu, X. Bian, J. Feng, J. Liu, Y. Yang, C. Yuan, Y. An, R. Fan, L. Ci, *ACS Nano* 2018, 12, 7380.
- [50] X. Liu, B. Xiao, A. Daali, X. Zhou, Z. Yu, X. Li, Y. Liu, L. Yin, Z. Yang, C. Zhao, L. Zhu, Y. Ren, L. Cheng, S. Ahmed, Z. Chen, X. Li, G.-L. Xu, K. Amine, *ACS Energy Lett.* 2021, 6, 547.
- [51] Y. Wu, H. B. Huang, Y. Feng, Z. S. Wu, Y. Yu, *Adv. Mater.* 2019, 31, 1901414.
- [52] X. Du, B. Zhang, *ACS Nano* 2021, 15, 16851.
- [53] H. Liu, K. Hu, D. Yan, R. Chen, Y. Zou, H. Liu, S. Wang, *Adv. Mater.* 2018, 30, 1800295; R. Meng, J. Huang, Y. Feng, L. Zu, C. Peng, L. Zheng, L. Zheng, Z. Chen, G. Liu, B. Chen, Y. Mi, J. Yang, *Adv. Energy Mater.* 2018, 8, 1801514.
- [54] M. Dahbi, N. Yabuuchi, M. Fukunishi, K. Kubota, K. Chihara, K. Tokiwa, X.-f. Yu, H. Ushiyama, K. Yamashita, J.-Y. Son, Y.-T. Cui, H. Oji, S. Komaba, *Chem. Mater.* 2016, 28, 1625.
- [55] Y. Xu, Y. Zhu, Y. Liu, C. Wang, *Adv. Energy Mater.* 2013, 3, 128.
- [56] B. Zhang, J. Huang, J.-K. Kim, *Adv. Funct. Mater.* 2015, 25, 5222.
- [57] Y. Liu, N. Zhang, L. Jiao, J. Chen, *Adv. Mater.* 2015, 27, 6702.
- [58] J. Xie, Y. Ji, L. Ma, Z. Wen, J. Pu, L. Wang, S. Ding, Z. Shen, Y. Liu, J. Li, W. Mai, G. Hong, *ACS Nano* 2023, 17, 1511–1521.
- [59] Y. Liu, Y. Xu, Y. Zhu, J. N. Culver, C. A. Lundgren, K. Xu, C. Wang, *ACS Nano* 2013, 7, 3627.



- [60] Y. Tian, Y. An, S. Xiong, J. Feng, Y. Qian, *J. Mater. Chem. A* 2019, 7, 9716; Z. Yi, Z. Wang, Y. Cheng, L. Wang, *Energy Environ. Mater.* 2018, 1, 132.
- [61] Z. Liu, X.-Y. Yu, X. W. Lou, U. Paik, *Energy Environ. Sci.* 2016, 9, 2314; S. Liu, J. Feng, X. Bian, J. Liu, H. Xu, *Energy Environ. Sci.* 2016, 9, 1229; Y. An, Y. Tian, J. Feng, Y. Qian, *Mater. Today* 2022, 57, 146.
- [62] Q. Zhang, J. Mao, W. K. Pang, T. Zheng, V. Sencadas, Y. Chen, Y. Liu, Z. Guo, *Adv. Energy Mater.* 2018, 8, 1703288.
- [63] Marcin W. Orzech, F. Mazzali, J. D. McGettrick, C. Pleydell-Pearce, T. M. Watson, W. Voice, D. Jarvis, S. Margadonna, *J. Mater. Chem. A* 2017, 5, 23198.
- [64] C. K. Chan, H. Peng, G. Liu, K. McIlwrath, X. F. Zhang, R. A. Huggins, Y. Cui, *Nat. Nanotechnol.* 2008, 3, 31.
- [65] G. Zhou, L. Xu, G. Hu, L. Mai, Y. Cui, *Chem. Rev.* 2019, 119, 11042.
- [66] R. Zhao, H. Di, C. Wang, X. Hui, D. Zhao, R. Wang, L. Zhang, L. Yin, *ACS Nano* 2020, 14, 13938.
- [67] R. Zhao, H. Di, X. Hui, D. Zhao, R. Wang, C. Wang, L. Yin, *Energy Environ. Sci.* 2020, 13, 246.
- [68] H. Yuan, F. Ma, X. Wei, J. L. Lan, Y. Liu, Y. Yu, X. Yang, H. S. Park, *Adv. Energy Mater.* 2020, 10, 2001418.
- [69] J. Huang, X. Lin, H. Tan, B. Zhang, *Adv. Energy Mater.* 2018, 8, 1703496.
- [70] N. Nitta, F. Wu, J. T. Lee, G. Yushin, *Mater. Today* 2015, 18, 252.
- [71] W. Zhai, Q. Ai, L. Chen, S. Wei, D. Li, L. Zhang, P. Si, J. Feng, L. Ci, *Nano Res.* 2017, 10, 4274.
- [72] Y. Tian, Y. An, H. Wei, C. Wei, Y. Tao, Y. Li, B. Xi, S. Xiong, J. Feng, Y. Qian, *Chem. Mater.* 2020, 32, 4054.
- [73] R. Jain, A. S. Lakhnot, K. Bhimani, S. Sharma, V. Mahajani, R. A. Panchal, M. Kamble, F. Han, C. Wang, N. Koratkar, *Nat. Rev. Mater.* 2022, 7, 736.
- [74] J. Han, H. Li, D. Kong, C. Zhang, Y. Tao, H. Li, Q.-H. Yang, L. Chen, *ACS Energy Lett.* 2020, 5, 1986.
- [75] Y. F. Tian, G. Li, D. X. Xu, Z. Y. Lu, M. Y. Yan, J. Wan, J. Y. Li, Q. Xu, S. Xin, R. Wen, Y. G. Guo, *Adv. Mater.* 2022, 34, 2200672.
- [76] H. Zhu, Z. Jia, Y. Chen, N. Weadock, J. Wan, O. Vaaland, X. Han, T. Li, L. Hu, *Nano Lett.* 2013, 13, 3093.
- [77] Y. Liu, Q. Liu, C. Jian, D. Cui, M. Chen, Z. Li, T. Li, T. Nilges, K. He, Z. Jia, C. Zhou, *Nat. Commun.* 2020, 11, 2520.

- [78] E. Peled, *J. Electrochem. Soc.* 1979, 126, 2047.
- [79] Y. Ein-Eli, B. Markovsky, D. Aurbach, Y. Carmeli, H. Yamin, S. Luski, *Electrochim. Acta* 1994, 39, 2559.
- [80] E. Peled, D. Golodnitsky, G. Ardel, *J. Electrochem. Soc.* 1997, 144, L208.
- [81] S. Shi, P. Lu, Z. Liu, Y. Qi, L. G. Hector, Jr., H. Li, S. J. Harris, *J. Am. Chem. Soc.* 2012, 134, 15476.
- [82] P. Peljo, H. H. Girault, *Energy Environ. Sci.* 2018, 11, 2306.
- [83] C. Stetson, Y. Yin, C.-S. Jiang, S. C. DeCaluwe, M. Al-Jassim, N. R. Neale, C. Ban, A. Burrell, *ACS Energy Lett.* 2019, 4, 2770.
- [84] O. B. Chae, L. Rynearson, B. L. Lucht, *ACS Energy Lett.* 2022, 7, 3087.
- [85] J. Nanda, G. Yang, T. Hou, D. N. Voylov, X. Li, R. E. Ruther, M. Naguib, K. Persson, G. M. Veith, A. P. Sokolov, *Joule* 2019, 3, 2001.
- [86] A. Gajan, C. Lecourt, B. E. Torres Bautista, L. Fillaud, J. Demeaux, I. T. Lucas, *ACS Energy Lett.* 2021, 6, 1757.
- [87] X. Yu, A. Manthiram, *Energy Environ. Sci.* 2018, 11, 527.
- [88] A. N. Dey, B. P. Sullivan, *J. Electrochem. Soc.* 1970, 117, 222.
- [89] E. Peled, *J. Power Sources* 1983, 9, 253.
- [90] G. Nazri, R. H. Muller, *J. Electrochem. Soc.* 1985, 132, 1385; G. Nazri, R. H. Muller, *J. Electrochem. Soc.* 1985, 132, 2050.
- [91] D. Aurbach, M. L. Daroux, P. W. Faguy, E. Yeager, *J. Electrochem. Soc.* 1987, 134, 1611.
- [92] K. Kanamura, H. Tamura, S. Shiraishi, Z. i. Takehara, *J. Electrochem. Soc.* 1995, 142, 340.
- [93] X. Cao, X. Ren, L. Zou, M. H. Engelhard, W. Huang, H. Wang, B. E. Matthews, H. Lee, C. Niu, B. W. Arey, Y. Cui, C. Wang, J. Xiao, J. Liu, W. Xu, J.-G. Zhang, *Nat. Energy* 2019, 4, 796; Y. Li, Y. Li, A. Pei, K. Yan, Y. Sun, C. L. Wu, L. M. Joubert, R. Chin, A. L. Koh, Y. Yu, J. Perrino, B. Butz, S. Chu, Y. Cui, *Science* 2017, 358, 506.
- [94] J. B. Goodenough, Y. Kim, *Chem. Mater.* 2009, 22, 587.
- [95] Y. Ma, Y. Ma, H. Euchner, X. Liu, H. Zhang, B. Qin, D. Geiger, J. Biskupek, A. Carlsson, U. Kaiser, A. Groß, S. Indris, S. Passerini, D. Bresser, *ACS Energy Lett.* 2021, 6, 915; D. Li, L. Cao, T. Deng, S. Liu, C. Wang, *Angew. Chem. Int. Ed.* 2021, 60, 13035.
- [96] M. Ma, H. Cai, C. Xu, R. Huang, S. Wang, H. Pan, Y. S. Hu, *Adv. Funct. Mater.* 2021, 31, 2100278.

- [97] K. Liu, A. Pei, H. R. Lee, B. Kong, N. Liu, D. Lin, Y. Liu, C. Liu, P. C. Hsu, Z. Bao, Y. Cui, *J. Am. Chem. Soc.* 2017, 139, 4815; N. Takenaka, A. Bouibes, Y. Yamada, M. Nagaoka, A. Yamada, *Adv. Mater.* 2021, 33, 2100574.
- [98] X. B. Cheng, R. Zhang, C. Z. Zhao, F. Wei, J. G. Zhang, Q. Zhang, *Adv. Sci.* 2016, 3, 1500213.
- [99] H. He, D. Sun, Y. Tang, H. Wang, M. Shao, *Energy Storage Mater.* 2019, 23, 233.
- [100] Q. Liu, T. Meng, L. Yu, S. Guo, Y. Hu, Z. Liu, X. Hu, *Small Methods* 2022, 6, 2200380.
- [101] H. Dong, J. Wang, P. Wang, H. Ding, R. Song, N.-S. Zhang, D.-N. Zhao, L.-J. Zhang, S.-Y. Li, *J. Energy Chem.* 2022, 64, 190.
- [102] M. Moshkovich, Y. Gofer, D. Aurbach, *J. Electrochem. Soc.* 2001, 148, E155.
- [103] F. Shi, Z. Song, P. N. Ross, G. A. Somorjai, R. O. Ritchie, K. Komvopoulos, *Nat. Commun.* 2016, 7, 11886.
- [104] A. v Cresce, S. M. Russell, D. R. Baker, K. J. Gaskell, K. Xu, *Nano Lett.* 2014, 14, 1405.
- [105] J. Wu, M. Ihsan-Ul-Haq, Y. Chen, J.-K. Kim, *Nano Energy* 2021, 89, 106489.
- [106] Y. Zhou, M. Su, X. Yu, Y. Zhang, J. G. Wang, X. Ren, R. Cao, W. Xu, D. R. Baer, Y. Du, O. Borodin, Y. Wang, X. L. Wang, K. Xu, Z. Xu, C. Wang, Z. Zhu, *Nat. Nanotechnol.* 2020, 15, 224.
- [107] C. Yan, R. Xu, Y. Xiao, J. F. Ding, L. Xu, B. Q. Li, J. Q. Huang, *Adv. Funct. Mater.* 2020, 30, 1909887.
- [108] A. M. Tripathi, W. N. Su, B. J. Hwang, *Chem. Soc. Rev.* 2018, 47, 736.
- [109] T. Liu, L. Lin, X. Bi, L. Tian, K. Yang, J. Liu, M. Li, Z. Chen, J. Lu, K. Amine, K. Xu, F. Pan, *Nat. Nanotechnol.* 2019, 14, 50.
- [110] H. Lee, A. Kim, H. S. Kim, C. W. Jeon, T. Yoon, *Adv. Energy Mater.* 2022, 13, 2202780.
- [111] X. Y. Zhang, T. M. Devine, *J. Electrochem. Soc.* 2006, 153, B344.
- [112] Y. Gao, B. Zhang, *Adv. Mater.* 2023, 10.1002/adma.202205421, 2205421.
- [113] D. Liu, Z. Shadike, R. Lin, K. Qian, H. Li, K. Li, S. Wang, Q. Yu, M. Liu, S. Ganapathy, X. Qin, Q. H. Yang, M. Wagemaker, F. Kang, X. Q. Yang, B. Li, *Adv. Mater.* 2019, 31, 1806620.
- [114] Y. Li, W. Huang, Y. Li, A. Pei, D. T. Boyle, Y. Cui, *Joule* 2018, 2, 2167.
- [115] W. Huang, J. Wang, M. R. Braun, Z. Zhang, Y. Li, D. T. Boyle, P. C. McIntyre, Y. Cui, *Matter* 2019, 1, 1232.
- [116] D. Polcari, P. Dauphin-Ducharme, J. Mauzeroll, *Chem. Rev.* 2016, 116, 13234; D. Liu, Q. Yu, S. Liu, K. Qian, S. Wang, W. Sun, X.-Q. Yang, F. Kang, B. Li, *J. Phys. Chem. C* 2019, 123, 12797.

- [117] H. Bulter, F. Peters, J. Schwenzel, G. Wittstock, *Angew. Chem. Int. Ed.* 2014, 53, 10531.
- [118] D. Martin-Yerga, D. C. Milan, X. Xu, J. Fernandez-Vidal, L. Whalley, A. J. Cowan, L. J. Hardwick, P. R. Unwin, *Angew. Chem. Int. Ed.* 2022, 61, 202207184.
- [119] J. Zhang, R. Wang, X. Yang, W. Lu, X. Wu, X. Wang, H. Li, L. Chen, *Nano Lett.* 2012, 12, 2153; I. Yoon, S. Jurng, D. P. Abraham, B. L. Lucht, P. R. Guduru, *Nano Lett.* 2018, 18, 5752; N. Weadock, N. Varongchayakul, J. Wan, S. Lee, J. Seog, L. Hu, *Nano Energy* 2013, 2, 713; D. Aurbach, B. Markovsky, M. D. Levi, E. Levi, A. Schechter, M. Moshkovich, Y. Cohen, *J. Power Sources* 1999, 81-82, 95.
- [120] Y. Gu, W. W. Wang, Y. J. Li, Q. H. Wu, S. Tang, J. W. Yan, M. S. Zheng, D. Y. Wu, C. H. Fan, W. Q. Hu, Z. B. Chen, Y. Fang, Q. H. Zhang, Q. F. Dong, B. W. Mao, *Nat. Commun.* 2018, 9, 1339.
- [121] J. Liu, S. Y. Lee, J. Yoo, S. Kim, J.-H. Kim, H. Cho, *ACS Materials Lett.* 2022, 4, 840; S. Huang, L.-Z. Cheong, S. Wang, D. Wang, C. Shen, *Appl. Surf. Sci.* 2018, 452, 67.
- [122] P. Desai, J. Huang, H. Hijazi, L. Zhang, S. Mariyappan, J. M. Tarascon, *Adv. Energy Mater.* 2021, 11, 2101490.
- [123] J. Huang, X. Han, F. Liu, C. Gervillié, L. A. Blanquer, T. Guo, J.-M. Tarascon, *Energy Environ. Sci.* 2021, 14, 6464.
- [124] L. Zhou, Z. Cao, W. Wahyudi, J. Zhang, J.-Y. Hwang, Y. Cheng, L. Wang, L. Cavallo, T. Anthopoulos, Y.-K. Sun, H. N. Alshareef, J. Ming, *ACS Energy Lett.* 2020, 5, 766; Y. Sun, F. Ai, Y. C. Lu, *Small* 2022, 18, 2200009; Y. Sun, Q. Zou, W. Wang, Y.-C. Lu, *ACS Energy Lett.* 2021, 6, 3607; Z. Hou, Y. Gao, H. Tan, B. Zhang, *Nat. Commun.* 2021, 12, 3083; X. Li, J. Li, L. Ma, C. Yu, Z. Ji, L. Pan, W. Mai, *Energy Environ. Mater.* 2021, 5, 458.
- [125] L. Zhou, Z. Cao, J. Zhang, H. Cheng, G. Liu, G. T. Park, L. Cavallo, L. Wang, H. N. Alshareef, Y. K. Sun, J. Ming, *Adv. Mater.* 2021, 33, 2005993.
- [126] J. L. Gómez-Cámer, B. Acebedo, N. Ortiz-Vitoriano, I. Monterrubio, M. Galcerán, T. Rojo, *J. Mater. Chem. A* 2019, 7, 18434.
- [127] N. M. Johnson, Z. Yang, M. Kim, D.-J. Yoo, Q. Liu, Z. Zhang, *ACS Energy Lett.* 2022, 7, 897.
- [128] H. Jia, L. Zou, P. Gao, X. Cao, W. Zhao, Y. He, M. H. Engelhard, S. D. Burton, H. Wang, X. Ren, Q. Li, R. Yi, X. Zhang, C. Wang, Z. Xu, X. Li, J. G. Zhang, W. Xu, *Adv. Energy Mater.* 2019, 9, 1900784.
- [129] L. Gu, J. Han, M. Chen, W. Zhou, X. Wang, M. Xu, H. Lin, H. Liu, H. Chen, J. Chen, Q. Zhang, X. Han, *Energy Storage Mater.* 2022, 52, 547.

- [130] D. H. S. Tan, Y. T. Chen, H. Yang, W. Bao, B. Sreenarayanan, J. M. Doux, W. Li, B. Lu, S. Y. Ham, B. Sayahpour, J. Scharf, E. A. Wu, G. Deysher, H. E. Han, H. J. Hah, H. Jeong, J. B. Lee, Z. Chen, Y. S. Meng, *Science* 2021, 373, 1494.
- [131] Y. Li, M. Liu, X. Feng, Y. Li, F. Wu, Y. Bai, C. Wu, *ACS Energy Lett.* 2021, 6, 3307.
- [132] W. Song, E. S. Scholtis, P. C. Sherrell, D. K. H. Tsang, J. Ngiam, J. Lischner, S. Fearn, V. Bemmer, C. Mattevi, N. Klein, F. Xie, D. J. Riley, *Energy Environ. Sci.* 2020, 13, 4977.
- [133] F. Shi, P. N. Ross, H. Zhao, G. Liu, G. A. Somorjai, K. Komvopoulos, *J. Am. Chem. Soc.* 2015, 137, 3181; S. Ko, T. Obukata, T. Shimada, N. Takenaka, M. Nakayama, A. Yamada, Y. Yamada, *Nat. Energy* 2022, 7, 1217.
- [134] Q. Wang, M. Zhu, G. Chen, N. Dudko, Y. Li, H. Liu, L. Shi, G. Wu, D. Zhang, *Adv. Mater.* 2022, 34, 2109658.
- [135] W. An, B. Gao, S. Mei, B. Xiang, J. Fu, L. Wang, Q. Zhang, P. K. Chu, K. Huo, *Nat. Commun.* 2019, 10, 1447.
- [136] K.-T. Chen, Y.-C. Yang, L.-M. Lyu, M.-Y. Lu, H.-Y. Tuan, *Nano Energy* 2021, 88, 106233.
- [137] X. Guo, W. Zhang, J. Zhang, D. Zhou, X. Tang, X. Xu, B. Li, H. Liu, G. Wang, *ACS Nano* 2020, 14, 3651.
- [138] Y. Zhu, Z. Qian, J. Song, W. Du, J. Pan, D. Wang, J. Yang, *Nano Lett.* 2021, 21, 3588.
- [139] N. Yao, X. Chen, Z. H. Fu, Q. Zhang, *Chem. Rev.* 2022, 122, 10970.
- [140] M. Li, R. P. Hicks, Z. Chen, C. Luo, J. Guo, C. Wang, Y. Xu, *Chem. Rev.* 2023, 10.1021/acs.chemrev.2c00374, 1712.
- [141] X. Fan, C. Wang, *Chem. Soc. Rev.* 2021, 50, 10486.
- [142] B. S. Parimalam, B. L. Lucht, *J. Electrochem. Soc.* 2018, 165, A251.
- [143] L. Ma, J. Li, T. Wu, P. Sun, S. Tan, H. Wang, W. Xie, L. Pan, Y. Yamauchi, W. Mai, *Nano Energy* 2021, 87, 106150.
- [144] H. Zheng, H. Xiang, F. Jiang, Y. Liu, Y. Sun, X. Liang, Y. Feng, Y. Yu, *Adv. Energy Mater.* 2020, 10, 2001440.
- [145] B. Qin, A. Schiele, Z. Jusys, A. Mariani, T. Diemant, X. Liu, T. Brezesinski, R. J. Behm, A. Varzi, S. Passerini, *ACS Appl. Mater. Interfaces* 2020, 12, 3697.
- [146] H. Wang, J. He, J. Liu, S. Qi, M. Wu, J. Wen, Y. Chen, Y. Feng, J. Ma, *Adv. Funct. Mater.* 2020, 31, 2002578.
- [147] Z. Piao, R. Gao, Y. Liu, G. Zhou, H. M. Cheng, *Adv. Mater.* 2022, 2206009; J. Chen, Q. Li, T. P. Pollard, X. Fan, O. Borodin, C. Wang, *Mater. Today* 2020, 39, 118.

- [148] J. Xie, X. Li, H. Lai, Z. Zhao, J. Li, W. Zhang, W. Xie, Y. Liu, W. Mai, *Angew. Chem. Int. Ed.* 2019, 58, 14740.
- [149] X. Su, Y. Xu, Y. Wu, H. Li, J. Yang, Y. Liao, R. Qu, Z. Zhang, *Energy Storage Mater.* 2023, 56, 642; S. Zhang, K. Xu, T. Jow, *J. Solid State Electrochem.* 2003, 7, 147.
- [150] C. Wang, L. Wang, F. Li, F. Cheng, J. Chen, *Adv. Mater.* 2017, 29, 1702212.
- [151] X. Du, Y. Gao, Z. Hou, X. Guo, Y. Zhu, B. Zhang, *ACS Appl. Energy Mater.* 2022, 5, 2252.
- [152] J. Zhang, D. W. Wang, W. Lv, L. Qin, S. Niu, S. Zhang, T. Cao, F. Kang, Q. H. Yang, *Adv. Energy Mater.* 2018, 8, 1801361.
- [153] Y. Li, F. Wu, Y. Li, M. Liu, X. Feng, Y. Bai, C. Wu, *Chem. Soc. Rev.* 2022, 51, 4484.
- [154] H. Yang, R. Xu, Y. Yao, S. Ye, X. Zhou, Y. Yu, *Adv. Funct. Mater.* 2019, 29, 1809195.
- [155] D. Wang, X. Du, B. Zhang, *Small Struct.* 2022, 3, 2200078.
- [156] N. Zhang, C. Sun, Y. Huang, C. Zhu, Z. Wu, L. Lv, X. Zhou, X. Wang, X. Xiao, X. Fan, L. Chen, *J. Mater. Chem. A* 2021, 9, 1812.
- [157] K. Xu, *Chem. Rev.* 2014, 114, 11503.
- [158] G. Zeng, Y. An, S. Xiong, J. Feng, *ACS Appl. Mater. Interfaces* 2019, 11, 23229.
- [159] J. Wang, Y. Yamada, K. Sodeyama, E. Watanabe, K. Takada, Y. Tateyama, A. Yamada, *Nat. Energy* 2017, 3, 22.
- [160] K. Zhang, Y. Tian, C. Wei, Y. An, J. Feng, *Appl. Surf. Sci.* 2021, 553, 149566.
- [161] S. Zhang, S. Li, Y. Lu, *eScience* 2021, 1, 163.
- [162] Q. Zheng, Y. Yamada, R. Shang, S. Ko, Y.-Y. Lee, K. Kim, E. Nakamura, A. Yamada, *Nat. Energy* 2020, 5, 291.
- [163] Z. Zeng, X. Jiang, R. Li, D. Yuan, X. Ai, H. Yang, Y. Cao, *Adv. Sci.* 2016, 3, 1600066; Z. Yang, J. He, W. H. Lai, J. Peng, X. H. Liu, X. X. He, X. F. Guo, L. Li, Y. Qiao, J. M. Ma, M. Wu, S. L. Chou, *Angew. Chem. Int. Ed.* 2021, 60, 27086.
- [164] J. R. D. W. R. McKinnon, *J. Electrochem. Soc.* 1985, 132, 364.
- [165] L. Wang, B. Zhang, B. Wang, S. Zeng, M. Zhao, X. Sun, Y. Zhai, L. Xu, *Angew. Chem. Int. Ed.* 2021, 60, 15381.
- [166] L. Ji, M. Gu, Y. Shao, X. Li, M. H. Engelhard, B. W. Arey, W. Wang, Z. Nie, J. Xiao, C. Wang, J. G. Zhang, J. Liu, *Adv. Mater.* 2014, 26, 2901.
- [167] A. M. Haregewoin, A. S. Wotango, B.-J. Hwang, *Energy Environ. Sci.* 2016, 9, 1955.
- [168] Y. Jin, N. H. Kneusels, L. E. Marbella, E. Castillo-Martinez, P. Magusin, R. S. Weatherup, E. Jonsson, T. Liu, S. Paul, C. P. Grey, *J. Am. Chem. Soc.* 2018, 140, 9854; Y. Li, Y. An, Y. Tian, H. Fei, S. Xiong, Y. Qian, J. Feng, *J. Electrochem. Soc.* 2019, 166, A2736.



- [169] M. Peng, K. Shin, L. Jiang, Y. Jin, K. Zeng, X. Zhou, Y. Tang, *Angew. Chem. Int. Ed.* 2022, 61, 202206770.
- [170] J. Zhang, K. Zhang, J. Yang, V. Wing-wei Lau, G.-H. Lee, M. Park, Y.-M. Kang, *Chem. Mater.* 2019, 32, 448.
- [171] X. Bian, Y. Dong, D. Zhao, X. Ma, M. Qiu, J. Xu, L. Jiao, F. Cheng, N. Zhang, *ACS Appl. Mater. Interfaces* 2020, 12, 3554.
- [172] M. Xu, Y. Li, M. Ihsan-Ul-Haq, N. Mubarak, Z. Liu, J. Wu, Z. Luo, J. K. Kim, *Energy Storage Mater.* 2022, 44, 477.
- [173] A. Darwiche, C. Marino, M. T. Sougrati, B. Fraisse, L. Stievano, L. Monconduit, *J. Am. Chem. Soc.* 2012, 134, 20805.
- [174] J. Qian, X. Wu, Y. Cao, X. Ai, H. Yang, *Angew. Chem. Int. Ed.* 2013, 52, 4633.
- [175] S. Yuan, K. Ding, X. Zeng, D. Bin, Y. Zhang, P. Dong, Y. Wang, *Adv. Mater.* 2022, 10.1002/adma.202206228, 2206228.
- [176] L. B. Huang, G. Li, Z. Y. Lu, J. Y. Li, L. Zhao, Y. Zhang, X. D. Zhang, K. C. Jiang, Q. Xu, Y. G. Guo, *ACS Appl. Mater. Interfaces* 2021, 13, 24916.
- [177] L. Hu, X. Zhu, Y. Du, Y. Li, X. Zhou, J. Bao, *Chem. Mater.* 2015, 27, 8138.
- [178] K. Eom, J. Jung, J. T. Lee, V. Lair, T. Joshi, S. W. Lee, Z. Lin, T. F. Fuller, *Nano Energy* 2015, 12, 314.
- [179] Q. Sun, Z. Cao, Z. Ma, J. Zhang, W. Wahyudi, G. Liu, H. Cheng, T. Cai, E. Xie, L. Cavallo, Q. Li, J. Ming, *Adv. Funct. Mater.* 2022, 33, 2210292.
- [180] G. Yan, K. Reeves, D. Foix, Z. Li, C. Cometto, S. Mariyappan, M. Salanne, J. M. Tarascon, *Adv. Energy Mater.* 2019, 9, 1901431.
- [181] D. T. Rogstad, M.-A. Einarsrud, A. M. Svensson, *J. Electrochem. Soc.* 2021, 168, 110506.
- [182] M. Armand, F. Endres, D. R. MacFarlane, H. Ohno, B. Scrosati, *Nat. Mater.* 2009, 8, 621.
- [183] A. Banerjee, X. Wang, C. Fang, E. A. Wu, Y. S. Meng, *Chem. Rev.* 2020, 120, 6878; P. Hundekar, S. Basu, X. Fan, L. Li, A. Yoshimura, T. Gupta, V. Sarbada, A. Lakhnot, R. Jain, S. Narayanan, Y. Shi, C. Wang, N. Koratkar, *Proc. Natl. Acad. Sci.* 2020, 117, 5588; C. Wang, J. Liang, J. Luo, J. Liu, X. Li, F. Zhao, R. Li, H. Huang, S. Zhao, L. Zhang, J. Wang, X. Sun, *Sci. Adv.* 2021, 7, eabh1896; W. Xia, Y. Zhao, F. Zhao, K. Adair, R. Zhao, S. Li, R. Zou, Y. Zhao, X. Sun, *Chem. Rev.* 2022, 122, 3763; C. Wang, T. Deng, X. Fan, M. Zheng, R. Yu, Q. Lu, H. Duan, H. Huang, C. Wang, X. Sun, *Joule* 2022, 6, 1770.

- [184] H. Wang, J. Hu, J. Dong, K. C. Lau, L. Qin, Y. Lei, B. Li, D. Zhai, Y. Wu, F. Kang, *Adv. Energy Mater.* 2019, 9, 1902697; Z. Lu, W. Li, Y. Long, J. Liang, Q. Liang, S. Wu, Y. Tao, Z. Weng, W. Lv, Q. H. Yang, *Adv. Funct. Mater.* 2019, 30, 1907343.
- [185] P. Nie, X. Liu, R. Fu, Y. Wu, J. Jiang, H. Dou, X. Zhang, *ACS Energy Lett.* 2017, 2, 1279.
- [186] R. Nandan, N. Takamori, K. Higashimine, R. Badam, N. Matsumi, *J. Mater. Chem. A* 2022, 10, 15960.
- [187] R. Yi, F. Dai, M. L. Gordin, S. Chen, D. Wang, *Adv. Energy Mater.* 2013, 3, 295.
- [188] Y. Zhu, Y. Wen, X. Fan, T. Gao, F. Han, C. Luo, S. C. Liou, C. Wang, *ACS Nano* 2015, 9, 3254.
- [189] W. J. Li, S. L. Chou, J. Z. Wang, H. K. Liu, S. X. Dou, *Nano Lett.* 2013, 13, 5480.
- [190] H. Tian, X. Tan, F. Xin, C. Wang, W. Han, *Nano Energy* 2015, 11, 490.
- [191] G. Hou, B. Cheng, Y. Yang, Y. Du, Y. Zhang, B. Li, J. He, Y. Zhou, D. Yi, N. Zhao, Y. Bando, D. Golberg, J. Yao, X. Wang, F. Yuan, *ACS Nano* 2019, 13, 10179.
- [192] Y. An, Y. Tian, Y. Zhang, C. Wei, L. Tan, C. Zhang, N. Cui, S. Xiong, J. Feng, Y. Qian, *ACS Nano* 2020, 14, 17574.
- [193] Z. Yu, J. Song, D. Wang, D. Wang, *Nano Energy* 2017, 40, 550.
- [194] H. Wu, G. Zheng, N. Liu, T. J. Carney, Y. Yang, Y. Cui, *Nano Lett.* 2012, 12, 904; C. Yu, X. Tian, Z. Xiong, Z. Zhang, Z. Sun, X. Piao, *J. Alloys Compd.* 2021, 869, 159124; T. Zhao, D. Zhu, W. Li, A. Li, J. Zhang, *J. Power Sources* 2019, 439, 227027; B.-H. Chen, S.-I. Chuang, J.-G. Duh, *J. Power Sources* 2016, 331, 198; J. Liu, P. Kopold, C. Wu, P. A. van Aken, J. Maier, Y. Yu, *Energy Environ. Sci.* 2015, 8, 3531.
- [195] D. Wei, X. Gao, S. Zeng, H. Li, H. Li, W. Li, X. Tao, L. Xu, P. Chen, *ChemElectroChem* 2018, 5, 3143.
- [196] Y. Wu, S. Hu, R. Xu, J. Wang, Z. Peng, Q. Zhang, Y. Yu, *Nano Lett.* 2019, 19, 1351.
- [197] Y. Ren, X. Yin, R. Xiao, T. Mu, H. Huo, P. Zuo, Y. Ma, X. Cheng, Y. Gao, G. Yin, Y. Li, C. Du, *Chem. Engineer. J.* 2022, 431, 133982.
- [198] H. Gao, T. Zhou, Y. Zheng, Y. Liu, J. Chen, H. Liu, Z. Guo, *Adv. Energy Mater.* 2016, 6, 1601037; F. Lyu, Z. Sun, B. Nan, S. Yu, L. Cao, M. Yang, M. Li, W. Wang, S. Wu, S. Zeng, H. Liu, Z. Lu, *ACS Appl. Mater. Interfaces* 2017, 9, 10699; F. Chen, J. Han, D. Kong, Y. Yuan, J. Xiao, S. Wu, D.-M. Tang, Y. Deng, W. Lv, J. Lu, F. Kang, Q.-H. Yang, *Natl. Sci. Rev.* 2021, 8, nwab012.
- [199] X. Zhang, R. Guo, X. Li, L. Zhi, *Small* 2018, 14, 1800752.
- [200] J. Wang, X. Meng, X. Fan, W. Zhang, H. Zhang, C. Wang, *ACS Nano* 2015, 9, 6576.

- [201] J. Song, Z. Yu, M. L. Gordin, X. Li, H. Peng, D. Wang, *ACS Nano* 2015, 9, 11933.
- [202] L. Zhao, B. Ding, X. Y. Qin, Z. Wang, W. Lv, Y. B. He, Q. H. Yang, F. Kang, *Adv. Mater.* 2022, 34, 2106704; J. Xie, Y. Zhu, N. Zhuang, H. Lei, W. Zhu, Y. Fu, M. S. Javed, J. Li, W. Mai, *Nanoscale* 2018, 10, 17092.
- [203] J. Sun, H. W. Lee, M. Pasta, H. Yuan, G. Zheng, Y. Sun, Y. Li, Y. Cui, *Nat. Nanotechnol.* 2015, 10, 980.
- [204] S. Sim, P. Oh, S. Park, J. Cho, *Adv. Mater.* 2013, 25, 4498.
- [205] O. Ruiz, M. Cochrane, M. Li, Y. Yan, K. Ma, J. Fu, Z. Wang, S. H. Tolbert, V. B. Shenoy, E. Detsi, *Adv. Energy Mater.* 2018, 8, 1801781.
- [206] Y. Han, P. Qi, J. Zhou, X. Feng, S. Li, X. Fu, J. Zhao, D. Yu, B. Wang, *ACS Appl. Mater. Interfaces* 2015, 7, 26608.
- [207] Y. Luo, H. Wu, L. Liu, Q. Li, K. Jiang, S. Fan, J. Li, J. Wang, *ACS Appl. Mater. Interfaces* 2018, 10, 36058.
- [208] Y. Lv, M. Shang, X. Chen, P. S. Nezhad, J. Niu, *ACS Nano* 2019, 13, 12032.
- [209] S. Gao, F. Sun, N. Liu, H. Yang, P.-F. Cao, *Mater. Today* 2020, 40, 140; S. Pan, J. Han, Y. Wang, Z. Li, F. Chen, Y. Guo, Z. Han, K. Xiao, Z. Yu, M. Yu, S. Wu, D. W. Wang, Q. H. Yang, *Adv. Mater.* 2022, 34, 2203617.
- [210] A. Heist, D. M. Piper, T. Evans, S. C. Kim, S. S. Han, K. H. Oh, S.-H. Lee, *J. Electrochem. Soc.* 2018, 165, A244.
- [211] N. Liu, H. Wu, M. T. McDowell, Y. Yao, C. Wang, Y. Cui, *Nano Lett.* 2012, 12, 3315.
- [212] M. Liu, Z. Yang, Y. Shen, S. Guo, J. Zhang, X. Ai, H. Yang, J. Qian, *J. Mater. Chem. A* 2021, 9, 5639.
- [213] X. Li, M. Gu, S. Hu, R. Kennard, P. Yan, X. Chen, C. Wang, M. J. Sailor, J. G. Zhang, J. Liu, *Nat. Commun.* 2014, 5, 4105.
- [214] B. M. Bang, J.-I. Lee, H. Kim, J. Cho, S. Park, *Adv. Energy Mater.* 2012, 2, 878.
- [215] H. Zhang, W. An, H. Song, B. Xiang, S. Mei, Y. Hu, B. Gao, *Solid State Ion.* 2020, 352, 115365.
- [216] Y. Yang, S. Liu, X. Bian, J. Feng, Y. An, C. Yuan, *ACS Nano* 2018, 12, 2900.
- [217] Y. Zhang, H. Wang, Z. Luo, H. T. Tan, B. Li, S. Sun, Z. Li, Y. Zong, Z. J. Xu, Y. Yang, K. A. Khor, Q. Yan, *Adv. Energy Mater.* 2016, 6, 1600453; Y. Tian, Y. An, C. Wei, B. Xi, S. Xiong, J. Feng, Y. Qian, *ACS Nano* 2019, 13, 11676.
- [218] Y. M. Zhao, F. S. Yue, S. C. Li, Y. Zhang, Z. R. Tian, Q. Xu, S. Xin, Y. G. Guo, *InfoMat* 2021, 3, 460; Y. Tian, Y. An, J. Feng, Y. Qian, *Mater. Today* 2022, 52, 225; I. Kovalenko, B.

Zdyrko, A. Magasinski, B. Hertzberg, Z. Milicev, R. Burtovyy, I. Luzinov, G. Yushin, *Science* 2011, 334, 75.

[219] L. Han, T. Liu, O. Sheng, Y. Liu, Y. Wang, J. Nai, L. Zhang, X. Tao, *ACS Appl. Mater. Interfaces* 2021, 13, 45139.

[220] D. H. Yoon, M. Marinaro, P. Axmann, M. Wohlfahrt-Mehrens, *J. Electrochem. Soc.* 2020, 167, 160537.

[221] J. Song, M. Zhou, R. Yi, T. Xu, M. L. Gordin, D. Tang, Z. Yu, M. Regula, D. Wang, *Adv. Funct. Mater.* 2014, 24, 5904.

[222] Z.-J. Han, N. Yabuuchi, K. Shimomura, M. Murase, H. Yui, S. Komaba, *Energy Environ. Sci.* 2012, 5, 9014.

[223] Z. Xu, J. Yang, T. Zhang, Y. Nuli, J. Wang, S.-i. Hirano, *Joule* 2018, 2, 950.

[224] C. C. Nguyen, D. M. Seo, K. Chandrasiri, B. L. Lucht, *Langmuir* 2017, 33, 9254.

[225] H. Gao, W. Zhou, J.-H. Jang, J. B. Goodenough, *Adv. Energy Mater.* 2016, 6, 1502130.

[226] J. Wu, Q. Zhang, S. Liu, J. Long, Z. Wu, W. Zhang, W. K. Pang, V. Sencadas, R. Song, W. Song, J. Mao, Z. Guo, *Nano Energy* 2020, 77, 105118.

[227] J. Chen, A. Naveed, Y. Nuli, J. Yang, J. Wang, *Energy Storage Mater.* 2020, 31, 382.